UNIVERSITY OF CALIFORNIA

Los Angeles

Design and Synthesis of Plasmonic Core/Shell Nanorods for Light Trapping in Organic Photo-Voltaics, Non-Linear Optics and Photo-Thermal Therapy

A dissertation submitted in partial satisfaction of the
requirements for the degree Doctor of Philosophy
in Chemical Engineering

by

Vladan Janković

2014

ABSTRACT OF THE DISSERTATION

Design and Synthesis of Plasmonic Core/Shell Nanorods for

Light Trapping in Organic Photo-Voltaics, Non-Linear Optics

and Photo-Thermal Therapy

by

Vladan Janković

Doctor of Philosophy in Chemical Engineering

University of California, Los Angeles 2014

Professor Jane P. Chang, Chair

Core/shell nanorods based on a plasmonic gold nanorod core with a thin dielectric shell were designed, synthesized and characterized to demonstrate their potential in photovoltaics and cancer therapy applications.

For solar cell applications, the light scattering properties of Au nanorods were combined with an electrically insulating silica (SiO_2) shell layer in order to isolate the conductive metal surface of the gold from the photo-polymers in the active layers of organic photovoltaic (OPV) devices. Specifically, octadecyltrimethoxysilane (OTMS)-functionalized Au/SiO_2 core/shell nanorods were spectrally tailored and incorporated into the active layer of two OPV polymer systems: poly(3-hexylthiophene):[6,6]-phenyl-C61-butyric acid methyl ester (P3HT:$PCB_{60}M$) and poly[2,6-4,8-di(5-ethylhexylthienyl)benzo[1,2-b;3,4-b]dithiophene-alt-5-dibutyloctyl-3,6-bis(5-

bromothiophen-2-yl) pyrrolo[3,4-c]pyrrole-1,4-dione] (PBDTT-DPP:$PC_{60}BM$). For the P3HT:$PC_{60}BM$ polymer with a band edge at ~ 670 nm, the incorporation of Au/SiO_2 core/shell nanospheres (radius = 20 nm) resulted in a 2.7% improvement in photon conversion efficiency (PCE) while core/shell nanorods (radius = 10 nm) with an aspect ratio (AR) ~ 2.5 (extinction peak, λ_{peak} = 670 nm) resulted in a 7.1% improvement in PCE. For the PBDTT-DPP:$PC_{60}BM$ polymer with a band edge at ~ 830 nm, the incorporation of Au/SiO_2 core/shell nanospheres resulted in a 9.2% improvement, while that of core/shell nanorods (radius = 8 nm) of AR ~ 4 (extinction peak, λ_{peak} = 830 nm) resulted in a 14.4% improvement in PCE. The performance enhancements were corroborated by external quantum efficiency (EQE) measurements.

For cancer therapy applications, the strong light absorption properties of Au nanorods were combined with the upconverting light emission properties of rare earth doped-yttria (RE:Y_2O_3) in order to create hybrid plasmonic/fluorescent core/shell nanorods for dual bio-imaging and photo-thermal therapy applications. The plasmonic/fluorescent Au/SiO_2/Yb:Er:Y_2O_3 core/shell nanorods showed a unique optical signature when excited with 980 nm laser irradiation, exhibiting both the broadband photoluminescence characteristic of Au interband transitions and the sharp emission lines characteristic of the Er^{3+} $^4F_{9/2} \rightarrow {}^4I_{15/2}$ energy transition as well as a 1.81 fold increase in emission intensity compared to SiO_2/Yb:Er:Y_2O_3 nanospheres at 655 nm. Concentrations of 7mM of core/shell nanorods were found to be effective in inducing selective hyperthermia in breast cancer cells both *in-vitro* and *in-vivo* with 5 and 10 minutes respectively of 1.7 W/cm^2 980 nm laser irradiation.

The dissertation of Vladan Janković is approved.

Benjamin S. Williams

Vasilios Manousiouthakis

Jane P. Chang, Chair

University of California, Los Angeles

2014

TABLE OF CONTENTS

CHAPTER 1 INTRODUCTION 1
1.1 Historical Background of Au Nanoparticle Synthesis Methods 6
1.2 Properties of Au Nanoparticles 7
1.3 Au/SiO_2 Core/Shell Nanorods for Plasmonic Light Trapping 23
1.4 Au/SiO_2/Yb:Er:Y_2O_3 Core/Shell Nanorods for Plasmonic Photothermal Therapy .. 41
CHAPTER 2 SIMULATION, SYNTHESIS, CHARACTERIZATION 56
2.1 Simulation to Tailor Optical Properties of Au Nanorods 57
2.2 Synthesis of Au/SiO_2 and Au/SiO_2/Yb:Er:Y_2O_3 Core/Shell Nanorods 80
2.3 Characterization of Au Based Core/Shell Nanorods 90
CHAPTER 3 PLASMONIC LIGHT TRAPPING WITH Au/SiO_2 CORE/SHELL NANORODS 100
3.1 Au/SiO_2 Core/Shell Nanoparticle Synthesis 101
3.2 Plasmonic Organic Photovoltaic Device Fabrication 103
3.3 Plasmonic Organic Photovoltaic Device Characterization 104
CHAPTER 4 PLASMONIC PHOTOTHERMAL THERAPY WITH Au/SiO_2/Yb:Er:Y_2O_3 NANORODS 116
4.1 Synthesis of Spectrally-Tailored Au/SiO_2/Yb:Er:Y_2O_3 Core/Shell Nanorods 118
4.2 Cell Viability and Morphology Evaluation 119
4.3 Optical Characterization 122
4.4 Plasmonic Photo-Thermal Therapy 126
CHAPTER 5 CONCLUSION 133
APPENDICES 138
BIBLIOGRAPHY 153

LIST OF FIGURES

Figure 1.1 Timeline of the four generations of photovoltaic devices, with associated nanomaterial components in the fourth generation devices (Jayawardena, 2013). 2
Figure 1.2 Illustrations of diagnostic, carrier, therapeutic and targeting nanomaterials in medical applications (Menon, 2013)..... 4
Figure 1.3 (a) An illustration of various photo-physical processes in Au nanoparticles. An irradiation induces the excitation of a plasmon resonance mode, resulting in strong light extinction at the local surface plasmon resonance (LSPR) frequency (extinction = scattering + absorption). The optical energy absorbed by the nanoparticle is generally dissipated as heat in electron-phonon collisions or electronic transitions from the d-band to sp-band, generating electron-hole pairs; recombination of separated charges results in luminescence; (b) (i) Photograph of colloidal solutions of Au nanorods of aspect ratios (AR) of ~2.4 to ~5.7; (ii) Corresponding solution extinction spectra; (iii) Discrete dipole approximation simulation of the optical properties of Au nanorods of different diameters; (iv) The dependence of the LSPR wavelength on the aspect ratio (top) and the dependence of scattering quantum yield (scattering efficiency/absorption efficiency) on the aspect ratio (bottom), adapted from (Lee, 2005). 10
Figure 1.4 (a) UV-visible absorbance spectra of Au nanorods with LSPR peaks at 600, 650 and 730 nm are shown as solid curves. UV-visible absorbance spectra of Au nanorods coated with 13 nm-thick silica with LSPR peaks at 615 nm, 665 nm, and 750 nm are shown as dashed curves; (b)-(d) TEM images of 600 nm-resonant Au nanorods, 600 nm-resonant Au nanorods coated with 8 nm silica; (e)-(g) TEM images of 650 nm- Au nanorods, 650 nm- Au nanorods coated with 13 nm silica, adapted from (Li, 2010). 11
Figure 1.5 (a) A schematic illustration of light trapping by Au nanoparticles, adapted from (Atwater 2010); (b) Current characteristic of solar cells without and with gold nanoparticles. Four closely spaced curves represent four separate solar cells with and without nanoparticles, respectively (the cells are shown in the inset), adapted from (Poh, 2011)..... 13
Figure 1.6 (a) A schematic illustration of Au nanorod–based photo-thermal therapy cancer treatment (Zhang, 2012); (b) (i) Viability of the HeLa cells treated with polyethyleneglycol coated Au nanoparticles at various concentrations with (red) or without (green) irradiation using an Ar^+ laser (514.5 nm) at a fluence of 26 W cm^{-2} for 5 min (7.8 kJ cm^{-2}). (ii) Fluorescence microscope images of HeLa cells treated with the Au nanoparticles at various concentrations with irradiation using Ar^+ laser. The living and dead cells emit green and red fluorescence, respectively, adapted from (Nakamura, 2010). 14
Figure 1.7 (a) The TPL image of Au nanorods (blue) in live U2OS cells superimposed on a transmission image (gray scale); (b) Typical 30 min trajectories of single Au nanorods in a live HeLa cell. Adapted from (van den Broek 2013) (c) Linear absorption of the Au nanorods (solid line) compared with the TPL excitation spectrum (solid circles with error bars). The peak at 820 nm corresponds to the

longitudinal plasmon mode. The same power (0.17 mW) was used for all excitation wavelengths, adapted from (Wang, 2005). 15
Figure 1.8 A schematic representation of the response of LSPR biosensors based on refractive index changes: (a) a substrate is chosen, (b) metal nanoparticles are attached to it by means of chemical linkers or nanolithography, (c) the metal particles are modified with the sensor moiety, (d) the analyte are attached specifically onto the recognition function on the particles, causing a change in the refractive index around the particle and an LSPR shift in (e), adapted from (Sepúlveda, 2009). 16
Figure 1.9 SERS detection of cancer cells using immunolabeled Au nanorods. (a) SERS spectra of normal HaCaT cells incubated with anti-EGFR antibody conjugated Au nanorods; (b) SERS spectra of HSC cancer cells incubated with anti-EGFR antibody conjugated Au nanorods. Cancer cells in (b) show stronger, sharper and better resolved SERS signals than normal cells in (a) due to the specific binding of immunolabeled Au nanorods with receptors on the cancer cell surface, suggesting that SERS may serve as a clinical diagnostic tool. The sharper and stronger Raman signals in (b) result from electromagnetic field enhancement due to interparticle coupling between immunolabeled nanorods and their alignment along the cellular membrane surface, adapted from (Huang, 2007)..... 18
Figure 1.10 (a) (i) Diagram of the hybrid nanoparticle architecture (not to scale), indicating dye molecules throughout the silica shell. (ii) Transmission electron microscope image of Au core. (iii), Scanning electron microscope image of Au/silica/dye core–shell nanoparticles. (iv) Spaser mode (in false color), with λ=525 nm and Q = 14.8; the inner and the outer circles represent the 14 nm core and the 44 nm shell, respectively. The field strength color scheme is shown on the right; (b) Normalized extinction (1), excitation (2), spontaneous emission (3), and stimulated emission (4) spectra of Au/silica/dye nanoparticles. The peak extinction cross-section of the nanoparticles is 10^{-12} cm^2. The emission and excitation spectra were measured in a spectrofluorometer at low fluence; adapted from (Noginov, 2009). 19
Figure 1.11 (a) A schematic illustration of light scattering by active layer incorporated, spectrally tuned Au/silica core/shell nanorods for PLT in OPVs. (b) A schematic illustration of light absorption, heat dissipation and rare earth light emission by spectrally tuned plasmonic/fluorescent Au/silica/rare earth doped yttria core/shell nanorods for cancer PPTT. 22
Figure 1.12 (a) Photon induced ionization through excitation of a bound (valence) electron to a higher energy state. (b) Current conduction mechanism in semiconductor materials. 23
Figure 1.13 An illustration of energy levels for electrons showing evolution from discrete atomic energies to bands of allowed states separated by forbidden gaps as the atoms are brought together into a lattice (Sze, 1969). 24
Figure 1.14 Incident solar spectrum and portion absorbed with the corresponding spectral response showing relative contribution of each area from (a-b) 260-micron crystalline silicon and (c-d) 2-micron amorphous silicon..... 31

Figure 1.15 (a) Polymer/fullerene BHJ OPVs by Heeger group, adapted from (Yu 1995) (b) polymer/polymer BHJ OPVs by Friend group, and (c) Device response of MEH-PPV-CN-PPV BHJ OPV, adapted from (Marks, 1994). 33
Figure 1.16 (a) Photo-charge extraction by linearly induced voltage (PCELIV) current transients, collected at different values of *t*delay for a P3HT:PCBM BHJ solar cell with and without Ag nanoparticles. The inset shows the solar cell device efficiency and the charge-carrier mobility for hybrid cells with different concentrations of Ag nanoparticles. The mobility strongly increases with increasing concentration of Ag nanoparticles. (b) Current voltage curves of reference and plasmonic solar cells with various ratios of P3HT:Ag nanoparticles, adapted from (Mei, 2011). 37
Figure 1.17 Maximum attainable values of current density (red) for Si, P3HT, PTB7 and PCPDTBT with an AM 1.5G photon flux (black). The inset summarizes the band gap, maximum wavelength of absorption and maximum attainable photocurrent density for these materials. Adapted from (Chen, 2013)..... 39
Figure 1.18 (a) Schematic illustration of light scattering by spectrally-tuned gold/silica core/shell nanospheres and nanorods (b) EQE of an OPV polymer and extinction spectra of Au nanospheres and nanorods of AR ~ 4 showing spectral overlap between OPV polymer and Au nanoparticles..... 40
Figure 1.19 (a) An illustration and corresponding TEM images of the effect of laser irradiation on Au nanorods (top) and Au/silica core/shell nanorods (bottom) Adapted from (Hu 2011) (b) TEM images bare Au nanorods and Au/SiO_2 core/shell nanorods along with optical absorption spectra for bare Au nanorods and Au/SiO_2 core/shell nanorods before and after exposure with 21.20 m*J*/cm^2 of 785 nm laser irradiation (Chen, 2010). 44
Figure 1.20 (a) Energy scheme with the relevant processes of energy transfer UC in Yb^{3+}/Er^{3+} codoped materials: energy transfers, radiative, multiphonon processes, and cross-relaxation are depicted in dashed, full, dotted, and curly lines, respectively. The high efficiency in the upconverter is achieved by the absorption of the photons by the Yb^{3+} ions followed by the transfer of the excitation to the Er^{3+}(Schietinger 2009) (b) Live-cell imaging of Yb:Er:$NaYF_4$ in NIH 3T3 murine fibroblasts. (i) Brightfield image of a cell with endocytosed Yb:Er:$NaYF_4$, (ii) upconverted luminescence following 980-nm excitation, and (iii) overlay of (i) and (ii). (iv) Brightfield image of a cell without Yb:Er:$NaYF_4$, (v) upconverted luminescence following 980-nm excitation, and (vi) cellular autofluorescence following 532-nm excitation. All images are shown on the same intensity scale (Scale bar, 10 μm), adapted from (Wu, 2009)..... 47
Figure 1.21 (a) An illustration of energy transitions involved in upconversion using Yb^{3+} as a sensitizer and Tm^{3+} as the emitter (Zhang, 2010). (b) *In-vitro* bioimaging of photosensitizer: colloidal NCs in HeLa cells. HeLa cells were incubated with (at 37 °C (i) or at 4 °C (ii)) and without (ii) Yb:Tm:$NaYF_4$ NCs. All the concentration of photo-sensitizer colloidal NCs was 10 μgmL^{-1} and the incubation time was 3 h. The four panels from left to right in each line (a–c) are the false-colored fluorescent images of Hoechst 33258, visible (400 − 700 nm) and NIR (720 − 880 nm) UC emission of Yb:Tm:$NaYF_4$ NCs, and the merged images, respectively, adapted from (Zhou, 2011). 48

Figure 1.22 Upconversion spectra of Ag-core/SiO_2-spacer/20 nm-Y_2O_3 (a) Ag-50nm/SiO_2-30nm/Er:Y_2O_3 (b) No Ag, Er:Y_2O_3 (c) Ag-50nm/SiO_2-70nm/Er:Y_2O_3 (d) Ag-130nm/Er:Y_2O_3 (e) Ag-50nm/Er:Y_2O_3 and (f) Ag-20nm/Er:Y_2O_3 (b) Enhancement factors (EF) averaged between 550 and 650 nm for the three Ag sizes, and (black trace) normalized integrated green to red intensity ratio (Band Ratio) for Ag-50nm/SiO_2-30nm/Y_2O_3:Er as a function of the SiO_2 spacer thickness. (c) Band ratio versus EF at 550 nm for the three Ag cores/spacers with an EF less than or equal to the maximum. (d) Prostate cancer cell imaging after overnight incubation with particles and cell viability graph as inset, adapted from (Zhang, 2010). 50
Figure 1.23 UV-vis-NIR absorption spectra of (a) Er:Y2O3 hollow nanospheres; (b) Ag-50nm/Er:Y2O3 hollow nanospheres; (c) Ag-50nm/SiO2-30nm/Er:Y2O3 hollow nanosphere; (d) Ag-50nm/SiO2-70nm/Er:Y2O3 nanospheres; (e) Ag-50nm/SiO2 nanospheres and (f) 50 nm Ag nanoparticles, adapted from (Zhang, 2010)..... 51
Figure 1.24 (a) Absorption spectra of Au-shell encapsulated silica coated Yb:Er:$NaYF_4$ (b) Fluorescence spectra of silica coated Yb:Er:$NaYF_4$ before and after encapsulation with Au nanoshells with different thickness and SPR peaks. For all the fluorescence measurements, the concentration was fixed at 20 μM $NaYF_4$ nanocrystals and the laser excitation density was 35 $mWcm^{-2}$. Adapted from (Priyam, 2012). 52
Figure 1.25 (a) A schematic illustration of light absorption, heat dissipation and rare earth light emission by spectrally tuned plasmonic/fluorescent gold/silica/rare earth doped yttria core/shell nanorods for cancer photothermal therapy and bioimaging (b) Normalized absorption spectra of blood, fat and water along with experimentally measured emission spectra of $^4F_{9/2} \rightarrow {}^4I_{15/2}$ energy transition of Er^{3+} (655nm) 53
Figure 1.26 (a) A schematic illustration of light scattering by active layer incorporated, spectrally tuned Au/SiO_2 core/shell nanorods for OPV light trapping (b) A schematic illustration of light absorption, heat dissipation and rare earth ion light emission by spectrally tuned Au/SiO_2/Yb:Er:Tm:Y_2O_3 core/shell nanorods for photo-thermal tumor therapy. 55
Figure 2.1 Dielectric permittivity as a function of frequency. ε′ and ε″ denote the real and the imaginary part of the permittivity, respectively. Adapted from (Johnson, 1972). 58
Figure 2.2 (a) Real (ε') and imaginary (ε") dielectric permittivity functions of Au and Ag. (b) Reflectivity of Au and Ag as a function of frequency. 61
Figure 2.3 Experimentally obtained values (symbols) of real ε' and imaginary ε" dielectric permittivity from a 100nm thin Au film and the Drude model (lines). 61
Figure 2.4 Calculated absorption and scattering cross-sections of gold nanospheres in water as a function of diameter (El-Sayed, 2001)..... 65
Figure 2.5 The arrangement of electric and magnetic field nodes in space and time. The electric field nodes are shown as circles and the magnetic field nodes are shown as triangles. The indicated point is expanded to obtain an update equation for H_y 66
Figure 2.6 (a) Simulated absorption and scattering cross sections of Au/SiO_2 ellipsoids of different aspect ratios (transverse ellipsoid diameter is each spectrum is 10nm). Simulated (b) absorption and (c) scattering cross sections of Au/SiO_2 ellipsoids of aspect ratio 2.5 but with different (transverse ellipsoid diameter is shown next to

absorption cross section) (d) Absorption sections of Au/SiO_2 core/shell nanorods (aspect ratios 2.5 and 4, SiO_2 shell thickness 10 nm) along with emission cross sections of the $^4F_{9/2} \rightarrow {}^4I_{15/2}$ energy transition of an Er^{3+} ion (peak at 655nm) and the $^3H_4 \rightarrow {}^3H_6$ energy transition of a Tm^{3+} ion (peak at 805nm)..... 69
Figure 2.7 Simulation of Au/SiO_2 core/shell nanorods with Au cores of 12 nm and 30 nm in length (AR=2.5) and a 10 nm thick SiO_2 shell. The left column are off resonance (850 nm) near field simulation results for (a) ZY (c) ZX (e) YX orientations. The right column are on-resonance (655 nm) near field simulation results for (b) ZY (d) ZX (f) YX orientations..... 74
Figure 2.8 Simulation of Au/SiO_2 core/shell nanorods with Au cores of 12 nm and 30 nm in length (AR=2.5) and a 5 nm thick SiO_2 shell. The left column are off resonance (850 nm) near field simulation results for (a) ZY (c) ZX (e) YX orientations. The right column are on-resonance (655 nm) near field simulation results for (b) ZY (d) ZX (f) YX orientations..... 75
Figure 2.9 Simulation of Au/SiO_2 core/shell nanorods with Au cores of 12 nm diameter and 48 nm in length (AR=4) and a 10 nm thick SiO_2 shell. The left column are off resonance (555 nm) near field simulation results for (a) ZY (c) ZX (e) YX orientations. The right column are on-resonance (800 nm) near field simulation results for (b) ZY (d) ZX (f) YX orientations..... 76
Figure 2.10 Simulation of Au/SiO_2 core/shell nanorods with Au cores of 12 nm diameter and 48 nm in length (AR=4) and a 5 nm thick SiO_2 shell. The left column are off resonance (555 nm) near field simulation results for (a) ZY (c) ZX (e) YX orientations. The right column are on-resonance (800 nm) near field simulation results for (b) ZY (d) ZX (f) YX orientations..... 77
Figure 2.11 (a) Illustration of an Au nanorod with a CTAB bilayer attached (Alkilany, 2012) (b) Illustration of an Au nanoparticle in solution showing how counterions arrange themselves in response to a charged particle and the potential difference as a function of distance in the solution from the charged particle..... 81
Figure 2.12 (a) Schematic illustration of the seed-mediated method for the growth of Au nanorods(Chen 2013) (b) Proposed growth mechanism of Au nanorods from an Au seed Adapted from (Alkilany 2010). 84
Figure 2.13 (a) Au nanorod aspect ratio and peak extinction wavelength as a function of $AgNO_3$ precursor amount (b) Au nanorod aspect ratio and peak extinction wavelength as a function of $C_6H_8O_6$ precursor amount (c) Au nanorod longitudinal peak extinction intensity as a function of $AgNO_3$ amount, and (d) FDTD, empirical and experimentally obtained relationships between Au nanorod aspect ratio and the longitudinal plasmon peak wavelength..... 85
Figure 2.14 (a) Diagrams of molecular structures of CTAB, PSS, PAH and PVP surfactants (b) Zeta potential measurements of Au/CTAB, Au/PSS, Au/PAH and Au/PVP nanorods at pH 7, adapted from (Pastoriza-Santos 2006) 88
Figure 2.15 (a) Schematic diagram of SiO_2 coating process for Au nanospheres and Au nanorods of different aspect ratios (b) Mass of TEOS needed to coat 10, 20 and 30 nm SiO_2 shells on Au nanospheres and Au nanorods of 10nm radius and 30, 40 and 50nm lengths (10 ml, 0.5mM $AuCl_3$ basis). 89

Figure 2.16 (a) Schematic diagram of $Au/SiO_2/Yb:Er:Y_2O_3$ core/shell nanorod synthesis procedure (b) Mass of Y_2O_3 needed to coat 5, 10 and 15 nm Y_3O_3 shells on Au nanospheres and Au nanorods of 10nm radius and 30, 40 and 50nm lengths (10 ml, 0.5mM $AuCl_3$ basis)..... 90
Figure 2.17 (a) Schematic diagram of a transmission electron microscope (TEM) (b) From left to right, TEM images of Au nanospheres, AR ~ 2.5 nanorods and AR ~ 4 nanorods (c) From left to right, TEM images of Au/SiO_2 nanospheres, AR ~ 2.5 and AR ~ 4 Au/SiO_2 core/shell nanorods..... 92
Figure 2.18 (a) Schematic diagram of a UV-Vis absorption spectrometer showing the main components of the system: a broadband light source (lamp), a monochromator, a sample cuvette and a photodetector (b) Extinction spectra of Au nanospheres (20 nm diameter), Au nanorods of aspect ratio ~ 2.5 (15 nm diameter, 37 nm length) and Au nanorods of aspect ratio ~4 (10 nm diameter, 40 nm length). 93
Figure 2.19 (a) Schematic diagram of an experimental setup used to measure upconversion photoluminescence (b) Upconversion spectra of Au/SiO_2 nanorods (15 nm diameter, 40 nm length, 5 nm SiO_2 shell thickness) as a function of excitation power..... 95
Figure 2.20 (a) Simplified time correlated single photon counting (TCSPC) experimental setup (b) Radiative lifetime measurements of $SiO_2/Yb:Er:Y_2O_3$ and $Au/SiO_2/Yb:Er:Y_2O_3$ core/shell nanoparticles..... 97
Figure 2.21 (a) Schematic diagram of an experimental setup used to measure photoluminescence; (b) Sample EQE spectrum of PBDTT-DPP:$PC_{60}BM$ and PBDTT-DPP:$PC_{60}BM$ with Au/SiO_2 core/shell nanorods embedded in the active layer..... 98
Figure 2.22 (a) Experimental setup used to measure photothermal energy conversion of Au, Au/SiO_2 and $Au/SiO_2/Yb:Er:Y_2O_3$ nanorods; (b) Photo-thermal heating rates of 400μl colloidal solutions of 14 mM, 7 mM, 1.75 mM Au/PVP nanorods and a control (H_2O). 99
Figure 3.1 (a) TEM images and (b) Extinction spectra of various colloidal solutions: (A) Au nanospheres in water (B) Au nanorods of AR~2.5 in water (C) Au nanorods of AR~4 in water (D) Au/SiO_2 core/shell nanospheres in DCB (E) Au/SiO_2 nanorods of AR ~2.5 in DCB (F) Au/SiO_2 nanorods of AR ~4 in DCB; (c) EQE of P3HT:$PC_{60}BM$ plotted with normalized extinction spectra from solutions D and E; (d) EQE of PBDTT-DPP:$PC_{60}BM$ devices plotted with normalized extinction spectra from solutions D and F; (e) EQE from (e) P3HT:$PC_{60}BM$ with solutions D, E and reference (f) PBDTT-DPP:$PC_{60}BM$ with solutions D, F and reference. 106
Figure 3.2 Spectral EQE enhancements of (a) P3HT-based device with Au/SiO_2 nanospheres (solution D) (b) PBDTT-DPP-based device with solution Au/SiO_2 nanospheres (solution D) (c) P3HT-based device with AR~2.5 Au/SiO_2 core/shell nanorods (solution E) (d) PBDTT-DPP-based device with AR~4 Au/SiO_2 core/shell nanorods (solution F)..... 107
Figure 3.3 Solar cell PCE as a function of Au/SiO_2 nanosphere and nanorod concentrations for (a) D in P3HT:$PC_{60}BM$ (b) D in PBDTT-DPP:$PC_{60}BM$ (c) E in P3HT:$PC_{60}BM$ and (d) F in PBDTT-DPP:$PC_{60}BM$. 110

Figure 3.4 Atomic force microscopy images of P3HT:$PCB_{60}M$ devices (the left column is the height image and the right column the phase image): (a-b) Reference device, (c-d) Device with 0.6 mg/ml Au/SiO_2 nanospheres, and (e-f) Device with 3 mg/ml Au/SiO_2 nanospheres. 112
Figure 3.5 Atomic force microscopy image of PBDTT-DPP:$PCB_{60}M$ devices (the left column is the height image and the right column the phase image): (a-b) Reference device, (c-d) Device with 0.6 mg/ml Au/SiO_2 nanospheres, and (e-f) Device with 1 mg/ml Au/SiO_2 nanospheres. 113
Figure 4.1 (a) Normalized extinction spectra of $Au/SiO_2/Yb:Er:Y_2O_3$, $SiO_2/Yb:Er:Y_2O_3$ and Au/SiO_2 solutions along with emission spectrum associated with the Er^{3+} $^4F_{9/2} \rightarrow {}^4I_{15/2}$ radiative energy transition (b) EDX of $Au/SiO_2/Yb:Er:Y_2O_3$ core/shell nanorods. (c) From left to right: TEM image of (A) Au/SiO_2 (B) $SiO_2/Yb:Er:Y_2O_3$ and (C) $Au/SiO_2/Yb:Er:Y_2O_3$ 123
Figure 4.2 Upconversion power spectra (980nm laser diode excitation) of (a) Au/SiO_2, (b) $SiO_2/Yb:Er:Y_2O_3$. 124
Figure 4.3 Upconversion power spectra (980nm laser diode excitation) of $Au/SiO_2/Yb:Er:Y_2O_3$. 125
Figure 4.4 (a) Power dependence spectra of samples $Au/SiO_2/Yb:Er:Y_2O_3$, $SiO_2/Yb:Er:Y_2O_3$ and Au/SiO_2. (b) The radiative lifetime measurements for $Au/SiO_2/Yb:Er:Y_2O_3$ and $SiO_2/Yb:Er:Y_2O_3$. 126
Figure 4.5 (a) Photo-thermal properties of 400 μl of control (0 mM), 1.75 mM, 7 mM and 14 mM Au/PSS nanorods (b) Cell viability of breast cancer cells after incubation with 0 mM, 1.75 mM, 7 mM and 14 mM Au/PSS nanorods. 127
Figure 4.6 (a) Photo-thermal properties of 7 mM Au/PSS and $Au/SiO_2/Yb:Er:Y_2O_3$ core/shell nanorods (b) Cell viability of 7 mM Au/PSS, Au/PAH, Au/PVP, Au/SiO_2 and $Au/SiO_2/Yb:Er:Y_2O_3$ nanorods. 128
Figure 4.7 (a) Photograph of tumor cells without (left) and with 5 minutes of 1.7 W/cm^2 laser irradiation (right). (b) Cyto-toxicity assay results of breast cancer tumors with 7 mM Au/PAH, Au/PVP, Au/SiO_2 and $Au/SiO_2/Yb:Er:Y_2O_3$ nanorods prior to laser irradiation and after 5 min of 1.7 W/cm^2 980nm laser irradiation. 130
Figure 4.8 (a) Photograph (left) and near infra-red scope image (right) of an athymic nude mouse with a MDA MB 231 breast cancer tumor on its back receiving laser treatment (b) (A) Histology cross section of breast cancer tumor explanted from mouse model after 10 minutes of 1.7 W/cm^2 laser irradiation of a tumor section into which 100 μl of 10mM Au/PVP nanorods were injected (left) and area which received laser treatment but was not injected with Au/PVP nanorods (right). 131

LIST OF TABLES

Table 1.1 Typical minority carrier diffusion lengths for c-Si, a-Si (Sze, 1969) 30
Table 1.2 Summary of Plasmonic Light Trapping in OPV devices 36
Table 1.3 Summary of Au nanorod-based photo-thermal therapy results 46
Table 3.1 Gold/Silica Core/Shell Nanospheres (radius=20 nm) 109
Table 3.2 Gold/Silica Core/Shell Nanospheres (radius=20 nm) 109
Table 3.3 Gold/Silica Core/Shell Nanorods of AR~2.5 (radius=10 nm) 109
Table 3.4 Gold/Silica Core/Shell Nanorods of AR~4 (radius=8 nm) 109
Table 4.1 Summary of sample parameters for Au/SiO_2 and Au/SiO_2/Yb:Er:Y_2O_3 core/shell nanorods and SiO_2/Yb:Er:Y_2O_3 core/shell nanospheres 122

ACKNOWLEDGEMENTS

I would like to thank Professor Jane Chang for her mentorship, advice and support; it has been an honor and privilege to work with you.

I would like to thank Professor Benjamin Williams, Professor Selim Senkan and Professor Vasilios Manousiouthakis for serving on my committee.

I would like to acknowledge funding support from the Northrop Grumman PhD Fellowship and from the U.S. Department of Energy under Award No. ER46658 and BES-114229.

I would like to thank Professor Yang Yang and Michael Yang in the Materials Science and Engineering Department for their support and assistance on the photo-voltaic portion of the work.

I would like to thank Professor Bo Han and Josephine Fang in the Department of Surgery at USC for their help and advice on the photo-thermal tumor therapy portion of the work.

I would like to thank my Northrop Grumman colleagues, especially Luke Sweatlock, James Ma, Seth Taylor, Erik Antonsson and Hiroshi Komine for their assistance and advice.

I would like to thank my lab mates over the years for all the hilarious moments, serious talks, help, intellectual needling, companionship and friendship, especially: Cyrus, Jay, Colin, James, Nathan, Sandy, Calvin, Jack, Diana, Taeseung, Ju, John, Ryan, Trinh, Carey, Wilson and Ragesh.

I would like to thank my family and friends for their help, encouragement and support: Aleksandar, Tatjana, Tamara, Nebojša, Carl, Julie, Ana, Joe, Stevan, Boris, Antonio, Lino, Pablo, Matt, Sam, Jeff, Tom, Ruth, Ružica and Vesna.

Finally, I would like to thank Banafsheh for her love, kindness, patience and grace. This would not have been possible without you.

CURRICULUM VITA

1997-2001	B.S., Chemical Engineering University of Nevada, Reno
2001-2004	M.S., Chemical Engineering University of California, Los Angeles
2004-2006	Junior Materials & Process Engineer Northrop Grumman Aerospace Systems
2006-2008	Senior Materials & Process Engineer Northrop Grumman Aerospace Systems
2008-2012	Research Scientist Northrop Grumman Aerospace Systems
2009-2013	Graduate Student Researcher University of California, Los Angeles
2012-Present	Senior Materials & Process Engineer Northrop Grumman Aerospace Systems

PATENTS, PUBLICATIONS & PRESENTATIONS

Janković, V.; Fang, J.; Cheung, P.L.; Han B. and Chang, J.P. "Plasmonic Core/Shell Nanorods for Photo-Thermal Tumor Therapy," AIChE Annual Meeting, San Francisco, USA (2013)

Janković, V.; Yang, Y.; Cheung, P.L.; Chang, J.P. and Yang, Y. "Active Layer-Incorporated, Spectrally-Tuned Nanostructure-based Light Trapping for Organic Photovoltaic Devices," 61780232, provisional patent filed on 3.13.2013

Janković, V.; Yang, Y.; You, J.; Dou, L.; Liu, Y.; Cheung, P.L..; Chang, J.P. and Yang, Y. "Active Layer-Incorporated, Spectrally-Tuned Au/SiO_2 Core/Shell Nanorod-based Light Trapping for Organic Photovoltaics," ACS Nano 7, 5 (2013)

Janković, V.; Yang, Y.; Cheung, P.L.; Chang, J.P. and Yang, Y. "Au/SiO_2 Core/Shell Nanorods for Light Trapping in Organic Photovoltaics," AIChE Annual Meeting, Pittsburgh, USA (2012)

Sweatlock, L; Diest, K; Janković, V; Ma, J; Pryce, I; Briggs, R. and Atwater, H. "Plasmonic, Thermo-Optic and Electro-Optic Modulator Employing Solid State Phase Change Active Media," 4136804, provisional patent filed on 12.15.2011

Janković, V. and Chang, J.P. "Core/Shell Nanoparticle Optical Antenna," MRS Spring Meeting, San Francisco, USA (2011)

Janković, V. and Chang, J.P. "HfO_2 and ZrO_2-based Microchemical Ion Sensitive Field Effect Transistor (ISFET) Sensors: Simulation & Experiment," Journal of the Electrochemical Society 158, 11 (2011)

Dicken, M.; Pryce, I.; Janković, V.; Sweatlock, L.; Ma, J. and Atwater, H. "Development of Vanadium Oxide-Based Functional Media for Active Infrared Metamaterials," 4th International Conference of Surface Plasmon Photonics (SPP4), Amsterdam, Holland (2009)

Janković, V. and Chang, J.P. "Integrated Ion Sensitive Field Effect Transistor (ISFET) Microchemical Sensor and Electrowetting on Dielectric (EWOD) Microfluidic Actuator Using Ultra-Thin Zirconium Oxide and Hafnium Oxide Films," 208th Annual Meeting of the Electrochemical Society, Los Angeles, USA (2005)

Nowling, G.R.; Babayan S.E.; Janković, V. and Hicks, R.F. "Remote Plasma-Enhanced Chemical Vapor Deposition of Silicon Nitride at Atmospheric Pressure," Plasma Sources Science & Technology 11, 7 (2002)

CHAPTER 1 INTRODUCTION

Two issues that our society cares deeply about are renewable energy generation and health care. Renewable energy can allay air pollution and global warming concerns, while effective medical treatments can increase the longevity and quality of life. Developments in nanomaterial technology in the past decade has provided scientists, engineers and medical doctors with new tools and techniques to tackle pressing technological challenges in these areas.

In the renewable energy sector, nanomaterials have transformed solar technology in such a radical way that researchers in the area are referring to solar cells that incorporate nanomaterials as fourth generation photovoltaics (Jayawardena, 2013). First generation solar cells, developed in the 1960s, based on thick (>200 nm) Si crystalline films, have high efficiencies (>20%) but the materials and fabrication processes are too expensive to compete with fossil fuel-based energy. Second generation solar cells, developed in the 1980s and based on amorphous or polycrystalline silicon (Si), copper indium gallium (di)selenide (CIGS), and cadmium telluride (CdTe), reduced the high costs prevalent in first generation cells by diminishing the quality and quantity of the materials used in the fabrication of devices but the device efficiencies dropped significantly. Third generation solar cells, developed in the 1990s, took advantage of scalable materials and manufacturing techniques like organic photovoltaic (OPV) and dye-sensisitized solar cell (DSCC) technologies to further reduce cost and are becoming more competitive as their efficiencies keep climbing. Fourth generation solar technology aims to improve on the efficiency and durability of second and third generation solar cells

by incorporating nanomaterials into device architectures in the form of more efficient electron accepting layers, scalable and inexpensive transparent conducting electrodes, or as light trapping nanostructures (Kao, 2012). Figure 1.1 shows illustrations of the different generations of solar technology and nanomaterials being considered for fourth generation solar cell device architectures: quantum dots (QDs), metal oxide nanoparticles (TiO_x, MoO_3, V_2O_5, ZnO), graphene, carbon nanotubes (CNTs) and metal nanoparticles (NPs).

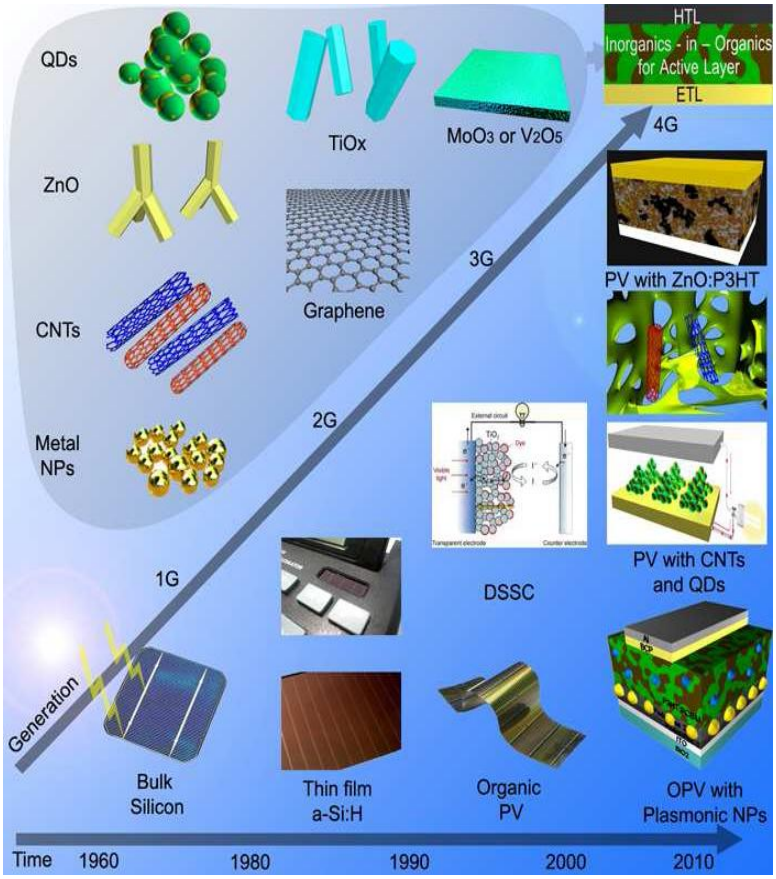


Figure 1.1 Timeline of the four generations of photovoltaic devices, with associated nanomaterial components in the fourth generation devices (Jayawardena, 2013).

For example, quantum dots (QDs) absorb a useful range of solar spectrum and are efficient electron acceptors in combination with conjugated polymers, however, the low electron mobility of QD networks (10^{-5} $cm^2V^{-1}s^{-1}$) currently limits the highest attainable efficiency by QD/OPV hybrid architectures to ~ 3.2% (Dayal, 2010). Nanostructured metal oxides have also found use as electron acceptors in combination with conjugated polymers, but the efficiencies of hybrid metal oxide/OPV devices still lag behind third generation PV technology at ~ 3% (Liao, 2012; Moon, 2011). Graphene shows promise as an ultra-thin and inexpensive transparent conductive electrode due to its low sheet resistance of 280 Ω/sq (Kim, 2009) and a transparency greater than 95% at visible frequencies, but processing technology is currently not compatible with roll to roll fabrication (Bae, 2010; Park, 2011). Silver nanowire networks are promising candidates as solution-processable transparent conductors (Zhu, 2011) with sheet resistances of 11 Ω/sq and a transparency of 87% at visible frequencies (Sahin, 2013) while carbon nanotubes (CNTs) show promise as efficient charge transport pathways inside active layers (Chaudhary, 2007; Dabera, 2012; Li, 2012; Lu, 2013). Finally, metal nanoparticles (NPs) of various sizes, shapes and configurations have been successfully integrated into OPV cell architectures in order to tune and enhance, in a wavelength-dependent manner, the optical absorption of OPV devices (Choi, 2013; Li, 2013; Janković, 2013; Xu, 2013; Stratakis, 2013).

It is clear that nanomaterials play a key role in improving both light coupling and charge extraction in second and third generation solar cell designs and as various synergies between material properties are discovered, more efficient and more durable solar cells can be achieved.

Besides revolutionizing the solar industry, nanomaterials are also having an impact in the health care industry (Menon, 2013). A wide variety of bio-compatible nanoparticles have been synthesized (Figure 1.2).

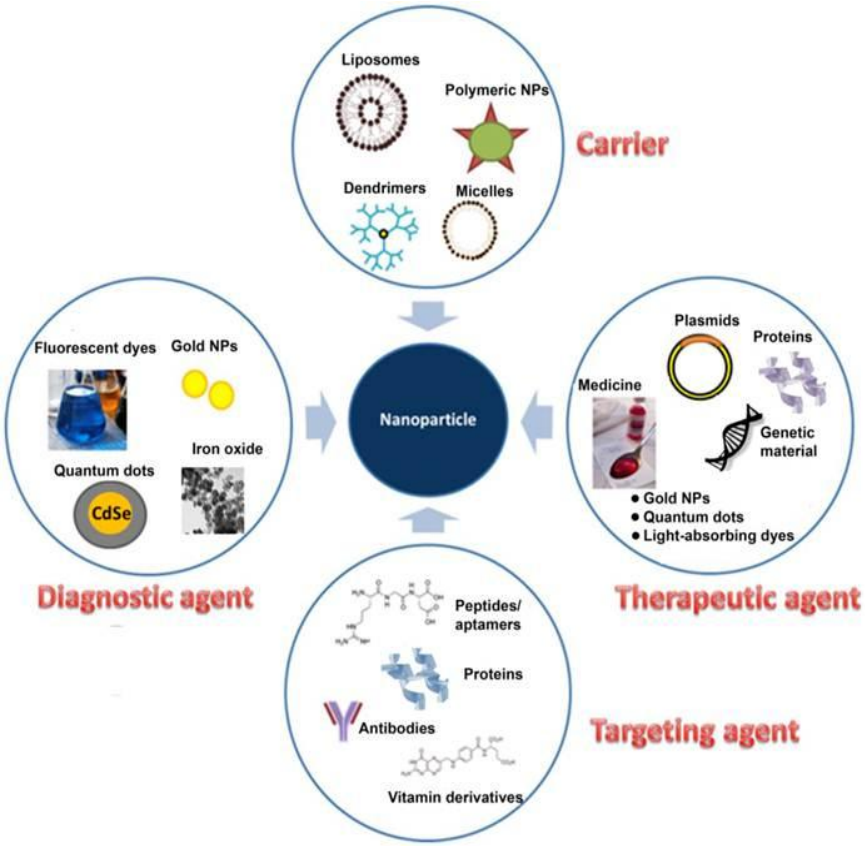


Figure 1.2 Illustrations of diagnostic, carrier, therapeutic and targeting nanomaterials in medical applications (Menon, 2013).

Nanoparticles for medical applications can be classified into carrier, diagnostic, targeting or therapeutic agents. Liposomes, dendrimers, emulsions, and other polymers are used as carrier vehicles of targeting and therapeutic agents for controlled protein and macromolecule release in the body while inorganic nanomaterials have found use in diagnostic and therapeutic purposes (Sanvicens, 2008; Huang, 2011). In general, inorganic nanoparticles have a central core that defines the fluorescent, optical, magnetic,

and electronic properties of the particle and a protective organic coating or shell on the surface that protects the inorganic core from degradation in physiological environments and can form electrostatic or covalent bonds with charged agents and biomolecules that have basic functional groups such as amines and thiols (Yezhelyev, 2006; de Dios, 2010).

Functionalized quantum dots, for example have been employed as high contrast probes in optical tumor imaging (Aswathy, 2010; Rogach, 2010; Wang, 2010), while functionalized magnetic nanoparticles have found utility as contrast agents in magnetic resonance imaging (MRI) (Lu, 2007; Sotiriou, 2011). Noble metal nanoparticles, on the other hand, have found utility in photo-thermal therapy due to fact that they radiate heat when exposed to laser light (Choi, 2011; Dreaden, 2012).

Research in biomedical nanomaterials is now gravitating toward hybrid nanomaterials. Hybrid nanomaterials combine two or more functionalities within the same nanoparticle and have demonstrated advantageous properties and novel functionalities compared to single-component nanoparticles (Timothy, 2007; Sortino, 2012). For example, hybrid plasmonic/magnetic nanomaterials can be guided to the diseased tissue by an externally applied magnetic field and once in place optically activated (Peng, 2011; Sotiriou 2011), while plasmonic/fluorescent hybrid nanomaterials have potential as simultaneous diagnosis and therapy agents (Saha, 2009; Schietinger, 2009; Zhang, 2010; Wang, 2011; Wu, 2011).

In the next section, a historical overview of gold nanoparticle synthesis is provided followed by a description of the unique properties of gold nanoparticles. In depth literature reviews of research on gold nanoparticle applications in solar cells and for cancer photothermal therapy are provided at the end of this chapter.

1.1 Historical Background of Au Nanoparticle Synthesis Methods

The use of metal nanoparticles can be traced back to the Roman times and the invention of stained glass. Before understanding the origin, Roman glassmakers discovered that adding gold powders to a glass melt would impart a deep red or violet color to the glass and stained glass developed as an art form. It was only in 1850 that Michael Faraday realized that the color was due to the fact that the gold was present in a finely dispersed state and was the first to demonstrate synthesis of colored colloids by the reduction of gold (Au) salts (Faraday, 1857). After the advent of the transmission electron microscope (TEM) in the early 1950s, the first structural studies of Au nanoparticles were performed by Turkevich *et.al.* (Turkevich, 1951).

Researchers continued to develop various techniques of synthesizing Au nanoparticles. Schmid *et.al.* showed that phosphine-stabilized Au nanoparticles with ~ 2 nm diameter could be produced from the reduction of chloro(triphenylphosphine)gold(I) (PPh_3AuCl) by diborane in benzene (Schmid, 1981), while Weare *et.al.* reported that Au clusters of 2 to 10 nm in diameter could be obtained via a ligand exchange method (Weare, 2000). Brust *et.al.* demonstrated synthesis of thiol-stabilized Au clusters using a two-phase system in which $AuCl_3$ was solvated in toluene by way of a phase-transfer reagent (tetraoctylammonium bromide) (Brust, 1994).

Interest in shape-controlled synthesis of Au nanostructures began in the early 1990's motivated by advances in nanotechnology and the unique and spectrally tunable light scattering and absorption properties of ellipsoidal metal nanoparticles predicted by theoretical calculations (Gans, 1912). Masuda *et.al.* and Martin *et.al.* developed the first techniques to prepare colloidal Au nanorods (~ 30 nm in diameter, 50-100 nm in length)

in solution by the electrochemical reduction of gold chloride ($HAuCl_4$) into nanoporous aluminum oxide (Al_2O_3) membranes (Masuda, 1990; Martin, 1991). Yu *et.al.* later demonstrated the synthesis of much smaller Au nanorods (~ 10 nm in diameter) by electrochemical oxidation of an Au plate electrode in the presence of cationic, quaternary ammonium surfactants (cetyltrimethylammonium bromide (CTAB) and tetraoctylammonium bromide (TOAB)) under ultra-sonication (Yu, 1997).

In 2003, Nikoobakht and El-Sayed demonstrated a colloidal growth method to produce monodisperse Au nanorods in high yield based on seeded growth (Nikoobakht, 2003). In their method, single-crystal Au seed nanoparticles of ~ 1.5 nm in diameter, produced from the reduction of chloroauric acid ($HAuCl_4$) by sodium borohydride ($NaBH_4$) in the presence of CTAB, are pipetted into an Au(I) growth solution prepared from the mild reduction of $HAuCl_4$ by ascorbic acid ($C_6H_8O_6$) and the addition of silver nitrate ($AgNO_3$) and CTAB. The protocol produces Au nanorods 10 – 20 nm in diameter and up to 100 nm in length. The nanorod aspect ratio is controlled by the seed to salt ratio and by the relative concentration of Ag^+ additive impurity ions. TEM analysis indicated that the Au nanorods grow along the [001] direction, which has less stable crystalline facets along the sides of the rods and more stable crystalline facets at the tips (Wang, 1999).

In the next section, the origin of the unique optical properties of Au nanospheres and nanorods is discussed.

1.2 Properties of Au Nanoparticles

The unique optical properties of Au nanoparticle colloid solutions arise from the interaction between light and the Au nanoparticle free electrons. The oscillating

electromagnetic field of light periodically displaces electrons from their equilibrium positions in the positive metal ion lattice; at the same time, the positive ions in the metal lattice exert a restoring force on the electrons. If the electron cloud is confined in dimensions that are smaller than the wavelength of the incident light (as in the case of a nanoparticle), the light-resonant displacement of the electrons with respect to the positively charged lattice gives rise to a charge oscillation, termed the local surface plasmon resonance (LSPR). At the LSPR frequency, these resonant electron oscillations lead to strong light absorption and scattering in a fairly narrow wavelength range (~ 100 nm full width half max). The absorbed light is generally dissipated as heat in electron-phonon collisions, while the scattered light is re-emitted into the environment at the same frequency as the incident light (Chen, 2013). The LSPR oscillation frequency depends on the dielectric permittivity, the geometry of the nanoparticle and the dielectric permittivity of the medium (Lee, 2005). Lower LSPR frequencies result when the electron gas is confined in larger nanoparticle geometries, while higher LSPR frequencies are the result of confinement of the electron gas in smaller nanoparticle geometries. For example, colloids of Au nanorods of diameter 15 nm and length 30 nm exhibit peak light absorption and scattering at wavelengths of ~ 620 nm, while Au nanorods of diameter 15 nm and length 60 nm exhibit peak absorption and scattering at wavelengths of ~ 800 nm. Since spectrophotometers typically measure the sum of the absorption and scattering intensities of a nanoparticle colloid, it is common to refer to the sum of absorption and scattering as extinction. The relative contributions of absorption versus scattering depend on the nanoparticle geometry. Smaller nanoparticles (< 30 nm) generally absorb the majority of incident light while larger nanoparticles (> 30 nm) scatter a greater portion of

the incident light (El-Sayed, 2001). Spherical particles tend to absorb a larger proportion of light than ellipsoidal or rod-shaped nanoparticles (El Sayed, 2007).

Besides resonantly enhanced extinction, resonant electron oscillations at the LSPR frequency also lead to a highly enhanced electromagnetic field in the vicinity of the metal nanoparticle, termed the near field. The near field increases the probability of electronic transitions from the d band to the sp band in Au, generating electron-hole pairs whose subsequent recombination results in luminescence. (Boyd, 1984; Mohamed, 2000; El-Sayed, 2001; Beversluis, 2003; Bouhelier, 2003; Dulkeith, 2004). A schematic diagram of the dipole oscillations induced in a metal nanoparticle under illumination and the three energy pathways available to the incident energy (scattering, absorption and luminescence) is shown in Figure 1.3 (a). The extinction spectra of Au nanorod solutions of different aspect ratios and the relative contributions of absorption and light scattering as a function of aspect ratio are shown in Figure 1.3(b).

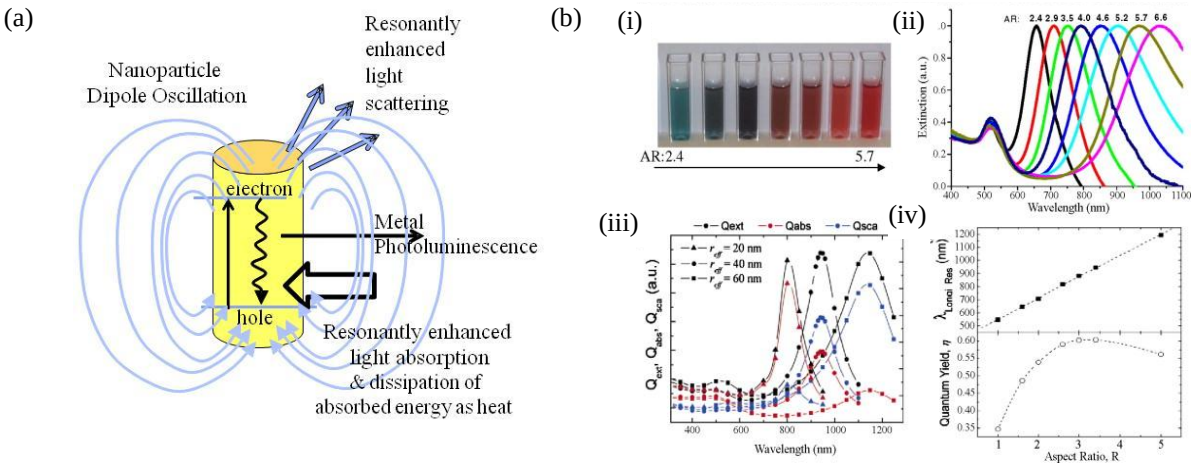


Figure 1.3 (a) An illustration of various photo-physical processes in Au nanoparticles. An irradiation induces the excitation of a plasmon resonance mode, resulting in strong light extinction at the local surface plasmon resonance (LSPR) frequency (extinction = scattering + absorption). The optical energy absorbed by the nanoparticle is generally dissipated as heat in electron-phonon collisions or electronic transitions from the d-band to sp-band, generating electron-hole pairs; recombination of separated charges results in luminescence; (b) (i) Photograph of colloidal solutions of Au nanorods of aspect ratios (AR) of ~2.4 to ~5.7; (ii) Corresponding solution extinction spectra; (iii) Discrete dipole approximation simulation of the optical properties of Au nanorods of different diameters; (iv) The dependence of the LSPR wavelength on the aspect ratio (top) and the dependence of scattering quantum yield (scattering efficiency/absorption efficiency) on the aspect ratio (bottom), adapted from (Lee, 2005).

The dielectric permittivity of the medium also affects the location of the LSPR peak frequency. Since the resonance condition of coated metal nanoparticles depends on the dielectric permittivities of both the metal and the surrounding medium, nanoparticles in the medium with a higher refractive index medium have LSPR peak extinction wavelengths that are red-shifted as compared to the LSPR peak wavelengths of nanoparticles in a lower refractive index medium (El-Sayed, 2001; Pastoriza-Santos, 2004). For example, Figure 1.4 shows the LSPR peak shift caused by coating Au

nanorods with a thin silica shell (changing the refractive index of the Au nanoparticle surrounding medium from water to silica) (Li, 2010).

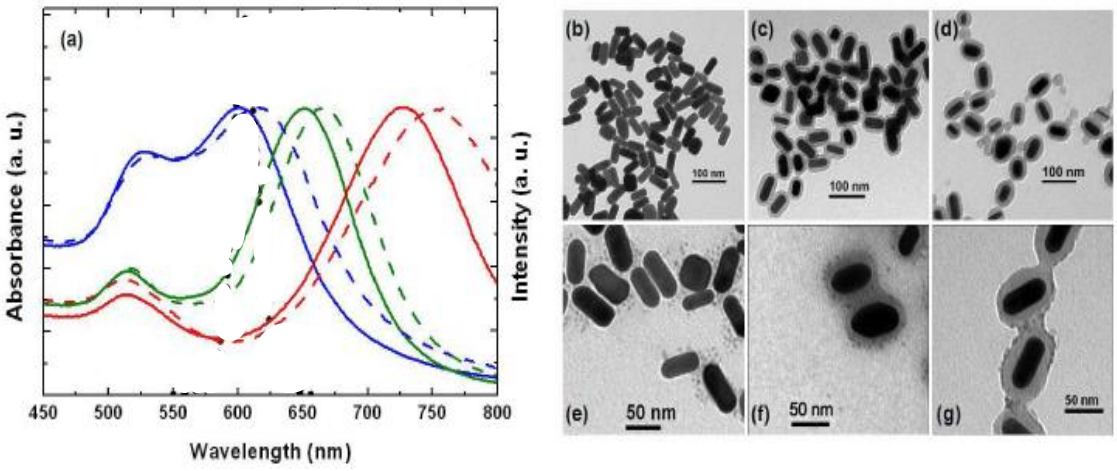


Figure 1.4 (a) UV-visible absorbance spectra of Au nanorods with LSPR peaks at 600, 650 and 730 nm are shown as solid curves. UV-visible absorbance spectra of Au nanorods coated with 13 nm-thick silica with LSPR peaks at 615 nm, 665 nm, and 750 nm are shown as dashed curves; (b)-(d) TEM images of 600 nm-resonant Au nanorods, 600 nm-resonant Au nanorods coated with 8 nm silica; (e)-(g) TEM images of 650 nm- Au nanorods, 650 nm- Au nanorods coated with 13 nm silica, adapted from (Li, 2010).

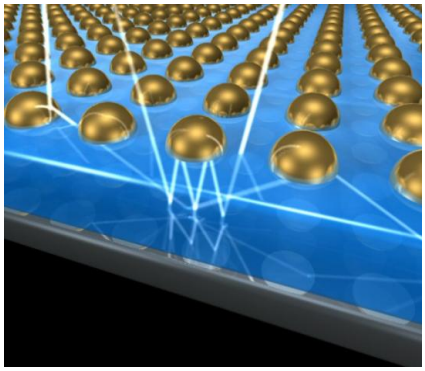
In the following sections, a review of some technological applications of noble metal nanoparticles is given. The sections are organized according to the physical properties of Au nanorods that are exploited in the application. For example, for solar cell applications, it is the light scattering properties of noble metal nanoparticle that has attracted the interest of researchers in the field (Atwater, 2010); for cancer photothermal therapy applications on the other hand, the light absorption and optical to thermal energy conversion properties of Au nanoparticles are of interest (Dreaden, 2012); for three dimensional *in-vivo* bio-imaging applications, the luminescent properties, and more specifically, the two-photon luminescence (TPL) properties of Au nanorods are of

interest (Tong, 2009); for chemical and biological sensing, the LSPR peak sensitivity to the dielectric environment is utilized for detection (Sotiriou, 2013); for amplification of optical frequency signals such as surface enhanced Raman scattering (SERS) and surface plasmon amplification by stimulated emission of radiation (SPASER), it is the highly enhanced electromagnetic fields in the near field that are utilized (Noginov, 2009).

1.2.1 Light Scattering by Au Nanoparticles

Au nanoparticles of diameters between 10 to 50 nm have scattering cross sections that are 10^5 times greater than the emission cross sections of fluorescent dyes (El-Sayed, 2001). Coupled with their small size, Au nanoparticles are very attractive for bio-imaging applications and more recently have found application as a novel way to trap light and increase solar cell efficiencies in ultra-thin solar cells (Yablonovitch, 1982; Heine, 1995; Kiess, 1995). Plasmonic photovoltaic designs usually incorporate noble metal nanoparticles on the front or back surface of a solar cell. The nanoparticles leads to preferential scattering of the incident light into the semiconductor active layer over an increased angular range, thereby enhancing the optical path length and the probability of photon absorption (Ferry, 2010). A schematic of light trapping by plasmonic nanoparticles is shown in Figure 1.5 (a) while current-voltage curves of amorphous silicon photovoltaic devices patterned with plasmonic nanostructures is shown in Figure 1.5 (b).

(a)



(b)

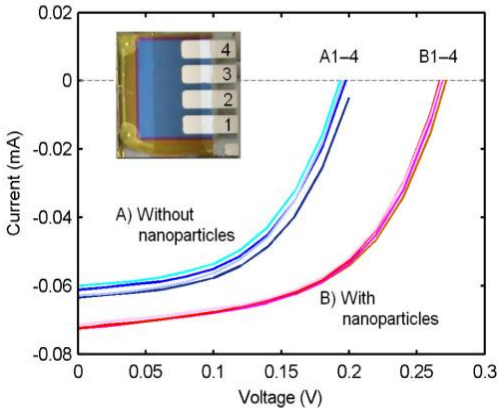


Figure 1.5 (a) A schematic illustration of light trapping by Au nanoparticles, adapted from (Atwater 2010); (b) Current characteristic of solar cells without and with gold nanoparticles. Four closely spaced curves represent four separate solar cells with and without nanoparticles, respectively (the cells are shown in the inset), adapted from (Poh, 2011).

1.2.2 Light Absorption by Au Nanoparticles

Due to their large absorption cross sections at the LSPR frequency (10^6 times greater than the absorption cross sections of fluorescent dyes), Au nanostructures can become highly localized heat sources when irradiated with a laser through the photothermal effect (Jain, 2008). This generated heat can be used in hyperthermal cancer therapy and/or to trigger drug release for chemotherapeutics. Thus, there is a possibility to realize imaging, chemotherapeutics, and hyperthermia within a single Au nanostructure platform for cancer treatments (Huang, 2007; Choi 2011). A schematic of a Au nanorod-based multifunctional theranostic system is shown in Figure 1.6 (a) while the results of Au nanorod-based plasmonic photothermal therapy study on HeLa cells (the HeLa cell line was derived from cervical cancer cells taken on February 8, 1951 from patient Henrietta Lacks) is shown in Figure 1.6 (b).

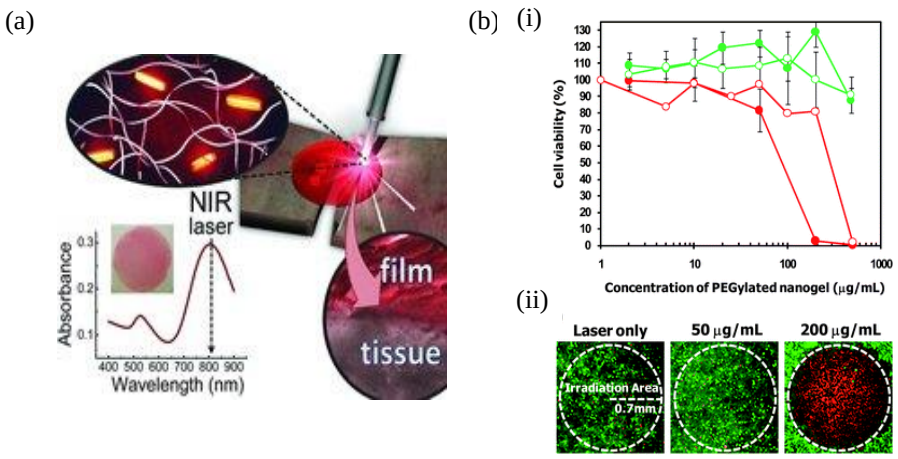


Figure 1.6 (a) A schematic illustration of Au nanorod–based photo-thermal therapy cancer treatment (Zhang, 2012); (b) (i) Viability of the HeLa cells treated with polyethyleneglycol coated Au nanoparticles at various concentrations with (red) or without (green) irradiation using an Ar^+ laser (514.5 nm) at a fluence of 26 W cm^{-2} for 5 min (7.8 kJ cm^{-2}). (ii) Fluorescence microscope images of HeLa cells treated with the Au nanoparticles at various concentrations with irradiation using Ar^+ laser. The living and dead cells emit green and red fluorescence, respectively, adapted from (Nakamura, 2010).

1.2.3 Luminescence of Au Nanoparticles

Luminescence from noble metals was first reported in 1969 by Mooradia (Mooradia, 1969) and later observed as a broad background in surface-enhanced Raman scattering (Moskovits, 1985). Single-photon luminescence from metals has been described as a three-step process: (a) excitation of electrons from the d to the sp band to generate electron–hole pairs, (b) scattering of electrons and holes on the picosecond timescale with partial energy transfer to the phonon lattice, and (c) electron–hole recombination resulting in photon emission. Two-photon luminescence (TPL) was characterized by Boyd *et.al.* (Boyd, 1986) and is considered to be produced by a similar mechanism as single-photon luminescence. The TPL signal can be amplified by several orders of magnitude when produced from roughened metal substrates. This amplification

is due to a resonant coupling with localized surface plasmons, which are well known to enhance a variety of linear and nonlinear optical properties (Chen, 1981; Sanchez, 1999; Dickson, 2000). The benefits of TPL imaging are: (i) multi-photon processes have a nonlinear dependence on excitation intensity and can be resolved in the axial direction to provide three-dimensional (3D) spatial resolution; (ii) TPL can be excited at NIR frequencies between 800 and 1300 nm, the window of greatest transmittance through biological tissue; (iii) TPL can be spectrally separated from tissue auto-fluorescence using short-pass optical filters. Figure 1.7 (a) shows TPL imaging of Au nanorods in live cells, Figure 1.7 (b) shows 3-dimensional tracking of Au nanorods (van den Broek, 2013) while Figure 1.7 (c) shows the correlation of the linear absorption spectrum of Au nanorods to their TPL excitation spectrum (Wang, 2005).

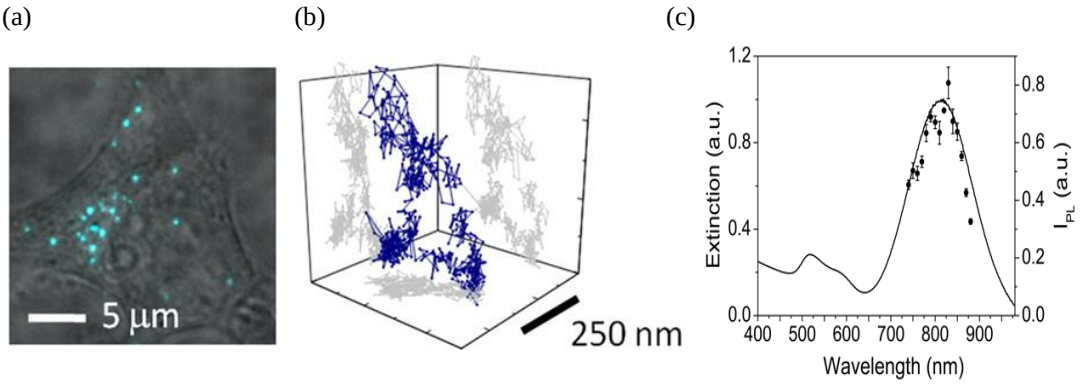


Figure 1.7 (a) The TPL image of Au nanorods (blue) in live U2OS cells superimposed on a transmission image (gray scale); (b) Typical 30 min trajectories of single Au nanorods in a live HeLa cell. Adapted from (van den Broek 2013) (c) Linear absorption of the Au nanorods (solid line) compared with the TPL excitation spectrum (solid circles with error bars). The peak at 820 nm corresponds to the longitudinal plasmon mode. The same power (0.17 mW) was used for all excitation wavelengths, adapted from (Wang, 2005).

1.2.4 Sensitivity of Au Nanoparticles to Dielectric Environment

The sensitivity of Au nanoparticles to changes in the local dielectric environment (eg. the solvent or surface bound molecules) has been applied to the detection and monitoring of biological and chemical reactions. LSPR-based assays rely on the shift of the LSPR wavelength in response to changes in the local refractive index that surrounds a plasmonic nanoparticle. For example, when a protein (n = 1.35–1.6) is adsorbed to the surface of a nanoparticle dispersed in aqueous solution (n = 1.3), a red shift of the plasmon resonance wavelength is observed (Dreaden, 2012). Several examples of LSPR-based sensing have been reported in literature (Nath, 2001; Frederix, 2003; Yonzon, 2004; Dahlin, 2005; Larsson, 2007). Notably, Engelbieme *et.al.* utilized the red shift in the LSPR wavelength of colloidal Au particles coated with a monoclonal antibody to detect the interaction of the antibody with its specific ligand (Englebienne, 1998) while Sannomiya *et.al.* detected single binding events of nanoparticle-labeled DNA strands as stepwise peak shifts in the nanoparticle LSPR frequency (Sannomiya, 2008). Figure 1.8 shows a schematic diagram of LSPR-based biosensing.

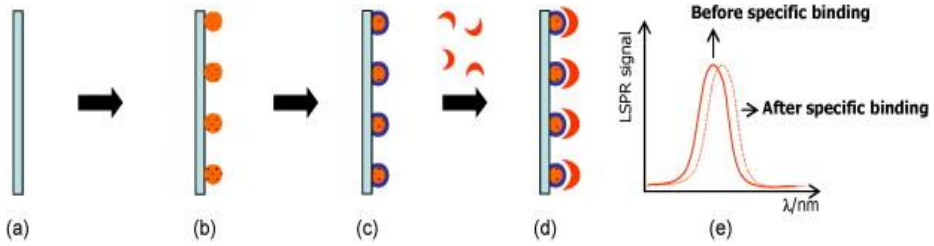


Figure 1.8 A schematic representation of the response of LSPR biosensors based on refractive index changes: (a) a substrate is chosen, (b) metal nanoparticles are attached to it by means of chemical linkers or nanolithography, (c) the metal particles are modified with the sensor moiety, (d) the analyte are attached specifically onto the recognition function on the particles, causing a change in the refractive index around the particle and an LSPR shift in (e), adapted from (Sepúlveda, 2009).

1.2.5 Light Amplification by Au Nanoparticles

At the LSPR peak wavelength, charge accumulation at the edges of the metal nanoparticle leads to a greatly enhanced optical field in the vicinity of the nanoparticle. Field intensity enhancement factors of up to 5 orders of magnitude at visible and near-infrared (Vis−NIR) frequencies translate into an increase in electronic transition probabilities of atoms or molecules exposed to these electromagnetic fields (Moskovits, 2005). Surface enhanced Raman scattering (SERS) starts with an excitation, followed by inelastic coupling to internal vibrational levels of the molecule and a subsequent radiative decay, thus involving two electronic transitions. If the frequency band of the surface plasmon field is broad enough to cover both excitation and emission, it enhances both the incident photons and the inelastically scattered, Raman-shifted photons and can thus amplify the Raman signal by up to 10 orders of magnitude (Rodríguez-Lorenzo, 2009). Since the first report dealing with SERS on Au colloids by Creighton *et.al.* (Creighton, 1979), there have been numerous demonstrations of SERS-based biological and chemical sensing (Huang, 2006; Cyrankiewicz, 2007; Rodríguez-Lorenzo, 2009). Xu *et.al.* demonstrated the detection of molecular vibrations in single hemoglobin (Hb) protein molecules attached to isolated and immobilized silver nanoparticles (Xu, 1999); Liz-Marzán *et.al.* showed that Au nanostars can be used to detect a wide variety of chemisorbing and non-chemisorbing analytes (biomarkers) at zeptomolar detection limits by sandwiching a drop-cast thin film of the analyte solution between a Au film and a subsequently drop-cast film of Au nanostars (Rodríguez-Lorenzo, 2009); Kniep *et. al.* used Au nanostructures as SERS labels for *in vivo* detection for the study of interior organelles and the composition of prokaryotic and eukaryotic micro-organisms (Kneipp,

2006) while Huang *et. al.* showed that head and neck cancer cells can be differentiated from normal cells by using sharp, highly polarized, and well-resolved Raman signals of Raman reporter molecules attached to Au nanorods on the surfaces of cancer cells (Huang, 2007; Vigderman, 2012) as shown in Figure 1.9.

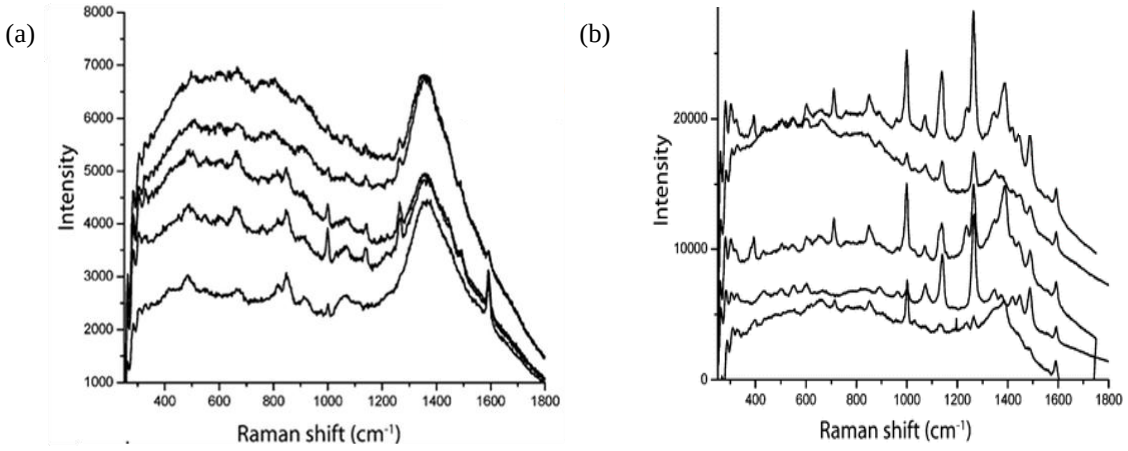


Figure 1.9 SERS detection of cancer cells using immunolabeled Au nanorods. (a) SERS spectra of normal HaCaT cells incubated with anti-EGFR antibody conjugated Au nanorods; (b) SERS spectra of HSC cancer cells incubated with anti-EGFR antibody conjugated Au nanorods. Cancer cells in (b) show stronger, sharper and better resolved SERS signals than normal cells in (a) due to the specific binding of immunolabeled Au nanorods with receptors on the cancer cell surface, suggesting that SERS may serve as a clinical diagnostic tool. The sharper and stronger Raman signals in (b) result from electromagnetic field enhancement due to interparticle coupling between immunolabeled nanorods and their alignment along the cellular membrane surface, adapted from (Huang, 2007).

When the LSPR resonant modes of a metallic nanoparticle are coupled to a strong light emitter, the resonant energy transfer can support resonant cavity modes and lead to subwavelength lasing (Noginov, 2009). Just like a conventional laser, a surface plasmon amplification by stimulated emission of radiation (spacers) is comprised of three principle components: a gain medium, a resonator and a pump. However, in contrast to

other lasers, the resonator of a spaser provides feedback for LSPR modes rather than optical modes (Gather, 2012). Figure 1.10 shows a diagram, TEM images and optical characteristics of the world's first nanolaser (Noginov, 2009).

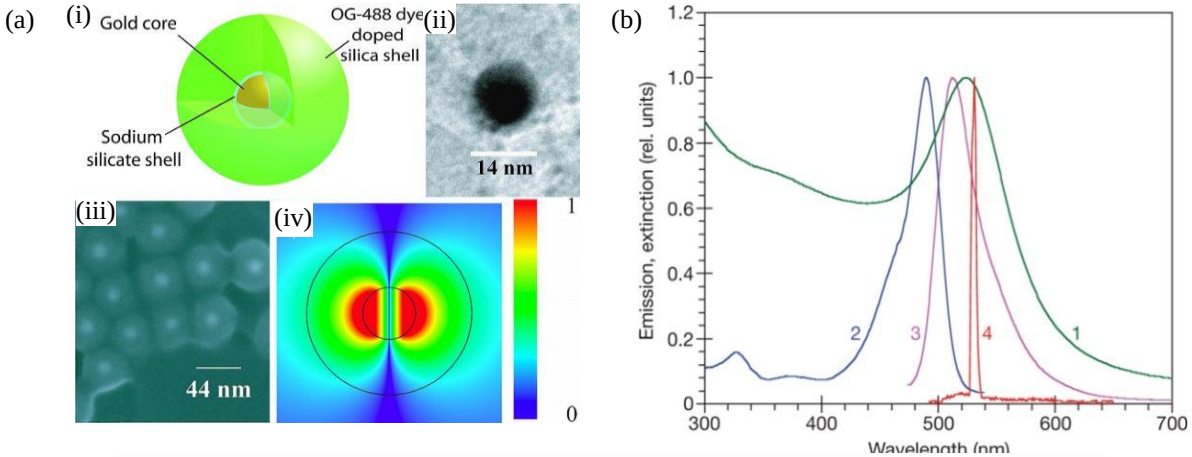


Figure 1.10 (a) (i) Diagram of the hybrid nanoparticle architecture (not to scale), indicating dye molecules throughout the silica shell. (ii) Transmission electron microscope image of Au core. (iii), Scanning electron microscope image of Au/silica/dye core–shell nanoparticles. (iv) Spaser mode (in false color), with λ=525 nm and Q = 14.8; the inner and the outer circles represent the 14 nm core and the 44 nm shell, respectively. The field strength color scheme is shown on the right; (b) Normalized extinction (1), excitation (2), spontaneous emission (3), and stimulated emission (4) spectra of Au/silica/dye nanoparticles. The peak extinction cross-section of the nanoparticles is 10^{-12} cm^2. The emission and excitation spectra were measured in a spectrofluorometer at low fluence; adapted from (Noginov, 2009).

In order to extend the technological applications of Au nanoparticles, it is often of interest to coat them with a thin layer of another material such as a polymer (Hu, 2011) or silica (Sotiriou, 2011) to form core/shell nanoparticles with enhanced colloidal or thermal stability (Pérez-Juste, 2004; Pastoriza-Santos, 2006; Chen, 2010), better biocompatibility (Gittins, 2001; Sharma, 2006) or electrically insulating properties (Qiaoqiang, 2012). Two applications that benefit from core/shell architectures studied in this work are

plasmonic light trapping (PLT) for organic photovoltaics (OPVs) and plasmonic photo-thermal therapy (PPTT) for cancer treatment.

In both applications, coating the Au nanorods with a shell of a different material is advantageous. In PLT, in order to achieve maximum light trapping, Au nanorods should be placed as close as possible to the semiconductor active layer. However, in order to incorporate light trapping Au nanorods into the active layer, a dielectric shell is necessary in order to ensure that the Au nanorods are electrically insulating otherwise serving as exciton recombination sites which degrade OPV device performance. In PPTT, an insulating shell allows faster heat dissipation, imparts higher photo-thermal stability and also provides a flexible surface for coating with secondary shells with further functionality (Sotiriou, 2013).

Besides coating, the ability to spectrally tune the peak extinction wavelength of the Au nanoparticles is key for optimizing their efficacy for specific applications. In PLT, optimal light trapping should be achieved across the entire absorption spectrum of a photovoltaic material, while optimal PPTT requires that photo-thermal sensitizers absorb light in spectral regions where tissue absorbs light poorly. For these purposes, Au nanorods have several advantages over the more commonly employed Au nanospheres. Unlike Au nanospheres, Au nanorods have two distinct LSPR bands: a transverse and a longitudinal band. The former (located from ~ 520 nm to ~ 540 nm, depending on the nanorod radius) corresponds to light absorption and scattering along the short axis of the Au nanorod. The longitudinal LSPR bands correspond to light absorption and scattering along the long axis; this band is much stronger and tunable from the visible to near infrared (NIR) region with increasing aspect ratio of the nanorod (Murphy, 2005). Au

nanorods has several advantages over Au nanospheres: (1) an LSPR extinction wavelength band consistent with the transparent window of human tissue facilitates bio-photonics applications; (2) the stronger LSPR band makes Au nanorods more sensitive to changes in their size, shape, and nano-environment as well as interparticle distance; (3) LSPR tunability can improve the efficiency of fluorescence quenching and enhancement through resonant energy transfer; (4) LSPR tunability of two-photon luminescence (TPL).

In this work, Au/SiO_2 core/shell nanospheres and nanorods were synthesized, characterized and incorporated into the active layers of OPV devices to enhance light absorption through PLT. The peak extinction wavelength of the Au/SiO_2 core/shell nanorods was designed to coincide with the wavelength region of the OPV band edge in order to ensure that light trapping was occurring at wavelengths of poor absorption. For PPTT applications, a second shell consisting of ytterbium, erbium doped yttria ($Yb:Er:Y_2O_3$) was deposited onto the Au/SiO_2 core/shell nanorods. In this case, the extinction peak of the Au/SiO_2 core/shell nanorods was designed to coincide with the emission peak of the erbium $^4F_{9/2} \rightarrow {}^4I_{15/2}$ energy transition in order to increase the spontaneous emission rate at that wavelength by taking advantage of the Purcell effect. Figure 1.11 shows schematic illustrations of PLT using spectrally tuned, active layer incorporated Au/SiO_2 core/shell nanorods and PPTT using spectrally tuned gold/silica/rare earth doped yttria core/shell nanorods.

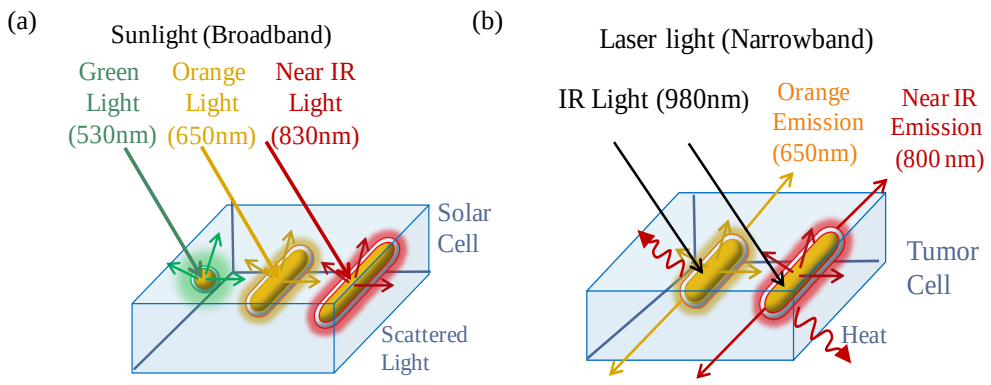


Figure 1.11 (a) A schematic illustration of light scattering by active layer incorporated, spectrally tuned Au/silica core/shell nanorods for PLT in OPVs. (b) A schematic illustration of light absorption, heat dissipation and rare earth light emission by spectrally tuned plasmonic/fluorescent Au/silica/rare earth doped yttria core/shell nanorods for cancer PPTT.

In Section 1.3, a brief literature review of OPVs is provided, the concept of PLT is introduced and some recent publications on PLT with Au and Ag nanoparticles in OPV devices are discussed. Finally, the motivation behind our approach of incorporating spectrally tailored gold/silica (Au/SiO_2) core/shell nanorods into the active layer of OPV devices is provided.

In Section 1.4, a brief literature review of PPTT is provided. Recent publications on nanoparticles that combine more than one functionality in a single nanoparticle such as plasmonic/magnetic (Sotiriou, 2013) and plasmonic/fluorescent (Jin, 2009) nanoparticles are briefly discussed and the motivation behind the approach of using spectrally tuned Au/silica/ytterbium erbium co-doped yttria ($Au/SiO_2/Yb:Er:Y_2O_3$) core/shell nanorods is introduced.

1.3 Au/SiO_2 Core/Shell Nanorods for Plasmonic Light Trapping

In this section, the physics behind solar cell operation is first introduced, followed by a historical perspective of OPVs and a literature review of plasmonic light trapping. Finally, the approach of incorporating spectrally tuned Au/silica core/shell nanorods into the active layer of OPVs is motivated and described.

Light incident upon a semiconductor material excites valence electrons localized at specific atomic lattice sites to higher energy levels where they are free to move about the lattice and conduct electricity. These excited electrons are called free or conduction electrons while the atomic lattice position that gave up the valence electron during this excitation process is called a hole. This is shown schematically in Figure 1.12. Holes are also mobile entities because valence electrons in neighboring atoms can move into these vacant orbitals in random thermal motion. Thus, current conduction in semiconductors can be thought of as occurring at two energy levels in parallel: positively charged holes conduct current in the lower (valence) energy level while free electrons conduct electricity in the higher (conduction) energy level, as shown in Figure 1.12.

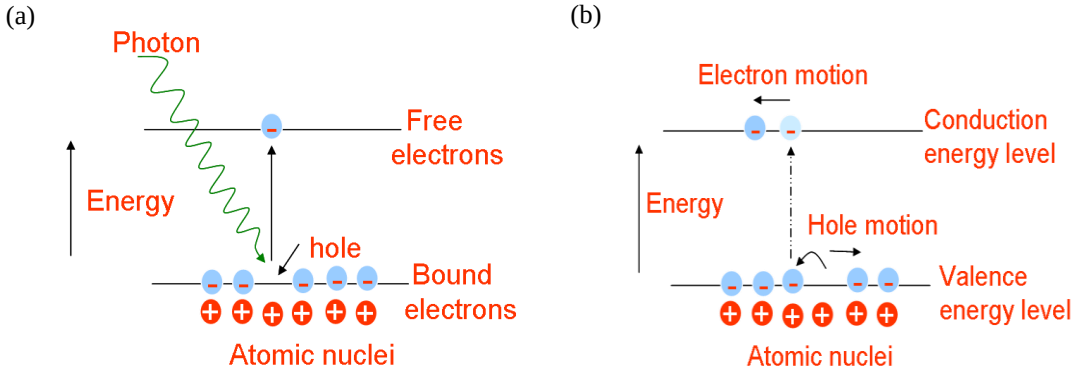


Figure 1.12 (a) Photon induced ionization through excitation of a bound (valence) electron to a higher energy state. (b) Current conduction mechanism in semiconductor materials.

The photon induced generation of these electron-hole pairs is a key mechanism in solar cell function, but not all incident photons have enough energy to ionize the semiconductor crystal and create the electron-hole pairs necessary for electric current generation. The energy required for current generation to occur is called the band gap energy. The band gap is an intrinsic property of the bulk material and arises as a consequence of the interaction between wavefunctions of atoms in the lattice. In an isolated atom, electrons are restricted to sets of discrete energy levels (orbitals) and large gaps exist in the energy scale at which no energy states are available. In a similar fashion, electrons in bulk solids are restricted to certain energy levels, but in the case of a solid, the electron has a range or band of available energies. The discrete energy levels of the isolated atom spread into bands of energies in the solid because the wave functions of electrons in neighboring atoms overlap and the electron is not necessarily localized at a particular atom (Sze, 1969). This in turn affects the potential energy term and boundary conditions in the Schrödinger equation and gives rise to shifting and splitting of energy states into energy bands as shown in Figure 1.13.

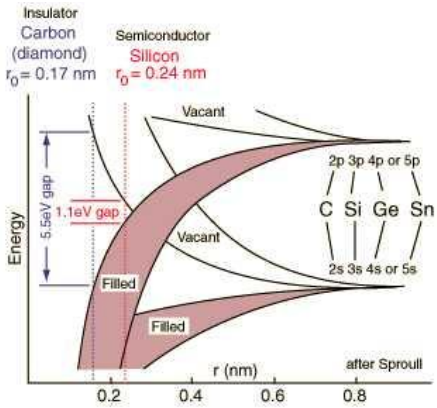


Figure 1.13 An illustration of energy levels for electrons showing evolution from discrete atomic energies to bands of allowed states separated by forbidden gaps as the atoms are brought together into a lattice (Sze, 1969).

The magnitude of the energy band gap determines the absorption spectrum of a material since photons with energies lower than the band gap are not able to excite valence electrons into the conduction band.

The absorption of a photon alone is not sufficient to generate electric power. Once an electron-hole pair is created, recombination needs to occur in a circuit outside the semiconductor crystal so that their transport results in powering electric devices. This can be encouraged by placing the semiconductor material in an electric field. In this case, electrons move toward the positive electrode and holes move toward the negative electrode. This type of device is a photoconductor since it changes its conductivity in response to light intensity but needs an external electric power source to provide the electric field. In order to create a solar cell, the electric field needs to be incorporated into the material so that the device can provide electric power when illuminated without the need for an external power source. Incorporating an electric field into a semiconductor is achievable by dissolving certain impurities or dopants into specific areas of the semiconductor, so that one part accumulates electrons and another part accumulates holes. The impurity or doping materials that are incorporated into the semiconductor are selected so that their valence state is lower than the semiconductor (in order to accumulate electrons) or higher (in order to accumulate holes) than the host material. Dopant materials with valence states lower than the host material are called p-type (because the majority carriers are positively charged) while those with valence states higher than the host semiconductor are called n-type (because the majority carriers are negatively charged). For a group IV elemental semiconductor, such as silicon, doping the

material with a group III element such as boron creates a p-type region, while doping the material with a group V element such as phosphorus creates an n-type region.

When a p-type region is brought into contact with an n-type region, electrons diffuse from the electron rich n-region across the p-n junction to the p-type region and recombine with holes. This process results in charge build up on either side of the junction and the creation of the required inherent electric field at the junction between the p and n type material. This distributed space-charge region is called the depletion region, so named because in the junction area all mobile charges are swept out by the electric field leaving behind an electrostatic gradient (potential or voltage) across the depletion region. Any electron-hole pair ionized in this region is immediately swept up by the electric field. The one-dimensional, steady state continuity equations for a p-n junction are:

$$G_n - \frac{n_p - n_{po}}{\tau_n} + \frac{1}{q}\frac{dJ_n}{dx} = 0 \tag{1.1}$$

$$G_p - \frac{p_n - p_{no}}{\tau_p} + \frac{1}{q}\frac{dJ_p}{dx} = 0 \tag{1.2}$$

where:

G_n : generation of carriers in n-region (s^{-1})

G_p : generation of carriers in p-region (s^{-1})

p_n : number density of holes in n region under illumination (cm^{-3})

p_{no} : number density of holes in n region under no illumination (cm^{-3})

n_p : number density of electrons in p region under illumination (cm^{-3})

n_{po} : number density of electrons in p region under no illumination (cm^{-3})

The current-density equations are:

$$J_n = q\mu_n n_p E + qD_n \frac{dn_p}{dx} \tag{1.3}$$

$$J_p = q\mu_p p_n E + qD_p \frac{dp_n}{dx} \tag{1.4}$$

where:

$J_n(\lambda)$: charge flux or photocurrent density in n-type region ($C \cdot cm^{-2}s^{-1}$ or $A \cdot cm^{-2}$)

$J_p(\lambda)$: charge flux or photocurrent density in p-type region ($C \cdot cm^{-2}s^{-1}$ or $A \cdot cm^{-2}$)

μ_n : minority carrier (hole) mobility in n-type region (cm^{-3})

μ_p : minority carrier (electron) mobility in p-type region (cm^{-3})

E : electric field (V/cm)

D_n : minority carrier (hole) diffusion coefficient in n-type region (cm^2/s)

D_p : minority carrier (electron) diffusion coefficient in p-type region (cm^2/s)

For an abrupt vertical p-n junction solar cell with constant doping on each side of the junction, there are no electric fields outside the depletion region and the expression for the top side (n-side) of the junction is:

$$D_p \frac{d^2 p_n}{dx^2} + \alpha F(1-R)e^{-\alpha x} - \frac{p_n - p_{no}}{\tau_p} = 0 \tag{1.5}$$

where:

α : absorption coefficient (cm^{-1})

F : number of incident photons/cm^{-2}/s^{-1} per unit bandwidth

R : fraction of incident photons reflected from surface (au)

τ_p : carrier diffusion lifetime (s)

The general solution is:

$$p_n - p_{no} = A\cosh\left(\frac{x}{L_p}\right) + B\sinh\left(\frac{x}{L_p}\right) - \frac{\alpha F(1-R)\tau_p}{\alpha^2 L_p^2 - 1} e^{-\alpha x} \tag{1.6}$$

where $L_p = \sqrt{D_p \tau_p}$ is the minority carrier (hole) diffusion length (cm).

There are two boundary conditions. At the surface of the solar cell, the surface recombination velocity provides one of the boundary conditions:

$$D_p \frac{d(p_n - p_{no})}{dx} = S_p(p_n - p_{no}) \quad \text{at} \quad x = 0 \tag{1.7}$$

At the depletion edge, the excess carrier density is negligible because the electric field in the depletion region sweeps out any excess carriers:

$$p_n - p_{no} \cong 0 \quad \text{at} \quad x = x_j \tag{1.8}$$

The hole density with these boundary conditions is:

$$p_n - p_{no} = \frac{\alpha F(1-R)\tau_p}{\left(\alpha^2 L_p^2 - 1\right)} \left\{ \frac{\left(\frac{S_p L_p}{D_p} + \alpha L_p\right)\sinh\left(x_j - \frac{x}{L_p}\right) + e^{-\alpha x_j}\left(\frac{S_p L_p}{D_p}\sinh\left(\frac{x}{L_p}\right) + \cosh\left(\frac{x}{L_p}\right)\right)}{\left(\frac{S_p L_p}{D_p}\right)\sinh\left(\frac{x_j}{L_p}\right) + \cosh\left(\frac{x_j}{L_p}\right)} e^{-\alpha x} \right\} \tag{1.9}$$

and the resulting hole photocurrent density at the depletion edge, collected from the front side of an n-on-p junction solar cell is:

$$J_p = -qD_p(dp_n/dx)_{x_j} = \frac{q\alpha F(1-R)L_p}{\left(\alpha^2 L_p^2 - 1\right)} \left\{ \frac{\left(\frac{S_p L_p}{D_p} + \alpha L_p\right) - e^{-\alpha x_j}\left(\frac{S_p L_p}{D_p}\cosh\left(\frac{x_j}{L_p}\right) + \sinh\left(\frac{x_j}{L_p}\right)\right)}{\left(\frac{S_p L_p}{D_p}\right)\sinh\left(\frac{x_j}{L_p}\right) + \cosh\left(\frac{x_j}{L_p}\right)} \alpha L_p e^{-\alpha x_j} \right. \tag{1.10}$$

The boundary conditions for the p-type base are:

$$n_p - n_{po} \cong 0 \quad at \quad x = x_j + W \tag{1.11}$$

and

$$-D_n \frac{d(n_p - n_{po})}{dx} = S_n(n_p - n_{po}) \quad \text{at} \quad x = x_{th} \tag{1.12}$$

yielding an expression for the electron distribution in a uniformly doped p-type base:

$$n_p - n_{po}$$

$$= \frac{\alpha F(1-R)\tau_n}{(\alpha^2 L_n^2 - 1)} e^{-\alpha(x_j+W)} \left\{ cosh\left(\frac{x - x_j - W}{L_n}\right) \quad -e^{-\left(\alpha(x-x_j-W)\right)} \right.$$

$$\left. - \frac{\left(\frac{S_n L_n}{D_n}\right) \cdot [cosh(x_{th}/L_n) - e^{-\alpha x_j}] \cdot \ sinh\left(\frac{x_{th}}{L_n}\right) + \alpha L_n e^{-\alpha x_{th}}}{\left(\frac{S_n L_n}{D_n}\right) sinh\left(\frac{x_{th}}{L_n}\right) + cosh\left(\frac{x_{th}}{L_n}\right)} sinh\left(\frac{x - x_j - W}{L_n}\right) \right\} \tag{1.13}$$

The photocurrent due to electrons collected at the depletion edge, $x=x_j+W$, is:

$$J_n = qD_n(dp_n/dx)_{x_j} \tag{1.14}$$
$$= \frac{q\alpha F(1-R)L_n}{(\alpha^2 L_n^2 - 1)} e^{-\alpha(x_j+W)}$$
$$\cdot \left\{ \alpha L_n - \frac{\left(\frac{S_n L_n}{D_n}\right)\left[cosh\left(\frac{x_{jth}}{L_p}\right) - e^{-\alpha x_{jth}}\right] + \left(sinh\left(\frac{x_{jth}}{L_n}\right)\right) + \alpha L_n e^{-\alpha x_{jth}}}{\left(\frac{S_n L_n}{D_n}\right) sinh\left(\frac{x_{jth}}{L_n}\right) + cosh\left(\frac{x_{jth}}{L_n}\right)} \right\}$$

Some photocurrent generation takes place within the depletion region. The electric field in this region is generally high so that photogenerated carriers are accelerated out of the depletion region before they can recombine. Hence the photocurrent per unit bandwidth is considered to be equal to the number of photons absorbed:

$$J_{dr} = qF(1-R)e^{-\alpha x}(1 - e^{-\alpha W}) \tag{1.15}$$

The total photocurrent at a given wavelength $J_{sf}(\lambda)$ that can be extracted from the incident solar flux is the sum of currents in the depletion, p- and n- regions:

$$J_{sf}(\lambda) = J_{dr}(\lambda) + J_p(\lambda) + J_n(\lambda) \tag{1.16}$$

The spectral response of a solar cell is the total photocurrent extracted by the semiconductor divided by qF(λ) (elementary charge times incident solar flux):

$$SR(\lambda) = \frac{J_{sf}(\lambda)}{qF(\lambda)} \tag{1.17}$$

There are two key parameters that determine the device spectral response: the absorption coefficient (α) and the minority carrier diffusion length ($L_p = \sqrt{D_p \tau_p}$). The absorption coefficient is a measure of the optical response of the device while the minority carrier diffusion length determines the carrier collection efficiency (electrical response). The carrier diffusion length can be thought of as a measure of the distance an ionized electron-hole pair can travel independent of each other before recombining. Materials of high quality (such as c-Si) have large minority carrier diffusion lengths (on the order of hundreds of microns) thus allowing the design of optically thick solar cells, i.e., devices that are thick enough to absorb the majority of the incident light. The carrier mobility of electrons and holes in OPVs is much smaller (in the order of 10^{-4} cm^2/Vs or less) and the active layers of these materials need to have a thickness of less than 100 nm for efficient carrier extraction (Park, 2009). Typical minority carrier diffusion lengths for Si are given in Table 1.1. A typical absorption spectrum and spectral response for a 260-micron c-Si substrate and a 2-micron a-Si solar cell are compared in Figure 1.14.

Table 1.1 Typical minority carrier diffusion lengths for c-Si, a-Si (Sze, 1969)

Parameter	Crystalline Si	Amorphous Si
n carrier diffusion length in p-type (L_n)	196 μm	132 nm
p carrier diffusion length in n-type (L_p)	68 μm	69 nm

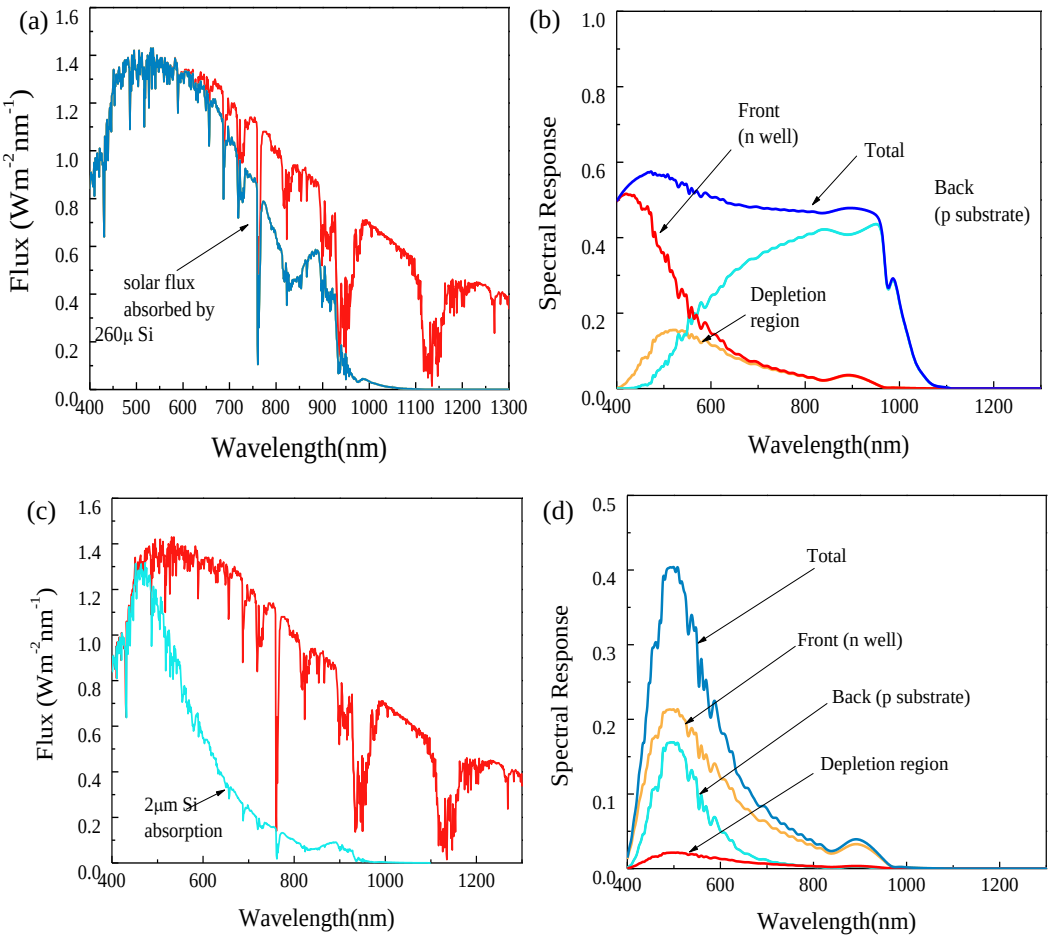


Figure 1.14 Incident solar spectrum and portion absorbed with the corresponding spectral response showing relative contribution of each area from (a-b) 260-micron crystalline silicon and (c-d) 2-micron amorphous silicon.

Inorganic semiconductors are limited by their intrinsic material properties. First, the processing of inorganic solar cells is expensive because silicon-based technology requires sophisticated clean room environment and complicated processing steps. Second, it is not possible to produce inorganic solar cells on flexible substrates with scalable manufacturing technology such as roll to roll processing. Given that its active

layer is amenable to simple solution processing, organic photovoltaic (OPV) technology is an inexpensive, flexible and lightweight option for solar energy conversion.

Early research in organic solar cells focused on the Schottky junction with low work-function metals or p-n junctions with inorganic n-type semiconductors, since most organic pigments behave as p-type semiconductors (Morel, 1978; Loutfy, 1979; Kirihata, 1981; Yokoyama, 1981; Wagner, 1982; Yokoyama, 1982; Hiramoto, 1991). Research in the area intensified after Tang *et. al.* demonstrated an organic photovoltaic device in 1986 cell with 0.95% efficiency using a blend of copper phthalocyanine and perylene tetracarboxylic (Tang, 1986). The key point of this structure is the innovative heterojunction concept which employs two organic materials (one donor material and one acceptor material) with different ionization potentials and electron affinities. The band offset at the donor/acceptor interface induces a strong electric field which can dissociate photogenerated excitons (Peumans, 2000).

Another breakthrough in photovoltaic technology came with the use of buckminsterfullerene (C_{60}). C_{60} and its derivatives such as [6,6]-phenyl-C60-butyric acid methyl ester (PCBM) are excellent n-type organic materials, capable of accepting as many as six electrons (Sariciftci, 1993). They also possess high solubility, high electron mobility, and, most importantly, the ability to achieve ultrafast charge transfer from conjugated polymers (as fast as 45 fs) (Sariciftci, 1992).

The next step forward in OPV technology was realized with the development of bulk heterojunction (BHJ) by Hiramoto *et al.* in 1992 (Hiramoto, 1992). BHJ technology addressed some of the limitations of planar cell architectures, such as the small surface area between the donor–acceptor interfaces and the requirement of long carrier lifetime to

ensure that the electrons and holes reach their respective electrodes. In the BHJ architecture, the bi-continuous network of donor/acceptor heterojunctions increases the donor/acceptor interfacial area so that charge transfer occurs rapidly. Seminal BHJ OPV papers using poly(2-methoxy-5(20-ethylhexyloxy)-1,4-phenylenevinylene (MEH-PPV) as the donor molecule and PCBM as the acceptor molecule were reported by the Heeger (Yu, 1995) and Friend (Marks, 1994) groups, independently (Figure 1.15).

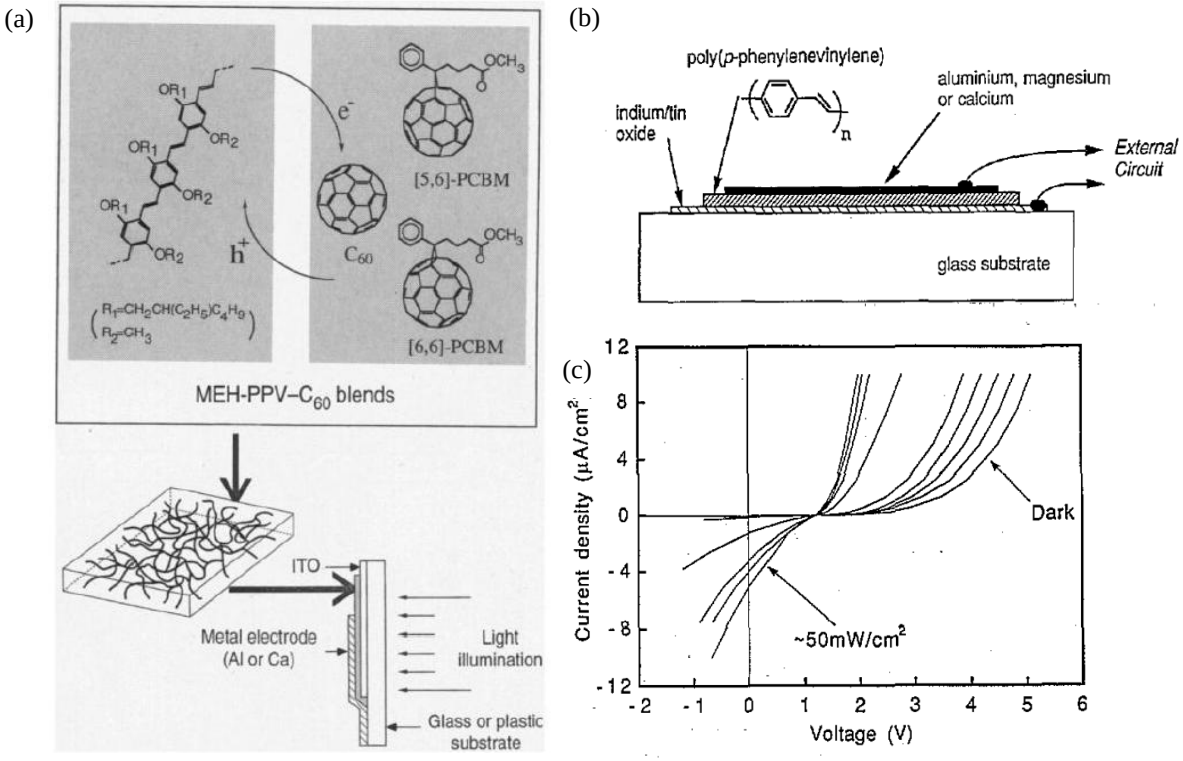


Figure 1.15 (a) Polymer/fullerene BHJ OPVs by Heeger group, adapted from (Yu 1995) (b) polymer/polymer BHJ OPVs by Friend group, and (c) Device response of MEH-PPV-CN-PPV BHJ OPV, adapted from (Marks, 1994).

Further studies revealed that the nanoscale morphology of the active layer plays an essential role and many strategies have been explored for morphology optimization (Goetzberger, 2003). Solvent selection (Duong, 2012), thermal annealing (Ma, 2005) or

incorporation of various additives (Li, 2011) have led to improved active layer morphologies and further improvements in photon conversion efficiency (PCEs) (Brady, 2011). Novel polymer blends such as poly(3-hexylthiphene) (P3HT) (Padinger, 2003), with its high hole mobility or low-bandgap polymers such as poly[2,6-4,8-di(5-ethylhexylthienyl)benzo[1,2-b;3,4-b]dithiophene-alt-5-dibutyloctyl-3,6-bis(5-bromothiophen-2-yl) pyrrolo[3,4-c]pyrrole-1,4-dione] (PBDTT) whose absorption extends up to $\lambda \sim 900$ nm have also led to improvements. Currently, a PCE of over 9% for single-junction OPVs has been achieved by Mitsubishi Chemical (Service, 2011) and an NREL-certified PCE of 10.6% has been obtained for tandem cells by Li *et. al*. (Li, 2012). Despite impressive progress, further improvements are needed for this technology to compete with Si-based solar energy.

The energy conversion efficiency of an OPV device is determined by the nature of charge photo-generation and transport in the constituent organic materials. Photons absorbed by molecules lead to current generation only if they are generated near donor–acceptor interfaces such that dissociation occurs prior to dissipative recombination (Li, 2012). However, since the carrier mobility of electrons and holes is often small in photo-active polymers (on the order of 10^{-4} cm^2/Vs, or less), it is common to use rather thin films in order to compromise between optical absorption and carrier collection. In solar cells using recently developed organic bulk heterojunctions, the active layer is in the range of 100nm or less for efficient carrier extraction (Park, 2009). The use of such thin layers means many photons remain unharvested and there are significant research activities focused on developing better light trapping designs to enhance photon absorption. From a ray-optics perspective, conventional light trapping employs total

internal reflection by patterning the entrance interface and randomizing the light propagation direction inside the active material. This leads to a longer interaction distance between the photon and the material and hence an absorption enhancement (Deckman, 1983). In thick crystalline Si solar cells, light trapping is typically achieved with the use of patterned structures that have features on the scale of the wavelength of light. The active layers in organic cells, however, have thicknesses that are far smaller than the wavelength of light and hence the relative large-scale geometries used in traditional light trapping designs are not suitable for thin-film cells (Atwater, 2010). Hence, for OPV applications, it is of interest to develop light trapping techniques that rely on structures that are compatible with the scale of OPV films, i.e. less than 100nm (Qiaoqiang, 2012). One light trapping method that is suitable for OPV applications and has garnered attention recently involves the use of Au nanoparticles due to their strong light scattering and absorption properties at optical frequencies, further detailed in Section 2.1 .

Plasmonic light trapping for OPVs has been demonstrated by various groups. For instance, by incorporating Au nanospheres (~ 45 nm) into the PEDOT:PSS buffer layer of an P3HT:PC_{60}BM OPV device, Morfa *et. al.* increased the PCE from 1.3% to 2.2% (Morfa, 2008). Au nanoparticles (15 nm) introduced in the PEDOT:PSS layer of an OPV device using poly(2-methoxy-5(20-ethylhexyloxy)-1,4-phenylenevinylene (MEH-PPV) as the active layer led to an enhancement in PCE from 1.99% to 2.36% (Qiao, 2011). Wu *et. al.* demonstrated that incorporating 45 nm Au nanoparticles into the anodic buffer layer of a P3HT:PCBM OPV device improved the PCE to 4.24% from a value of 3.57% for the device fabricated without Au nanoparticles (Wu, 2011). More recently, Au

nanoparticles (72 nm) were deposited in the interconnecting layer of an inverted tandem polymer solar cell consisting of a cell based on poly[(4,4'-bis(2-ethylhexyl)dithieno[3,2-b:2',3'-d]silole)-2,6-diyl-alt-(2,1,3-benzothiadiazole)-4,7-diyl]: [6,6]-phenyl-C_{60}-butyric acidmethyl ester (PSBTBT: $PC_{60}BM$) cell, and resulted in a 20% increase in PCE from 5.22% to 6.24% (Yang, 2011). The results of these studies are summarized in Table 1.2.

Table 1.2 Summary of Plasmonic Light Trapping in OPV devices

Au Nanosphere Size	OPV Polymer	Reference Cell PCE	Plasmonic Cell PCE	Reference
45 nm	P3HT:$PC_{60}BM$	1.3%	2.2%	(Morfa, 2008)
15 nm	MEH-PPV	1.99%	2.36%	(Qiao, 2011)
45 nm	P3HT:PCBM	3.57%	4.24%	(Wu, 2011)
72 nm	PSBTBT: $PC_{60}BM$	5.22%	6.24%	(Yang, 2011)

P3HT:$PC_{60}BM$ = poly(3-hexylthiphene): [6,6]-phenyl-C60-butyric acidmethyl ester
MEH-PPV = poly(2-methoxy-5(20-ethylhexyloxy)-1,4-phenylenevinylene
PSBTBT:$PC_{60}BM$ = poly[(4,4'-bis(2-ethylhexyl)dithieno[3,2-b:2',3'-d]silole)-2,6-diyl-alt-(2,1,3-benzothiadiazole)-4,7-diyl]:[6,6]-phenyl-C60-butyric acidmethyl ester

In all of these reports, nanoparticles are located relatively far from the active organic layers and the absorption enhancement arises from light scattering from nanoparticles rather than near-field enhanced LSPR modes. Embedding metallic nanoparticles into the active layers of OPVs can make full use of the enhanced LSPR near field (Qiaoqiang, 2012).

Currently, there are only a few reports documenting incorporation of plasmonic materials into OPV active layers. Szeremeta *et. al.* showed that Cu nanoparticles (20 nm) embedded inside P3HT layers enhanced the dissociation of excitons without increasing the P3HT optical absorption (Szeremeta, 2011). Wang *et. al.* demonstrated improved PCEs in three different polymer systems resulting from incorporation of Au nanoparticles

in the active layer but the observed external quantum efficiency (EQE) enhancements were broadband, indicating that the enhancements were due to light scattering and not due to the narrow band LSPR near field (Wang, 2011). Mei *et. al*. incorporated 20nm dodecanethiol-functionalized Ag nanoparticles into the active layer of a P3HT:$PC_{60}BM$ OPV device and found that while their addition into the active layer significantly enhanced carrier mobility, it decreased the total extracted carrier density as shown in Figure 1.16 (Mei, 2011).

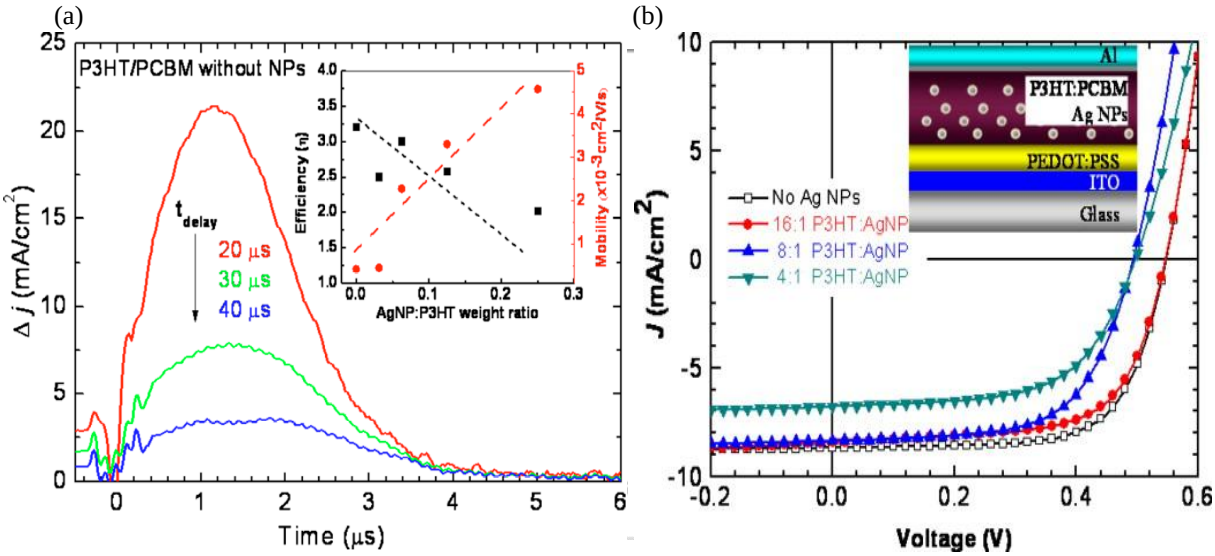


Figure 1.16 (a) Photo-charge extraction by linearly induced voltage (PCELIV) current transients, collected at different values of t_{delay} for a P3HT:PCBM BHJ solar cell with and without Ag nanoparticles. The inset shows the solar cell device efficiency and the charge-carrier mobility for hybrid cells with different concentrations of Ag nanoparticles. The mobility strongly increases with increasing concentration of Ag nanoparticles. (b) Current voltage curves of reference and plasmonic solar cells with various ratios of P3HT:Ag nanoparticles, adapted from (Mei, 2011).

They hypothesized that carriers leave the organic phase and move to an aggregated subnetwork of Ag nanoparticles. The decreased carrier extraction was

attributed to the fact that Ag nanoparticles act as carrier traps, leading to significantly enhanced recombination and thus lower overall net efficiency. In order to circumvent this issue, coating noble metal nanoparticles with a thin insulating layer would render their surfaces insulating yet still retain their attractive optical properties.

Several synthesis protocols have been reported to coat Au and Ag nanoparticles with insulating shells. For example, Wang *et.al.* developed a procedure to coat Au nanoparticles with ZrO_2 (Wang, 2011), while Klopfer *et. al.* used atomic layer deposited Al_2O_3 to coat a monolayer of Au nanoparticles for SERS applications, and demonstrated that the ultrathin coating keeps the nanoparticles from agglomerating, separates them from direct contact with the probed material and allows the nanoparticles to conform to different contours of substrates (Klopfer, 2011). A silica coating is very well suited for the purpose of incorporating Au nanoparticles into the active layer of OPVs because silica provides a colloidally stable and versatile surface that organic ligands like octadecyltrimethoxyosilane (OTMS) can be attached to a silica surface through silane chemistry (Pastoriza-Santos, 2006). Another important consideration in optimizing OPV device performance is to take into account the absorption frequency range of the polymer and design the light trapping nanoparticles to resonantly scatter light across the entire OPV polymer absorption frequency range but especially near the polymer band edge. This is because at the band edge, the polymer absorbs light very poorly and it is in this region that the OPV device can benefit the most from the incorporation of light trapping schemes. Shown in Figure 1.17 is a solar spectrum along with the maximum wavelengths of absorption of 3 common polymer systems.

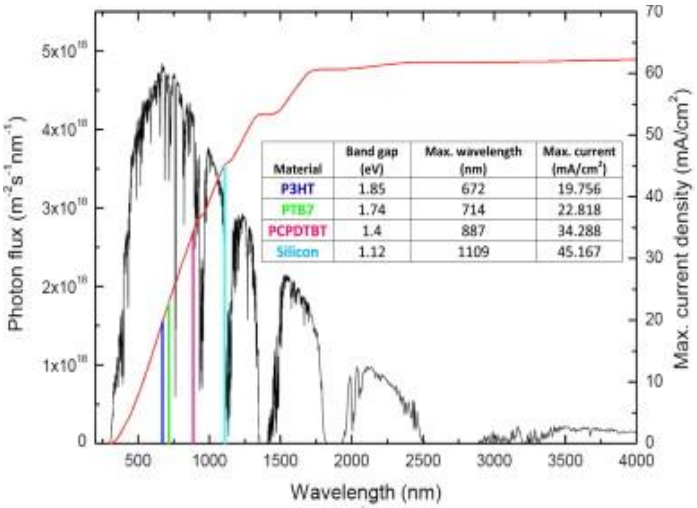


Figure 1.17 Maximum attainable values of current density (red) for Si, P3HT, PTB7 and PCPDTBT with an AM 1.5G photon flux (black). The inset summarizes the band gap, maximum wavelength of absorption and maximum attainable photocurrent density for these materials. Adapted from (Chen, 2013)

Since noble metal nanospheres have fairly narrow extinction wavelength bands centered at ~ 530 nm (Catchpole, 2008), they have limited utility for light trapping in OPCs since most OPV systems absorb light fairly efficiently in this wavelength regime. In Au nanorods, on the other hand, free electrons oscillate along both the long and short axes of the rod, resulting in two resonance bands: a band at ~ 530 nm resulting from electron oscillations along the short axis and a stronger band of wavelengths resulting from electron oscillations along the long axis. The peak longitudinal resonance wavelength of Au nanorods can be controlled between ~ 570 nm to ~ 930 nm by varying the nanorod aspect ratio (AR) (Huang, 2007). Nanorods can thus be designed to spectrally match the band edge of most OPV polymer systems, a spectral region where OPV polymers have poor light absorption. Shown in Figure 1.18 (a) is a schematic of an Au nanosphere and an Au nanorod of AR ~ 4 inside the active layer of an OPV material

demonstrating light scattering of wavelengths resonant with the nanoparticle. In Figure 1.18 (b), the extinction spectra of Au nanospheres and Au nanorods of AR ~ 4 are shown along with the EQE spectrum of PBDTT-DPP:$PC_{60}BM$ polymer.

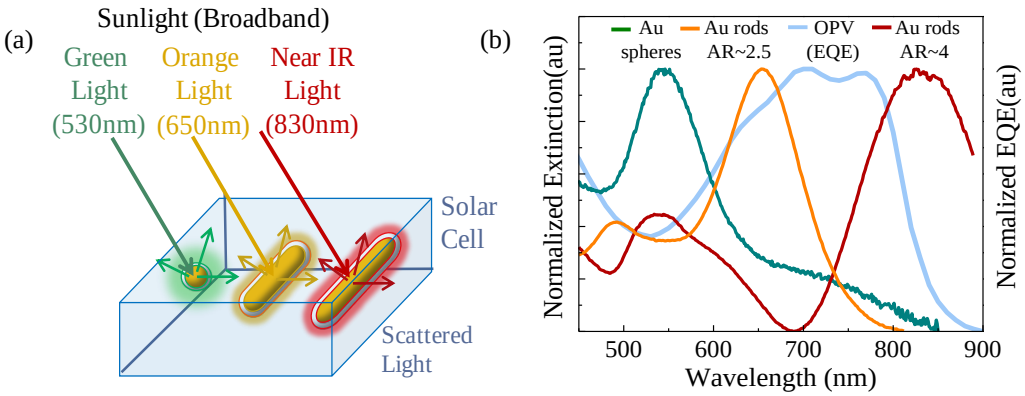


Figure 1.18 (a) Schematic illustration of light scattering by spectrally-tuned gold/silica core/shell nanospheres and nanorods (b) EQE of an OPV polymer and extinction spectra of Au nanospheres and nanorods of AR ~ 4 showing spectral overlap between OPV polymer and Au nanoparticles

In this work, poly(3-hexylthiophene):[6,6]-phenyl-C_{60}-butyric acid methyl ester (P3HT:$PCB_{60}M$) with a band edge of ~ 670 nm and poly[2,6-4,8-di(5-ethylhexylthienyl)benzo[1,2-b;3,4-b]dithiophene-alt-5-dibutyloctyl-3,6-bis(5-bromothiophen-2-yl) pyrrolo[3,4-c]pyrrole-1,4-dione]:[6,6]-phenyl-C_{60}-butyric acid methyl ester (PBDTT-DPP:$PC_{60}BM$) with a band edge of ~ 830 nm were chosen for the OPV device in order to demonstrate the versatility of Au/SiO_2 nanorods for spectrally tuned plasmonic light trapping.

1.4 Au/SiO_2/Yb:Er:Y_2O_3 Core/Shell Nanorods for Plasmonic Photothermal Therapy

Photo-thermal therapy (PTT) is a cancer treatment technique in which hyperthermia (a tissue temperature of > 43^{o}C for > 10 minutes) is induced in the diseased tissue by irradiation with light (usually laser light). In PTT, a photosensitive material is injected in the diseased tissue and subsequently exposed to laser light of frequency that is resonant with the peak absorption frequency of the photosensitizer. The treatment relies on creating a difference in thermal relaxation times of the target tissue compared to healthy surrounding tissue (tissue without embedded sensitizer material). This quantity is dependent on the excitation wavelength and is modulated by various factors: the optical absorption, the thermal conductivity, the specific heat and the density of both the medium and the photosensitizer (Dreaden, 2012). Exogenous dyes such as naphthalocyanines and metal porphyrins have been commonly used as photosensitizers but they suffer photo-bleaching under laser irradiation, which is a serious drawback (Dougherty, 1987). Au nanoparticles have recently emerged as superior photo-sensitizers because they have high light-to-heat conversion rates, and superb photo-stability. Plasmonic photothermal therapy (PPTT) using Au nanoparticles was first demonstrated *in vitro* by Pitsillides *et. al.* (Pitsillides, 2003). In their work, spherical Au nanoparticles were conjugated to IgG antibodies which targeted CD8 receptors on peripheral blood lymphocyte cells. Using nanosecond pulsed visible laser exposure, 95% of cells containing as few as 500 nanoparticles cell were rendered non-functional (versus 5–8% in sham treatments) due to membrane disruption. Breast carcinoma cells specifically labeled with polyethylene glycol (PEG)-coated Au/SiO_2 core/shell nanospheres were efficiently destroyed by continuous wave near infra-red (NIR) laser exposure (7 min, 35 W cm^{-2}, 810nm laser

frequency, 5 mm laser spot diameter). The SiO_2 core, PEGylated Au shell nanostructures were later injected into the tumor interstitium of mice bearing sarcoma xenografts. Using magnetic resonance imaging (MRI), NIR laser exposure was directed at the tumor site (4 W cm^{-2}, 5 mm spot diameter, <6 min) and based on the temperature-dependent MRI frequency shift of protons in the tissues, intra-tumoral temperature changes were three dimensionally mapped in real time and showed an average temperature increase of 37.4 ± 6.6 °C in Au nanoshell-based PPTT. NIR PPTT using systemically administered SiO_2/Au nanoshells was later demonstrated using a colon cancer model. PEGylated Au nanoshells were intravenously injected in carcinoma-bearing nude mice and their tumors were exposed to NIR laser radiation after 6 h accumulation (4 W/cm^2, 3 min, 5.5 mm spot dia). Tumors in SiO_2/Au nanoshell- treated mice were completely ablated after a single PPTT treatment and the animals appeared healthy and tumor free >90 days post treatment. In contrast, tumors in control and sham-treated animal groups continued to grow, with nearly 50% mortality at day 10 (Huang, 2011).

Compared with Au nanospheres and SiO_2/Au nanoshells, Au nanorods have an advantage in that their peak absorption wavelength can be designed to fall within the range of wavelengths where tissue absorbs poorly and light has its maximum depth of penetration in tissue (Huang, 2007). Unfortunately, the critical micelle concentration of the surfactant used to prepare Au nanorods, CTAB, is much higher (~ 1 mM) than the reported threshold for cytotoxicity (~ 0.2 μM), raising issues of maintaining stable nanorod dispersions without causing collateral injury to healthy cells or tissues (Cortesi, 1996; Huff, 2007). Furthermore, the introduction of improperly passivated Au nanorods into the body results in their rapid clearance by the reticuloendothelial system

(Tong, 2009). The complete removal of CTAB, followed by a robust method of surface modification is required to produce stable Au nanorod suspensions with long circulation lifetimes and specific targeting to diseased cells. At least three methods have been reported to reduce the amount of CTAB to below cytotoxic levels without severely compromising dispersion stability:

One involves simple surfactant exchange: CTAB can be partitioned into chloroform and gradually exchanged with phosphatidylcholine (PC), resulting in markedly lower cytotoxicity toward HeLa cells (Tong, 2009).

Another approach involves the displacement of CTAB by sterically stabilizing surfactants, particularly nonionic polymers such as PEG chains terminating in chemisorptive groups such as thiols or dithiocarbamates (DTC) (Niidome, 2006; Huang, 2007). Several polyelectrolytes have been examined for their effects on cell uptake and toxicity (Hauck, 2008). For detoxification of Au nanorods on a larger scale, it has been shown that polystyrenesulfonate (PSS) can serve as a mild detergent and enable the removal of CTAB by ultrafiltration and surfactant exchange, to the extent that no significant toxicity is observed at NR concentrations as high as 85 μg/ml (Tong, 2009).

A third approach involves replacing the CTAB with an SiO_2 shell. This approach reduces Au nanorod colloidal solution cytotoxicity, while simultaneously imparting thermal stability under laser illumination (Chen, 2010). This is particularly important for imaging and therapeutic modes that involve laser irradiation at high intensity or over extended periods, such as photoacoustic tomography, photothermal therapy, multiphoton microscopy, and optically modulated drug release (Dickerson, 2012). When irradiated with high-intensity femtosecond or nanosecond lasers matching their plasmon resonance

bands, Au nanorods not only melt and change shape to spherical nanoparticles, but also fragment over certain energy thresholds (Link, 1999). This poor photothermal stability is undesirable because the reshaped Au nanorods have significantly reduced absorbance. Chen *et. al.* were the first to show that replacing the CTAB coating layer with a silica shell provided the Au nanorods with the mechanical stability necessary to preclude deformation while minimizing photon absorption and scattering within itself (Chen, 2010). When subjected to exposures of 21.2mJ/cm^2, their TEM studies revealed that a significant fraction of the bare Au nanorods had deformed into rounder, lower aspect ratio entities, while Au/SiO_2 core/shell nanorods did not exhibit such behavior at these levels of irradiation, maintaining their original morphology and absorption spectra as shown in Figure 1.19.

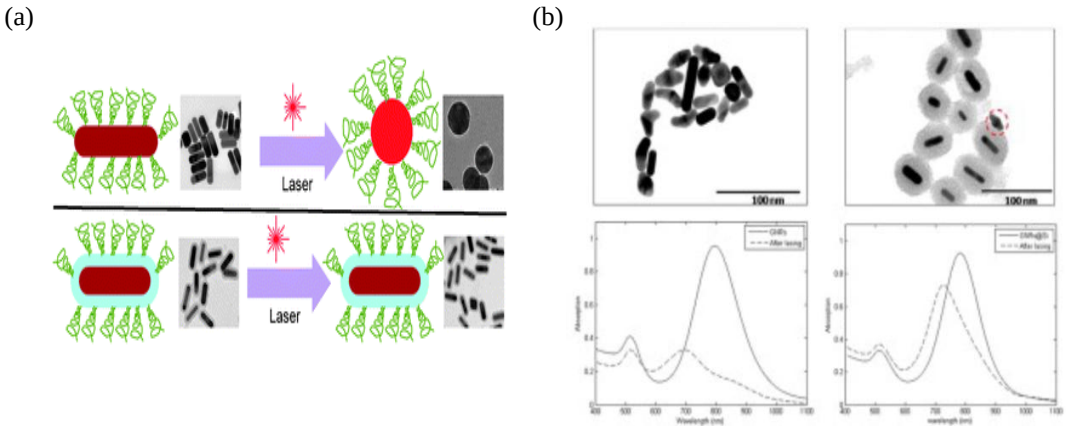


Figure 1.19 (a) An illustration and corresponding TEM images of the effect of laser irradiation on Au nanorods (top) and Au/silica core/shell nanorods (bottom) Adapted from (Hu 2011) (b) TEM images bare Au nanorods and Au/SiO_2 core/shell nanorods along with optical absorption spectra for bare Au nanorods and Au/SiO_2 core/shell nanorods before and after exposure with 21.20 mJ/cm^2 of 785 nm laser irradiation (Chen, 2010).

While significant challenges remain, several groups have demonstrated *in-vivo* tumor therapy using Au nanorods, shown in Table 1.3. Recently, nanoparticles that combine plasmonic properties with other functionalities such as magnetism or fluorescence have been realized and have demonstrated some novel features and advantageous properties compared to single function nanoparticles (Timothy 2007; Sortino, 2012). For example, hybrid plasmonic/magnetic nanomaterials can be guided to the diseased tissue by an externally applied magnetic field and once in place, optically activated (Sotiriou, 2011), while plasmonic/fluorescent hybrid nanomaterials have potential application for simultaneous diagnosis and therapy (Nabika, 2003; Lakowicz, 2005; Matsuura, 2005; Song, 2005; Liu, 2006; Mertens, 2006; Schneider, 2006; Rai, 2008; Wu, 2011). For example, Jin et. al. synthesized Au/quantum dot(QD) hybrid nanorods and observed plasmon-enhanced luminescence from the QD emitters as a function of distance between the Au and the QD (Jin 2009). A factor impeding the biomedical application of quantum dots is the fact that they contain toxic elements (e.g., cadmium, selenium, and lead) and the light emission is not temporally continuous (termed blinking) (Sharma 2006). Using high-energy excitation photons always has serious drawbacks: significant autofluorescence from biological samples resulting in low signal-to-background ratio and considerable absorption and scattering effects for visible light, inducing short penetration depth in biological tissues. Near-infrared (NIR) light on the other hand allows deeper penetration depth for *in vivo* bioimaging and can efficiently suppress autofluorescence and light scattering.

Table 1.3 Summary of Au nanorod-based photo-thermal therapy results

Animal model: cancer type	Nanorod diameter (d) & length(l) (nm)	Nanorod Resonant Wavelength (nm)	Laser power ($W\ cm^{-2}$)	PhotoTherapy Results
Mice: SCC	d =10±2 l = 35±5	750	4.15	20% of the injected dose accumulated in the tumor. Complete resorption of the tumor was achieved (Choi, 2011).
Mice: squamous cell tumor	d = 13±2 l = 50±5	810	1.7	Resorption of >57% of tumors treated with direct injection of nanoparticles to the tumor site *versus* 25% of the intravenously-treated tumors (Dickerson, 2008)
Mice: MDA-MB-435 human tumors	d = 11±3 l = 47±5	800	2	Circulation time = 17 hour. 7% of the injected dose in the tumor site. Temperature at the tumor tissue reached 70 °C. Single intravenous. injection of Au nanorods coupled with laser irradiation eliminated all the induced tumor in mice (von Maltzahn, 2009)

Upconverting (UC) nanoparticles have recently shown promise as imaging probes due to their ability to convert low-energy near-infrared (NIR) radiation into higher-energy visible luminescence (Heer, 2004). Unlike Stokes-shifted luminescence from organic fluorophores (Weiss, 1999), or semiconductor quantum dots (Alivisatos, 2005), this anti-Stokes luminescence circumvents competition from auto-fluorescent background signals in biological systems. The NIR-to-visible upconversion is based on sequential energy transfers between lanthanide dopants or excited-state absorption involving their real metastable-excited states with lifetimes as long as several milliseconds, a process orders of magnitude more efficient than the 2-photon absorption process typically used in multiphoton microscopy (Auzel, 2003). This permits the use of a continuous wave (CW)

laser to generate the upconverted luminescence, resulting in virtually zero 2-photon photoluminescence background from biomolecules, since powerful pulsed-laser excitation is generally required for generating measurable multiphoton absorption. The use of NIR excitation also minimizes the possible photo-damage in biological systems and permits deeper tissue penetration in whole-animal imaging. Figure 1.20 (a) shows a schematic illustration of a UC process involving Yb^{3+} and Er^{3+}. In the upconversion process, 980nm light is absorbed by the Yb^{3+} ion and the energy is transferred to the Er^{3+} ion. Upon relaxation from the higher energy manifolds, visible light emission occurs. Figure 1.20 (b) shows an example of the use of Yb:Er:$NaYF_4$ nanoparticles for live cell bioimaging.

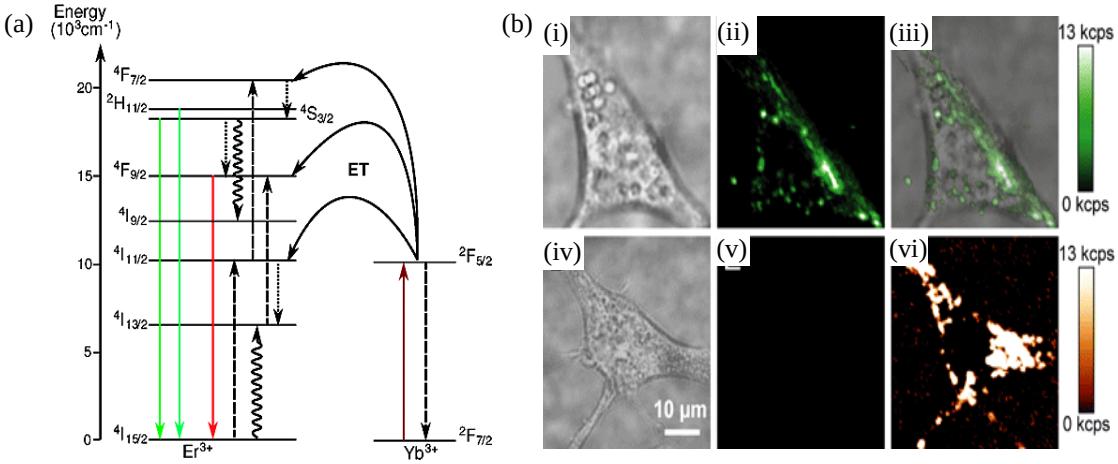


Figure 1.20 (a) Energy scheme with the relevant processes of energy transfer UC in Yb^{3+}/Er^{3+} codoped materials: energy transfers, radiative, multiphonon processes, and cross-relaxation are depicted in dashed, full, dotted, and curly lines, respectively. The high efficiency in the upconverter is achieved by the absorption of the photons by the Yb^{3+} ions followed by the transfer of the excitation to the Er^{3+}(Schietinger 2009) (b) Live-cell imaging of Yb:Er:$NaYF_4$ in NIH 3T3 murine fibroblasts. (i) Brightfield image of a cell with endocytosed Yb:Er:$NaYF_4$, (ii) upconverted luminescence following 980-nm excitation, and (iii) overlay of (i) and (ii). (iv) Brightfield image of a cell without Yb:Er:$NaYF_4$, (v) upconverted luminescence following 980-nm excitation, and (vi) cellular autofluorescence following 532-nm excitation. All images are shown on the same intensity scale (Scale bar, 10 µm), adapted from (Wu, 2009)

Photoluminescent (PL) probes for deep tissue *in vivo* imaging should have PL emission in the spectral range favorable for penetration of light through thick tissues due to minimal light scattering and tissue autofluorescence (Chen, 2012). The 800 nm energy transition of Tm^{3+} ($^3H_4 \rightarrow {}^3H_6$) is especially well suited for biological applications because it falls in a wavelength region where tissue absorbs light poorly. Figure 1.21(a) shows a schematic illustration of a UC process involving Yb^{3+} and Tm^{3+}, while Figure 1.21(b) shows an example of bioimaging using energy transitions of Tm^{3+} (Zhou, 2011).

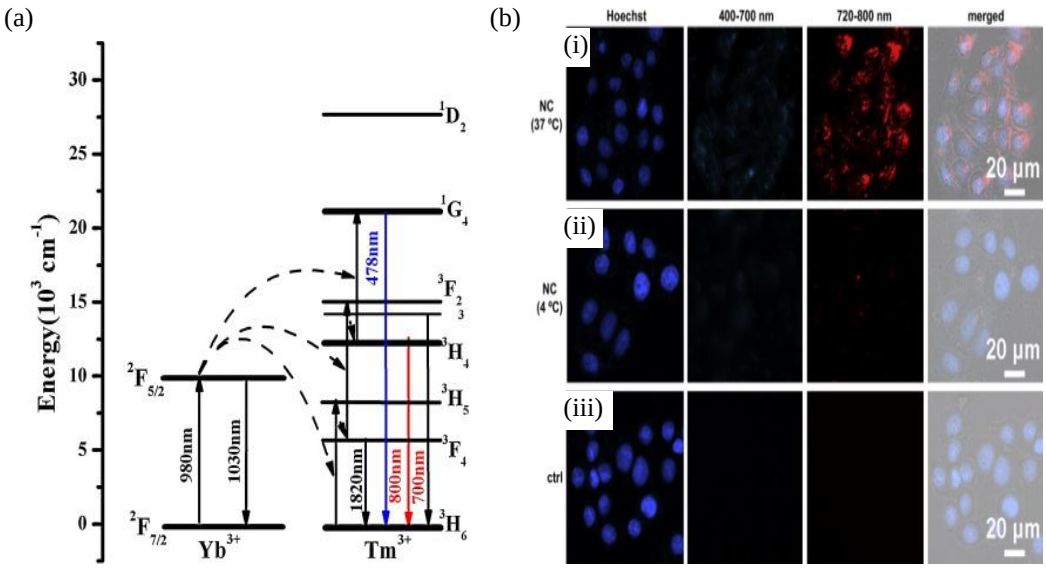


Figure 1.21 (a) An illustration of energy transitions involved in upconversion using Yb^{3+} as a sensitizer and Tm^{3+} as the emitter (Zhang, 2010). (b) *In-vitro* bioimaging of photosensitizer: colloidal NCs in HeLa cells. HeLa cells were incubated with (at 37 °C (i) or at 4 °C (ii)) and without (ii) Yb:Tm:$NaYF_4$ NCs. All the concentration of photo-sensitizer colloidal NCs was 10 μgmL^{-1} and the incubation time was 3 h. The four panels from left to right in each line (a–c) are the false-colored fluorescent images of Hoechst 33258, visible (400 − 700 nm) and NIR (720 − 880 nm) UC emission of Yb:Tm:$NaYF_4$ NCs, and the merged images, respectively, adapted from (Zhou, 2011).

However, as nonlinear optical materials, UC nanocrystals usually need high excitation power densities, which might damage biological tissues in applications (Liu,

2011). Therefore, the desired UC nanocrystals for such applications should be of low pumping threshold in power density and show high efficiency for UC emissions. The higher local field intensity caused by the plasmon resonance positively influences the UC efficiency because of the non-linear nature of upconversion (Paudel, 2011; Fischer, 2012). Klopfer *et. al.* enhanced UC emissions of Yb:Er:$NaYF_4$ nanocrystals by factors of about 2.3 and 3.7 for green and red UC emissions of Er^{3+} ions, respectively by combining them with Ag nanoparticles (Klopfer, 2011). Schietinger *et. al.* demonstrated plasmon-enhanced UC emissions in single Yb:Er:$NaYF_4$ co-doped nanocrystals and their overall emission intensity was increased by a factor of 3.8 (Schietinger, 2009). Zhang *et. al.* synthesized silver/silica/erbium-doped yttria core/shell nanospheres (Zhang, 2010). They demonstrated that plasmonic enhancement of two prominent emission bands of Er^{3+} ions centered at 535nm ($^4S_{3/2} \rightarrow {}^4I_{15/2}$) and 645nm ($^4F_{9/2} \rightarrow {}^4I_{15/2}$) was a function of distance between the fluorescent (Er^{3+}) and the plasmonic (Ag) component of the hybrid nanosphere as shown in Figure 1.22.

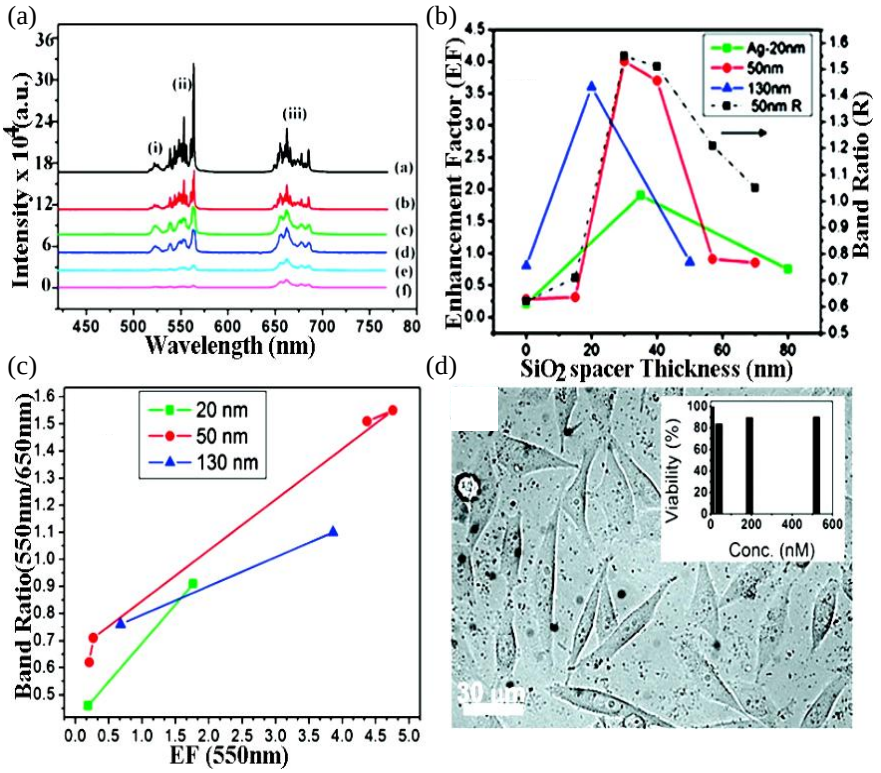


Figure 1.22 Upconversion spectra of Ag-core/SiO_2-spacer/20 nm-Y_2O_3 (a) Ag-50nm/SiO_2-30nm/Er:Y_2O_3 (b) No Ag, Er:Y_2O_3 (c) Ag-50nm/SiO_2-70nm/Er:Y_2O_3 (d) Ag-130nm/Er:Y_2O_3 (e) Ag-50nm/Er:Y_2O_3 and (f) Ag-20nm/Er:Y_2O_3 (c) Enhancement factors (EF) (d)eraged between 550 and 650 nm for the uiee Ag sizes, and (black trace) normalized integrated green to red intensity ratio (Band Ratio) for Ag-50nm/SiO_2-30nm/Y_2O_3:Er as a function of the SiO_2 spacer thickness. (c) Band ratio versus EF at 550 nm for the three Ag cores/spacers with an EF less than or equal to the maximum. (d) Prostate cancer cell imaging after overnight incubation with particles and cell viability graph as inset, adapted from (Zhang, 2010).

The plasmonic and fluorescent components of the Ag/SiO_2/Yb:Er:Y_2O_3 however were not spectrally matched as shown in Figure 1.23, thus energy transfer between the two components was not optimal.

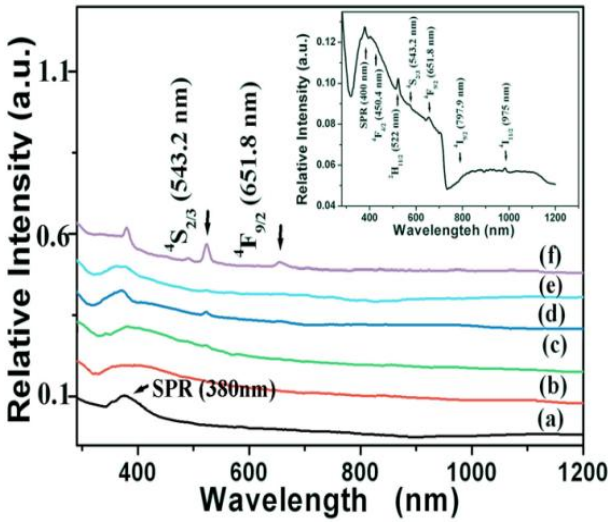


Figure 1.23 UV-vis-NIR absorption spectra of (a) Er:Y_2O_3 hollow nanospheres; (b) Ag-50nm/Er:Y_2O_3 hollow nanospheres; (c) Ag-50nm/SiO_2-30nm/Er:Y_2O_3 hollow nanosphere; (d) Ag-50nm/SiO_2-70nm/Er:Y_2O_3 nanospheres; (e) Ag-50nm/SiO_2 nanospheres and (f) 50 nm Ag nanoparticles, adapted from (Zhang, 2010).

Additionally, the SiO_2 spacer layer thicknesses were great than 50 nm, meaning that the electromagnetic near field intensity experienced by the rare earth ion emitters was significantly decayed compared to the plasmonically enhanced near field at the Au nanoparticle surface. Priyam *et. al.* reported Au nanoshell encapsulation of silica-coated Yb:Er:$NaYF_4$ upconversion nanoparticles in which they tuned the LSPR peaks in a wide wavelength range by controlling the gold shell thickness, as show in

Figure 1.24, but the plasmon spectral width of the gold shell is broader than the emission line widths of the rare earth ions and hence energy transfer between the two components is not optimal.

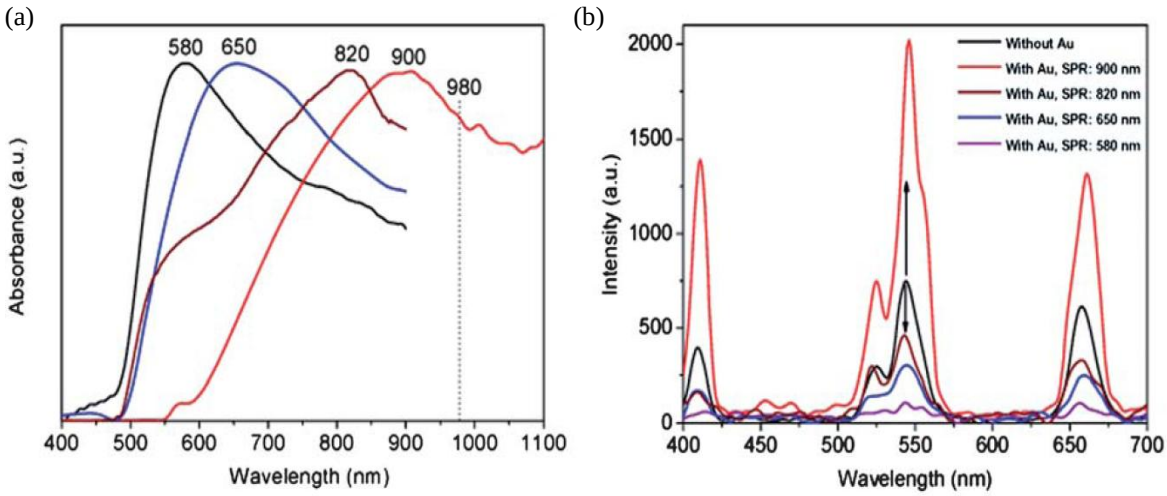


Figure 1.24 (a) Absorption spectra of Au-shell encapsulated silica coated Yb:Er:$NaYF_4$ (b) Fluorescence spectra of silica coated Yb:Er:$NaYF_4$ before and after encapsulation with Au nanoshells with different thickness and SPR peaks. For all the fluorescence measurements, the concentration was fixed at 20 μM $NaYF_4$ nanocrystals and the laser excitation density was 35 $mWcm^{-2}$. Adapted from (Priyam, 2012).

$Au/SiO_2/Yb:Er:Y_2O_3$ and $Au/SiO_2/Yb:Tm:Y_2O_3$ core/shell nanorods in which the Au nanorod extinction peak is spectrally matched to the emission peaks of Er^{3+} and Tm^{3+} and the ions are placed in the nanorod near field region have not been demonstrated. This nanostructure optimizes the energy transfer between the plasmonic and the fluorescent component because the plasmonic mode of an Au nanorod has a narrower linewidth than SiO_2/Au core/shell nanospheres and can be tuned more precisely to the emission wavelengths of rare earth ion emitters. A schematic illustration of the proposed $Au/SiO_2/Yb:Er:Y_2O_3$ and $Au/SiO_2/Yb:Tm:Y_2O_3$ core/shell nanorods is shown in Figure 1.25 (a). The normalized extinction and emission spectra of the plasmonic/fluorescent core/shell nanorods along with the normalized absorption spectra of blood, fat and water (principle optically absorbing components of tissue) are shown in Figure 1.25(b).

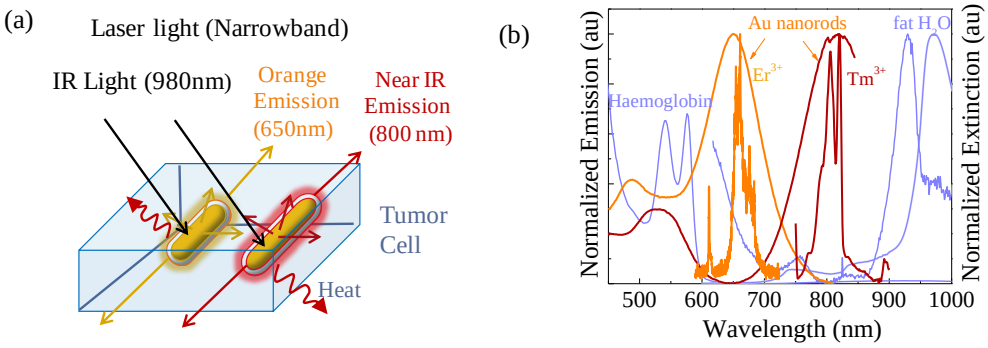


Figure 1.25 (a) A schematic illustration of light absorption, heat dissipation and rare earth light emission by spectrally tuned plasmonic/fluorescent gold/silica/rare earth doped yttria core/shell nanorods for cancer photothermal therapy and bioimaging (b) Normalized absorption spectra of blood, fat and water along with experimentally measured emission spectra of $^4F_{9/2} \rightarrow {}^4I_{15/2}$ energy transition of Er^{3+} (655nm)

In order to spectrally match the 655nm Er^{3+} energy transition ($^4F_{9/2} \rightarrow {}^4I_{15/2}$), Au nanorods of aspect ratio ~ 2.5 are needed, while in order to match the 800nm Tm^{3+} energy transition ($^3H_4 \rightarrow {}^3H_6$), Au nanorods of aspect ratio ~ 4 are needed. In order to maximize the energy transfer between the plasmonic and fluorescent components of the hybrid core/shell nanoparticle, the silica spacer layer should be thin and between 0.5nm and 2nm. The Yb^{3+}, Er^{3+} and Tm^{3+} ion compositions that result in the highest emission intensities depend on the host material. Jing et. al determined that the optimal concentration of Tm^{3+} is about 1 at% for a Yb^{3+} concentration of 10 at% for the blue upconverted emission using 980nm excitation in Yb:Tm:$NaY(WO_4)_2$ (Jing, 2006). Tikhomirov *et. al.* found that the most intense green emission band at 545 nm was observed for a 3:1 Yb:Er ratio in oxyfluoride glasses ($(SiO_2)_9(AlO_{1.5})_{32}(CdF_2)_{22}(PbF_2)_{4.0}(ZnF_2)$:x($ErF_3$):z($YbF_3$)) where x and z were varied in the study to determine the optimum ratio. In their study, they found that when the total

content of Er^{3+} and Yb^{3+} dopants increased up to 10 and more mol%, the intensity of up-conversion luminescence bands decreased substantially. They attributed this to energy migration amongst Yb^{3+} ions with eventual transfer to luminescence traps (Tikhomirov, 2012). Melkumov *et. al*. found that the optimal Yb^{3+} concentration for lasing from phosphosilicate glasses was between 6-8wt% and the optimal Er^{3+} concentration was between 0.1-0.4wt% (Melkumov, 2010). Hirai *et. al*. synthesized Yb:Er:Y_2O_3 nanoparticles and found that the 662nm emission peak reached a maximum intensity for an 8:1 Yb:Er ratio (Hirai, 2002).

When the LSPR frequency of the Au nanorod is tuned to a specific energy transition, it can increase its transition probability by providing a higher local density of photonic states and hence lead to higher emission rates or preferential emission from a specified frequency (Noginova, 2009). Additionally, through energy transfer from the fluorescent ion to the plasmonic component, hybrid plasmonic/fluorescent nanorods may be able to achieve higher heating rates compared to plasmonic nanorods.

This thesis focuses on the design, simulation, synthesis and characterization of spectrally tailored plasmonic core/shell nanorods as light trapping agents in organic photo-voltaics and for photo-thermal tumor therapy.

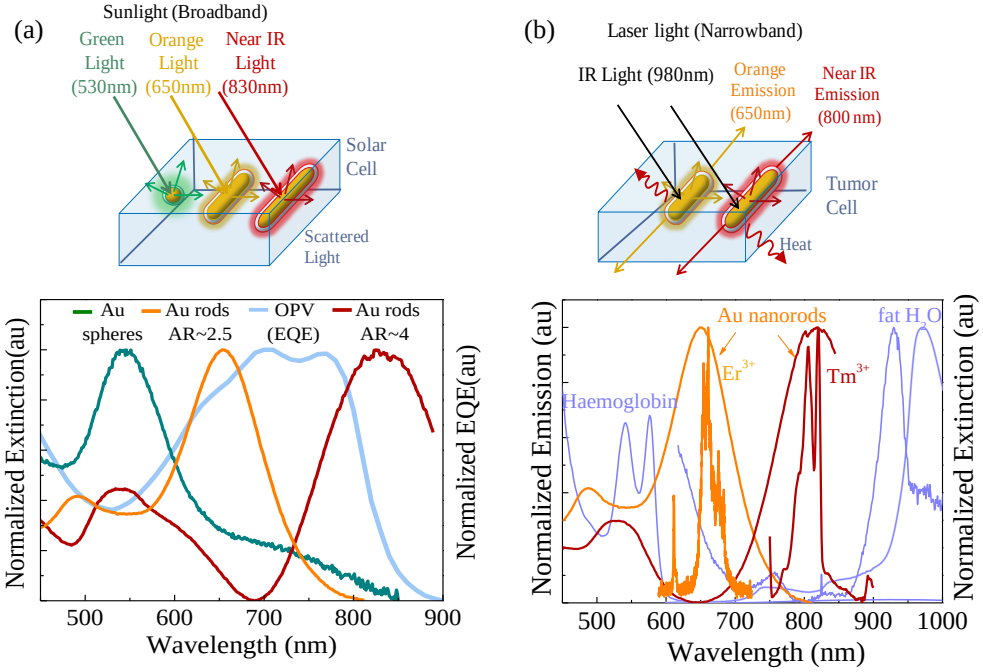


Figure 1.26 (a) A schematic illustration of light scattering by active layer incorporated, spectrally tuned Au/SiO_2 core/shell nanorods for OPV light trapping (b) A schematic illustration of light absorption, heat dissipation and rare earth ion light emission by spectrally tuned Au/SiO_2/Yb:Er:Tm:Y_2O_3 core/shell nanorods for photo-thermal tumor therapy.

CHAPTER 2 SIMULATION, SYNTHESIS, CHARACTERIZATION

Theoretical simulations were combined with experiments in order to realize Au/SiO_2 and $Au/SiO_2/Yb:Er:Y_2O_3$ core/shell nanospheres and nanorods with optical properties tailored for two technological applications: solar cells and cancer therapy.

For solar cell applications, organosilane-functionalized Au/SiO_2 core/shell nanorods with spectrally light scattering properties were incorporated in the active layers of two OPV polymers: P3HT:$PC_{60}BM$ and PBDTT-DPP:$PC_{60}BM$. In order to make the most effective use of light-trapping, the peak LSPR extinction wavelength of the Au/SiO_2 nanorods embedded in the active layers was tailored to match wavelength regions in which the OPV device has low photon conversion efficiency (PCE), for example, near the band edge.

For the tumor therapy application, $Au/SiO_2/Yb:Er:Y_2O_3$ and $Au/SiO_2/Yb:Tm:Y_2O_3$ plasmonic/fluorescent core/shell nanorod-based photosensitizer in which the Au nanorod LSPR frequency was matched to the $^4F_{9/2} \rightarrow {}^4I_{15/2}$ emission line of Er^{3+} (~ 660nm) and the $^3H_4 \rightarrow {}^3H_6$ emission line of Tm^{3+} (~ 800 nm) were synthesized, characterized and applied to both *in-vivo* and *in-vitro* cancer therapy. In order to maximize tissue penetration, photo-thermal sensitizers are designed to absorb and emit light in spectral regions where tissue absorbs light poorly, i.e. within the biologically transparent window. The hybrid plasmonic/fluorescent core/shell nanorod-based photosensitizers proposed in this work have an additional requirement that the extinction frequency of the plasmonic component (the Au nanorod) is resonant with the emission frequency of the fluorescent component (Er^{3+} and Tm^{3+}).

2.1 Simulation to Tailor Optical Properties of Au Nanorods

The response of a material to an electric field is expressed in a succinct format by Maxwell's equation:

$$\nabla \times H = J_i + \sigma E + i\omega\varepsilon E \tag{2.1}$$

where

σ : conductivity (Ω^{-1})

E : electric field (V/m)

ε : dielectric permittivity (F/m)

E : electric field (V/m)

J_i : external current density (A/m^3)

$\nabla \times H$: gradient of magnetic field (A/m^3)

The conductivity is a measure of the response of the free charge to an electric field while the dielectric permittivity is a measure of the response of the bound charge or polarization of the material due to: (a) molecules arranged in such a way as to exhibit an imbalance of charge, (b) ions with inherently oppositely charged parts, and (c) field-induced electron cloud position shift relative to the nucleus. The dielectric permittivity also depends on frequency, due to the fact that a material's polarization does not respond instantaneously to an applied field. The response is causal (arising after the applied field) and can therefore be represented by a phase difference. In the complex domain:

$$\varepsilon(\omega) = \varepsilon'(\omega) + i\varepsilon''(\omega) \tag{2.2}$$

where:

ε' : real part of the permittivity (F/m)

ε'' : imaginary part of the permittivity (F/m)

Dielectric dispersion, the dependence of the permittivity of a dielectric material on the frequency of an applied electric field, occurs because there is always a lag between changes in polarization and changes in an electric field. Dipolar polarization cannot follow the electric field at microwave frequencies (around 1010 Hz); in the infrared or far-infrared region (around 1013 Hz); ionic polarization and molecular distortion polarization lose the response to the electric field; and electronic polarization loses its response in the ultraviolet region (around 1015 Hz). In the frequency region above ultraviolet, permittivity approaches the permittivity of the free space. Figure 2.1 shows a schematic diagram of the real and imaginary components of dielectric permittivity as a function of frequency as well as the frequency regimes of dipolar, ionic, atomic and electronic material polarization.

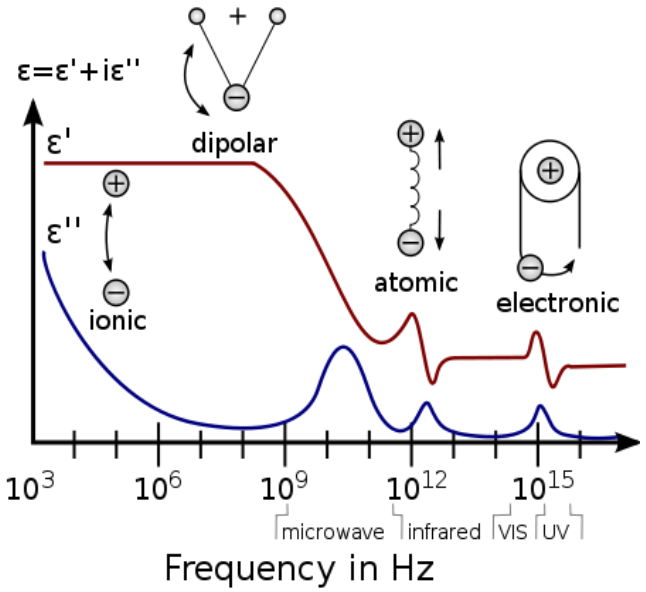


Figure 2.1 Dielectric permittivity as a function of frequency. ε′ and ε″ denote the real and the imaginary part of the permittivity, respectively. Adapted from (Johnson, 1972).

Equation (2.1) can be rewritten in terms of the real and imaginary components of the dielectric permittivity as:

$$\nabla \times H = J_i + i\omega\varepsilon' \left(1 - i\frac{\sigma}{\omega\varepsilon'} + i\frac{\varepsilon''}{\varepsilon'}\right) E \tag{2.3}$$

The term $\sigma/(\omega\varepsilon')$ describes loss due to collisions of electrons with other electrons and atoms, while $\varepsilon''/\varepsilon'$ describes how much energy supplied by an external electric field is dissipated. Dielectrics are associated with lossless or low-loss materials and $\sigma/(\omega\varepsilon') << 1$. A perfect dielectric is a material that has no conductivity, thus exhibiting only a displacement current. If $\sigma/(\omega\varepsilon') >> 1$, the material is a good conductor. An electric field cannot exist inside a good conductor such as a metal, because the electrons compensate the field. At optical frequencies, light is reflected (giving metals their shiny appearance) only up to certain frequency (the metal plasma frequency). Above the metal plasma frequency, the external field oscillates too fast for the electrons to follow and metals lose their reflectivity.

This frequency-dependent reflectivity of metals can be modeled with the Drude free electron model. The Drude model is classical in its approach that considers the material to be a 'gas' of free electrons interspersed among some arrangement of relatively heavy positive ions. The combination of these positive ionic cores and the 'gas' of electrons is neutral overall and is called a plasma while the collective oscillations of these free electrons under the influence of an external electric field are called plasmons. These free electrons may be treated as classical particles according to:

$$m\frac{d^2x}{dt^2} + b\frac{dx}{dt} + \mathrm{kx} = qE \tag{2.4}$$

where:

x : electron displacement (m)

m: mass of electron ($9.109 \cdot 10^{-31}$kg)

b : radiation damping (due to inelastic collisions) (Ns)

k : restoring force (N)

E : electric field felt by oscillator (V/m)

If the motion of the perturbed electrons in response to the electromagnetic field is periodic in time, the solution to equation (2.4) is:

$$x = \frac{\left(\frac{q}{m}\right)E}{\omega_o^2 - \omega^2 - i\gamma\omega} \tag{2.5}$$

where $\omega_o = k/m$ and $\gamma = b/m$. The electric polarization P (dipole moment per unit volume) is the product of the displacement of the electrons times the charge and can be expressed in terms the dielectric permittivity:

$$P = Np = Nqx = \frac{\omega_p^2 \varepsilon_o E}{\omega_o^2 - \omega^2 - i\gamma\omega} \tag{2.6}$$

Hence the real and imaginary components of the dielectric permittivity can be written as:

$$\varepsilon'(\omega) = 1 - \frac{\omega_p^2}{\omega^2 + i\omega\gamma} \tag{2.7}$$

$$\varepsilon"(\omega) = \frac{\omega_p^2}{\omega(\omega^2 + \gamma^2)} \tag{2.8}$$

where:

ω_p : metal plasma frequency ($\sqrt{Nq^2/m\varepsilon_o}$).

Figure 2.2(a) shows reflectance spectra of silver and gold, Figure 2.2 (b) shows the real and imaginary dielectric permittivities of the two metals obtained by ellipsometry from a 100 nm thin film, while Figure 2.3 shows the Drude model for silver and measured data.

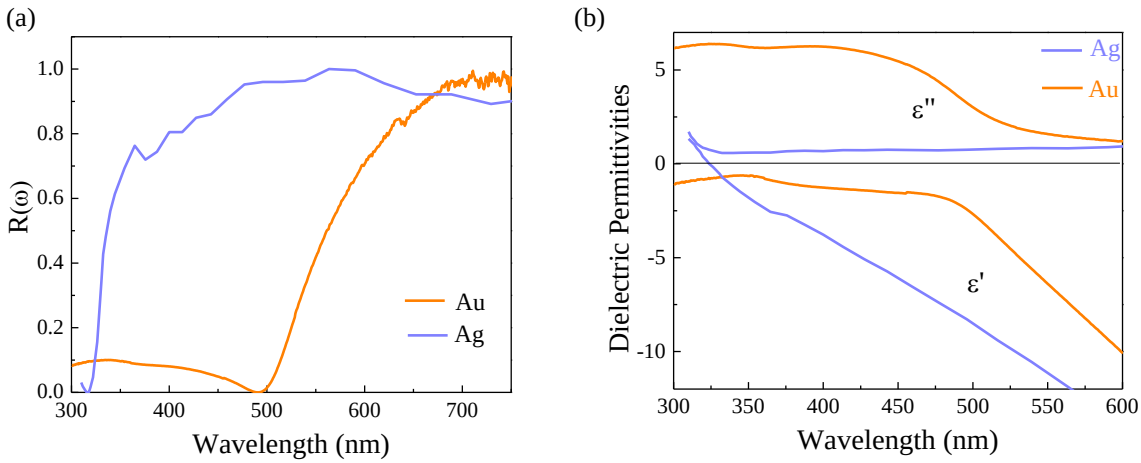


Figure 2.2 (a) Real (ε') and imaginary (ε") dielectric permittivity functions of Au and Ag. (b) Reflectivity of Au and Ag as a function of frequency.

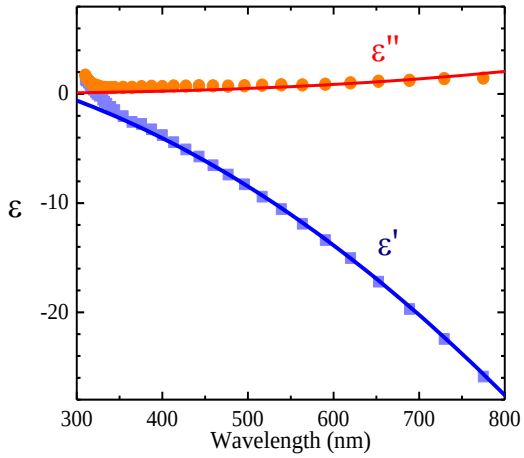


Figure 2.3 Experimentally obtained values (symbols) of real ε' and imaginary ε" dielectric permittivity from a 100nm thin Au film and the Drude model (lines).

In the same way as the energy of electron waves becomes quantized by confinement in a nanostructure, plasmons are affected by the boundary conditions in a thin film or a nanoparticle. Their resonance energy and color depend strongly on their size, analogous to the color change induced in semiconductor quantum dotsby confinement of electrons. In both cases, smaller particles have higher resonance frequency. Using a simple dipole model, it is possible to analytically calculate the light absorption and scattering of Au nanoparticles with simple geometries such as spheres and rods. For a subwavelength particle in an electrostatic field:

$$E_1 = -\nabla\Phi_1;\ E_2 = -\nabla\Phi_2 \tag{2.9}$$

$$\nabla^2\Phi_1 = 0;\ \nabla^2\Phi_2 = 0 \tag{2.10}$$

where:

Φ_1 : potential inside nanoparticle (V)

Φ_2 : potential outside nanoparticle (V)

E_1: : electric field inside nanoparticle (V/m)

E_2 : electric field outside nanoparticle (V/m)

At the interface between the nanoparticle and the medium, the potentials must satisfy:

$$\Phi_1 = \Phi_2 \tag{2.11}$$

$$\varepsilon_1 \frac{d\Phi_1}{d\mathrm{r}} = \varepsilon_2 \frac{d\Phi_2}{dr} \tag{2.12}$$

For a sub-wavelength size sphere, equations (2.9) and (2.10) with boundary conditions (2.11) and (2.12) are satisfied by:

$$\Phi_1 = -\frac{3\varepsilon_m}{\varepsilon_1 + 2\varepsilon_m} E_o r cos\theta \tag{2.13}$$

$$\Phi_2 = -E_o r cos\theta + a^3 E_o \frac{\varepsilon_1 - \varepsilon_m}{\varepsilon_1 + 2\varepsilon_m} \frac{cos\theta}{r^2} \tag{2.14}$$

where:

a : nanosphere radius (a<<λ) (m)

ε_1 : dielectric permittivity of noble metal nanosphere (F/m)

ε_m : dielectric permittivity of medium (F/m)

r : radial distance from dipole (m)

From equation (2.14), it follows that the field outside the sphere is the superposition of the applied field and the field of an ideal dipole with moment, p:

$$p = 4\pi\varepsilon_m r^3 \frac{\varepsilon_1 - \varepsilon_m}{\varepsilon_1 + 2\varepsilon_m} E_o \tag{2.15}$$

Thus the applied field induces a dipole moment proportional to the field. The ease with which the sphere is polarized is specified by the polarizability α:

$$\alpha = 4\pi r^3 \frac{\varepsilon_1 - \varepsilon_o}{\varepsilon_1 + 2\varepsilon_o} \tag{2.16}$$

Changing the shape of the particle modifies the coupling strength between the electron and the ionic core of the particle and alters the plasmon resonance energies. For non-spherical particles, multiple resonances appear under unpolarized light, due to the difference in the size of allowed surface modes in different directions. Ellipsoidal particles are the simplest example of this type of polarization-dependent scatterer. The polarizability of an ellipsoid is obtained in a similar fashion. In the case of a prolate (rod or cigar shaped) ellipsoid, the potential outside the particle is:

$$\Phi_p = \frac{E_o cos\theta}{r^2} \frac{\frac{abc}{3}\frac{\varepsilon_1 - \varepsilon_m}{\varepsilon_m}}{1 + \frac{L_3(\varepsilon_1 - \varepsilon_m)}{\varepsilon_m}} \quad (r \gg a) \tag{2.17}$$

where a : ellipsoid transverse radius (a<<λ) (m)

b : ellipsoid longitudinal radius (b<<λ) (m)

c : ellipsoid length (c<<λ) (m)

L_3 : geometric parameter (au)

The dipole moment is:

$$p = -4\pi\varepsilon_m abc \frac{\varepsilon_1 - \varepsilon_m}{3\varepsilon_m + 3L_3(\varepsilon_m - \varepsilon_o)} E_o \tag{2.18}$$

and the polarizability is:

$$\alpha = -4\pi abc \frac{\varepsilon_1 - \varepsilon_o}{3\varepsilon_o + 3L_3(\varepsilon_m - \varepsilon_o)} \tag{2.19}$$

A metal particle attenuates a beam of light in which it is placed, partly by absorption, and partly by scattering. For a spherical nanoparticle that is much smaller than the wavelength of the incident light, its response to the oscillating electric field can be described by the so-called dipole approximation of Mie theory. In this approximation the wavelength-dependent extinction cross section of a single particle, $C_{ext}(\lambda)$, which defines the energy losses in the direction of propagation of the incident light due to both scattering and absorption by the particle, is described in terms of the polarizability. The efficiencies of absorption and scattering are characterized by their respective cross-sections, C_{scat} and C_{abs}. In the limit of particles with size comparable to the wavelength, the cross-sections are given by the expressions:

$$C_{scat} = \frac{k^4}{6\pi} |\alpha|^2 = \frac{8\pi^3}{3\lambda^4} r^6 \left(\frac{\varepsilon_m - \varepsilon_o}{\varepsilon_m + 2\varepsilon_o} \right)^2 \quad (2.20)$$

$$C_{abs} = k\, Im\, (\alpha) \quad (2.21)$$

The scattering cross-section of a particle of radius r is much smaller than the wavelength of the light and varies as r^6, while its absorption cross-section varies as r^3. Therefore, for very small particles, absorption is more important than scattering, while scattering becomes more important than absorption when the circumference of the particle is comparable to the wavelength of light. Calculated scattering and absorption cross sections for Au nanospheres of different sizes are shown in Figure 2.4.

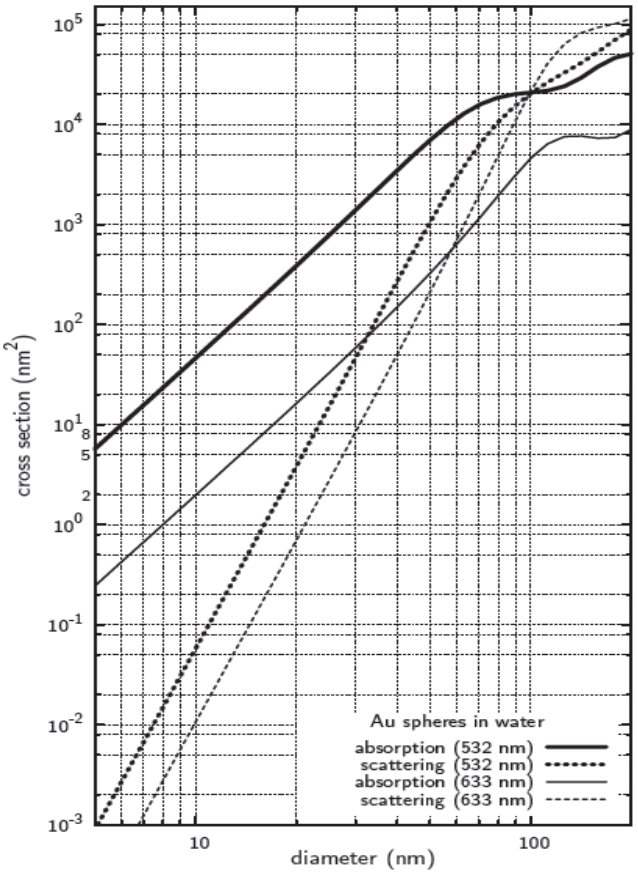


Figure 2.4 Calculated absorption and scattering cross-sections of gold nanospheres in water as a function of diameter (El-Sayed, 2001).

Besides the greatly enhanced light scattering and absorption, the induced collective electron oscillations associated with the surface plasmon resonance also give rise to local electric fields near the nanoparticle surface. The induced electric field originating from the charge separation in the nanoparticle during the plasmon resonance oscillations is very large at very small distances from the surface. For silver nanoparticles, the value of the induced field can be tens of times larger than the incident electric field value but quickly drops to smaller values as the distance from the surface increases (Campbell, 2012). The electromagnetic field intensities in the vicinity of plasmonic nanoparticles can be calculated using a finite difference time domain (FDTD) method. The FDTD algorithm employs second-order central differences in which space and time are discretized so that the electric and magnetic fields are staggered (Figure 2.5).

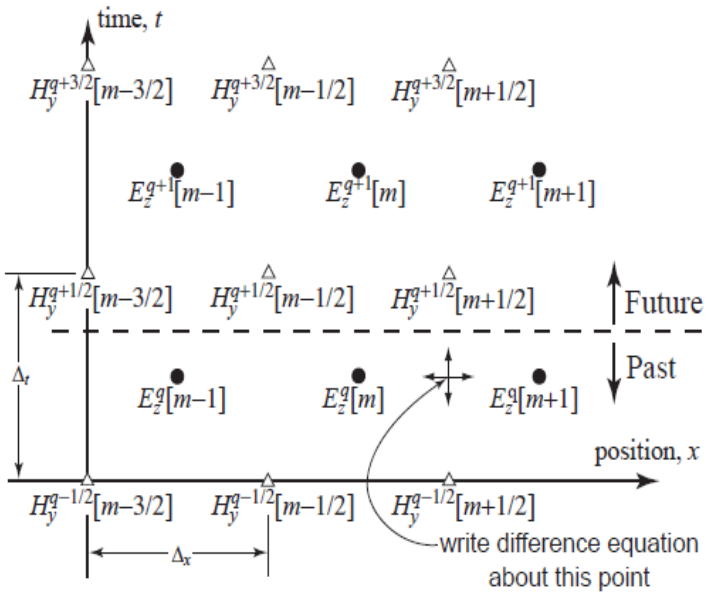


Figure 2.5 The arrangement of electric and magnetic field nodes in space and time. The electric field nodes are shown as circles and the magnetic field nodes are shown as triangles. The indicated point is expanded to obtain an update equation for H_y

Finite differences are utilized as approximations to both the spatial and temporal derivatives that appear in Maxwell's equations, specifically Faraday's and Ampere's law. For example, considering a one-dimensional space where there are only variations in the x-direction, for an electric field with only a z component, Faraday's law can be written:

$$-\mu \frac{dH}{dt} = \nabla \times E = \begin{vmatrix} \hat{a}_x & \hat{a}_y & \hat{a}_z \\ \frac{\partial}{\partial x} & 0 & 0 \\ 0 & 0 & E_z \end{vmatrix} = -\hat{a}_y \frac{\partial E_z}{\partial x} \tag{2.22}$$

Thus H_y must be the only non-zero component of the magnetic field which is time varying (the magnetic field may have non-zero components in the x and z directions but they must be static). Knowing this, Ampere's law can be written:

$$\varepsilon \frac{dE}{dt} = \nabla \times H = \begin{vmatrix} \hat{a}_x & \hat{a}_y & \hat{a}_z \\ \frac{\partial}{\partial x} & 0 & 0 \\ 0 & H_y & 0 \end{vmatrix} = \hat{a}_z \frac{\partial H_y}{\partial x} \tag{2.23}$$

The two scalar equations obtained from (2.22) and (2.23) are:

$$\mu \frac{\partial H_y}{\partial t} = \frac{\partial E_z}{\partial x} \tag{2.24}$$

$$\varepsilon \frac{\partial E_z}{\partial t} = \frac{\partial H_y}{\partial x} \tag{2.25}$$

Equation (2.22) describes the temporal derivative of the magnetic field in terms of the spatial derivative of the electric field while equation (2.23) describes the temporal derivative of the electric field in terms of the spatial derivative of the magnetic field. After replacing the derivatives in (2.24) and (2.25) with finite differences, the first equation is used to advance the magnetic field in time while the second is used to advance the electric field. The resulting difference equations are solved to obtain update

equations that express the (unknown) future fields in terms of previously computed fields.

In this work, simulations using a commercial FDTD code (Lumerical) were used to optimize the far field (extinction peak) and near field (local field enhancement) characteristics of Au/SiO_2 core/shell nanorod geometry for the targeted application.

For light trapping applications, simulations were used to determine the optimal Au/SiO_2 geometries that produce peak extinction wavelengths to match P3HT and PBDTT:DPP polymer band edges and also had strong light scattering at that frequency. For cancer therapy applications, simulations were used to determine the $Au/SiO_2/RE:Y_2O_3$ core/shell nanorod geometries that produce peak extinction wavelengths that match the $^4F_{9/2} \rightarrow {}^4I_{15/2}$ energy transition of Er^{3+} (~ 655 nm) and the $^3H_4 \rightarrow {}^3H_6$ energy transition of Tm^{3+} (~ 800 nm) and also have strong absorption at the frequencies of interest.

Figure 2.6 (a) shows simulated absorption and scattering cross section spectra for Au/SiO_2 core/shell ellipsoids of varying aspect ratios. The transverse diameter of the Au ellipsoid was the same in each simulation (10 nm), while the longitudinal diameter was varied from 20 nm to 40 nm yielding ellipsoids of aspect ratios from 2 to 4 with resonance wavelengths from 650nm to 800nm. The SiO_2 shell was 5 nm thick in each simulation. Figure 2.6(b) and (c) show the results of absorption and scattering simulations of Au/SiO_2 core/shell ellipsoids that all have the same aspect ratio (2.5) but different geometries (ellipsoid transverse diameters ranged from 10 nm to 20 nm, in accordance with experimentally obtainable geometries). Figure 2.6 (d) shows simulated absorption cross sections of Au/SiO_2 core/shell nanorods of 12 nm diameter, 30 nm length, 10 nm

thick SiO_2 shell (12 × 30, 10 nm), Au/SiO_2 core/shell nanorods of 10 nm diameter, 40 nm length with a 5 nm thick SiO_2 shell (10 × 25, 5 nm) and experimental emission cross section spectra of the $^4F_{9/2} \rightarrow {}^4I_{15/2}$ energy transition of Er^{3+} (~ 655 nm) and the $^3H_4 \rightarrow {}^3H_6$ energy transition of Tm^{3+} (~ 805 nm) (Watekar, 2008; Wang 2011).

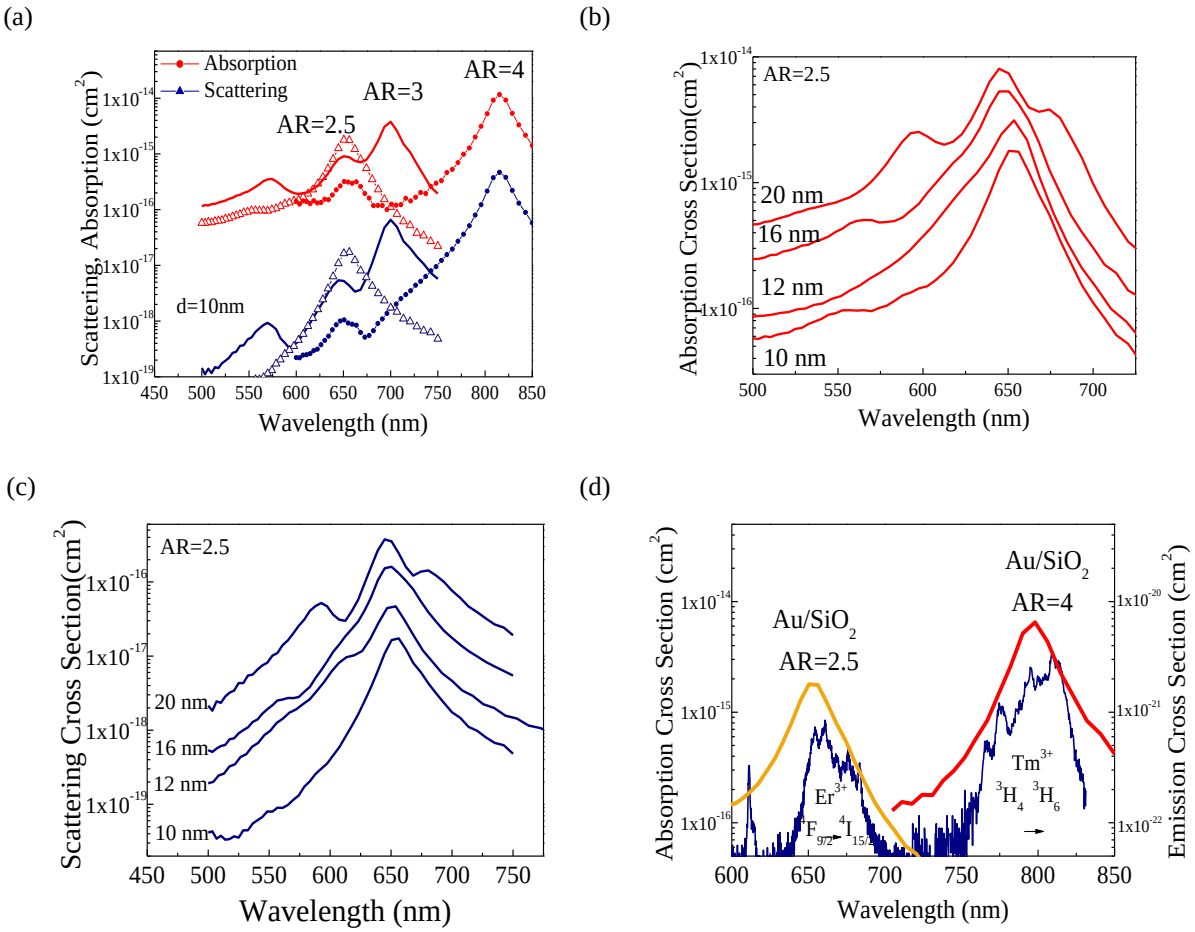


Figure 2.6 (a) Simulated absorption and scattering cross sections of Au/SiO_2 ellipsoids of different aspect ratios (transverse ellipsoid diameter is each spectrum is 10nm). Simulated (b) absorption and (c) scattering cross sections of Au/SiO_2 ellipsoids of aspect ratio 2.5 but with different (transverse ellipsoid diameter is shown next to absorption cross section) (d) Absorption sections of Au/SiO_2 core/shell nanorods (aspect ratios 2.5 and 4, SiO_2 shell thickness 10 nm) along with emission cross sections of the $^4F_{9/2} \rightarrow {}^4I_{15/2}$ energy transition of an Er^{3+} ion (peak at 655nm) and the $^3H_4 \rightarrow {}^3H_6$ energy transition of a Tm^{3+} ion (peak at 805nm)

Simulations indicate that the most important consideration in the design of Au/SiO_2 and $Au/SiO_2/RE:Y_2O_3$ core/shell nanorods is the aspect ratio (AR) since it dictates the peak plasmon resonance.

For tumor therapy and bioimaging applications, in order to match the peak extinction wavelength of the Au nanorod to the peak emission wavelength of $^4F_{9/2} \rightarrow {}^4I_{15/2}$ energy transition of Er^{3+} (~ 655 nm) nanorods of AR=2.5 are needed, while in order to match the peak extinction wavelength to the peak emission wavelength of $^3H_4 \rightarrow {}^3H_6$ energy transition of Tm^{3+} (~ 800 nm), Au nanorods of aspect ratio 4 are needed.

For light trapping applications, ideal Au/SiO_2 core/shell nanorods should have light scattering peaks resonant at OPV band edges and be incorporated into the OPV polymer active layer. For the P3HT:PC_{60}BM polymer with a band edge of ~ 670 nm, the addition of the core/shell nanorods with an aspect ratio (AR) ~ 2.5 should result in an improvement in photon conversion efficiency (PCE), while for the PBDTT-DPP:PC_{60}BM polymer with a band edge of ~ 830 nm, the addition of core/shell nanorods of AR ~ 4 should result in an improvement in PCE.

While the nanorod aspect ratio determines the peak wavelength, the Au nanorod size determines the absorption and scattering cross sections. In general, larger Au nanorods have higher absorption and scattering cross sections than smaller ones. According to simulation results, an Au nanorod with a 20 nm diameter and 50 nm length has absorption and scattering cross sections that are approximately an order of magnitude higher than those of an Au nanorod with a 10 nm diameter and 25 nm length (Figure 2.6 (c)). For light trapping applications, high light scattering cross sections are desirable but the disruption of OPV active layer morphology has to be taken into account in the design.

This is not an issue if Au nanorods are incorporated in one of the passive layers (eg. PEDOT:PSS hole trapping layer). For laser therapy applications, high absorption cross sections are desirable but again the optimal geometry for the application has to take into account the interaction of the $Au/SiO_2/RE:Y_2O_3$ core/shell nanorods with cells. In general, cancer cells uptake smaller nanorods at faster rates than larger ones.

The spatial distribution of the enhanced electromagnetic near field at the LSPR frequency is another important consideration. The enhanced local electromagnetic fields in the nanostructure near field can be utilized to modify rates of field-dependent processes such as spontaneous emission (Purcell, 1946). The first work on enhancement and suppression of spontaneous emission, sometimes called radiative decay engineering was performed by Drexhage and Kleppner at microwave frequencies (Kleppner, 1981), but has since been confirmed in different experimental settings such as close to plane interfaces (Anger, 2006), in optical cavities (Lodahl, 2004), and close to metallic nanoparticles (Bian, 1995; Dulkeith 2004; Rogobete, 2007; Noginov 2009; Saha 2009; Schietinger 2009; Gather, 2012; Priyam 2012; Pustovit, 2012; Saboktakin, 2012; Yorulmaz, 2012).

Radiative decay engineering is possible because the rate of spontaneous emission depends on two factors: an 'atomic part', which describes the internal structure of the light source (strength of a transition between two states in terms of transition moments) and a 'field part', which describes the density of electromagnetic modes of the environment. In a homogeneous medium, such as free space, the rate of spontaneous emission in the dipole approximation is given by:

$$\Gamma_{free}(\omega) = \frac{\omega^2 n^3 \left|\vec{d}_{12}\right|^2}{3\pi\varepsilon_o \hbar c^3} \tag{2.26}$$

where,

$\vec{d}_{12}$: transition dipole moment from state 1 to state 2 (C·m)

ω : emission frequency (Hz)

n : index of refraction (au)

ε_o : vacuum permittivity (F/m)

$\hbar$: reduced Planck constant (J/K)

c : vacuum speed of light (m/s)

The spontaneous emission rate of a dipole into a resonant cavity mode at a given point r follows from the Fermi golden rule:

$$\Gamma_{cav}(w) = \frac{2\pi}{\hbar^2} \langle \vec{d}_{12} \cdot \vec{E}(r) \rangle^2 \rho(\omega_e) \tag{2.27}$$

where,

$E(r)$: electric field at point r (V/m)

$\rho(\omega_e)$: density of electromagnetic modes (m^{-3})

The averaging of the dipolar matrix element is performed over the various modes seen by the emitter. The spontaneous emission rate enhancement of an emitter placed in modified electromagnetic environment (such as a mono-mode optical cavity or in proximity to an optical antenna) with respect to its free space emission rate is called the Purcell factor (PF) and can be written as:

$$PF = \frac{\Gamma_{cav}(w)}{\Gamma_{free}(w)} = \frac{\frac{2\pi}{\hbar^2}\langle \vec{d}_{12} \cdot \vec{E}(r)\rangle^2 \rho(\omega)}{\frac{\omega^2 n \left|\vec{d}_{12}\right|^2}{3\pi\varepsilon_o \hbar c^3}} = \frac{3Q\left(\frac{\lambda}{n}\right)^3}{4\pi^2 V_{eff}} \quad (2.28)$$

where

Q : quality factor of the cavity ($w/\Delta w_c$)

V_{eff} : effective mode volume $\left(\frac{\int \varepsilon(r)E^2(r)d^3r}{(\varepsilon(r)E^2(r))max}\right)$ describes how efficiently the cavity concentrates the electromagnetic field in a restricted space.

Optimal nanocavity design in the case of an $Au/SiO_2/Yb:Er:Y_2O_3$ nanorod involves maximizing the cavity quality factor Q (through single crystal Au nanorod synthesis) and minimizing the effective mode volume (by maximizing the overlap between emitter ions and regions of high photonic density of states).

Figures 2.7 – 2.10 show the spatial EM field distributions of Au/SiO_2 core/shell nanorods of two different aspect ratios (2.5 and 4) and two different SiO_2 shell thicknesses (5 and 10nm).

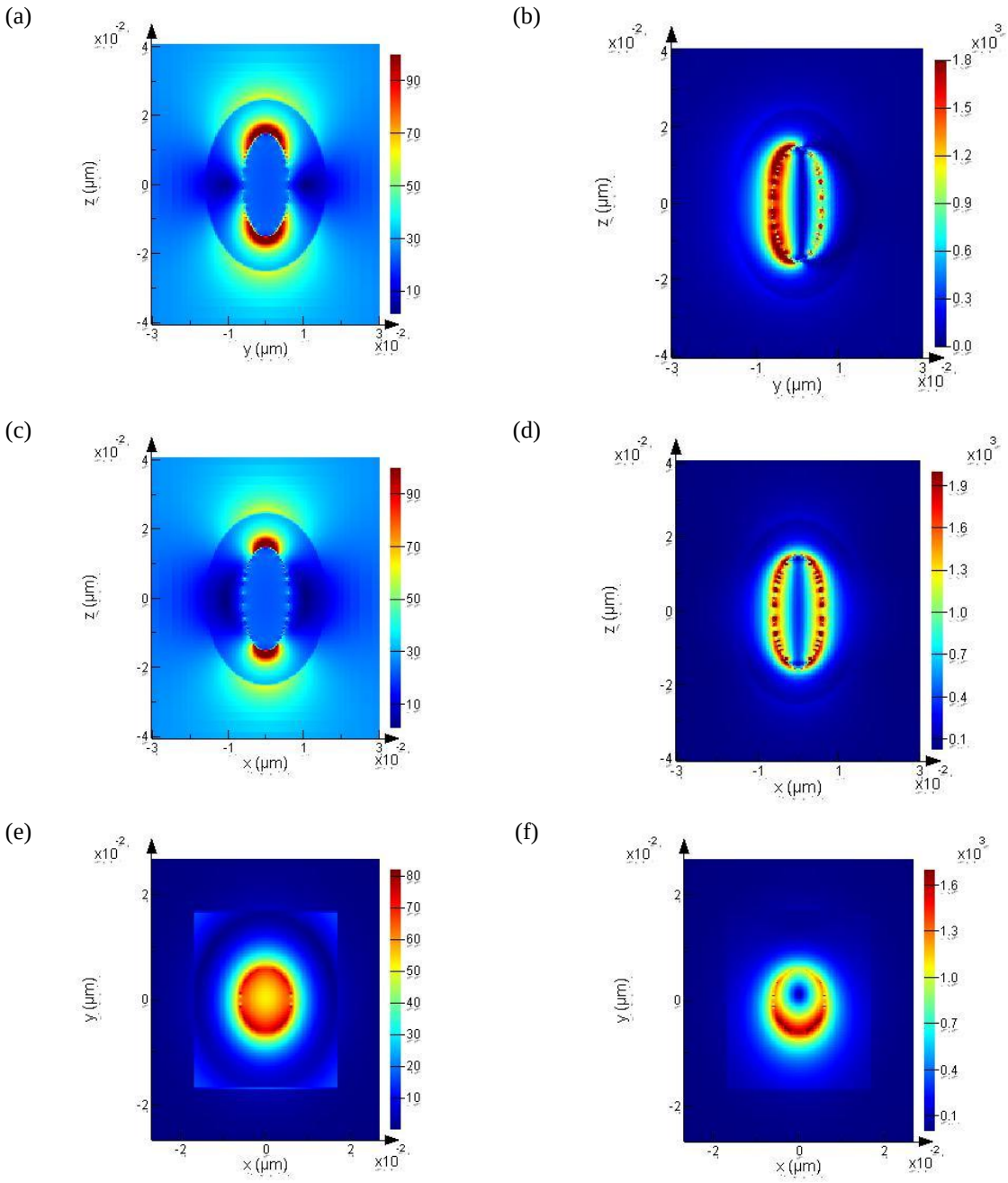


Figure 2.7 Simulation of Au/SiO_2 core/shell nanorods with Au cores of 12 nm and 30 nm in length (AR=2.5) and a 10 nm thick SiO_2 shell. The left column are off resonance (850 nm) near field simulation results for (a) ZY (c) ZX (e) YX orientations. The right column are on-resonance (655 nm) near field simulation results for (b) ZY (d) ZX (f) YX orientations.

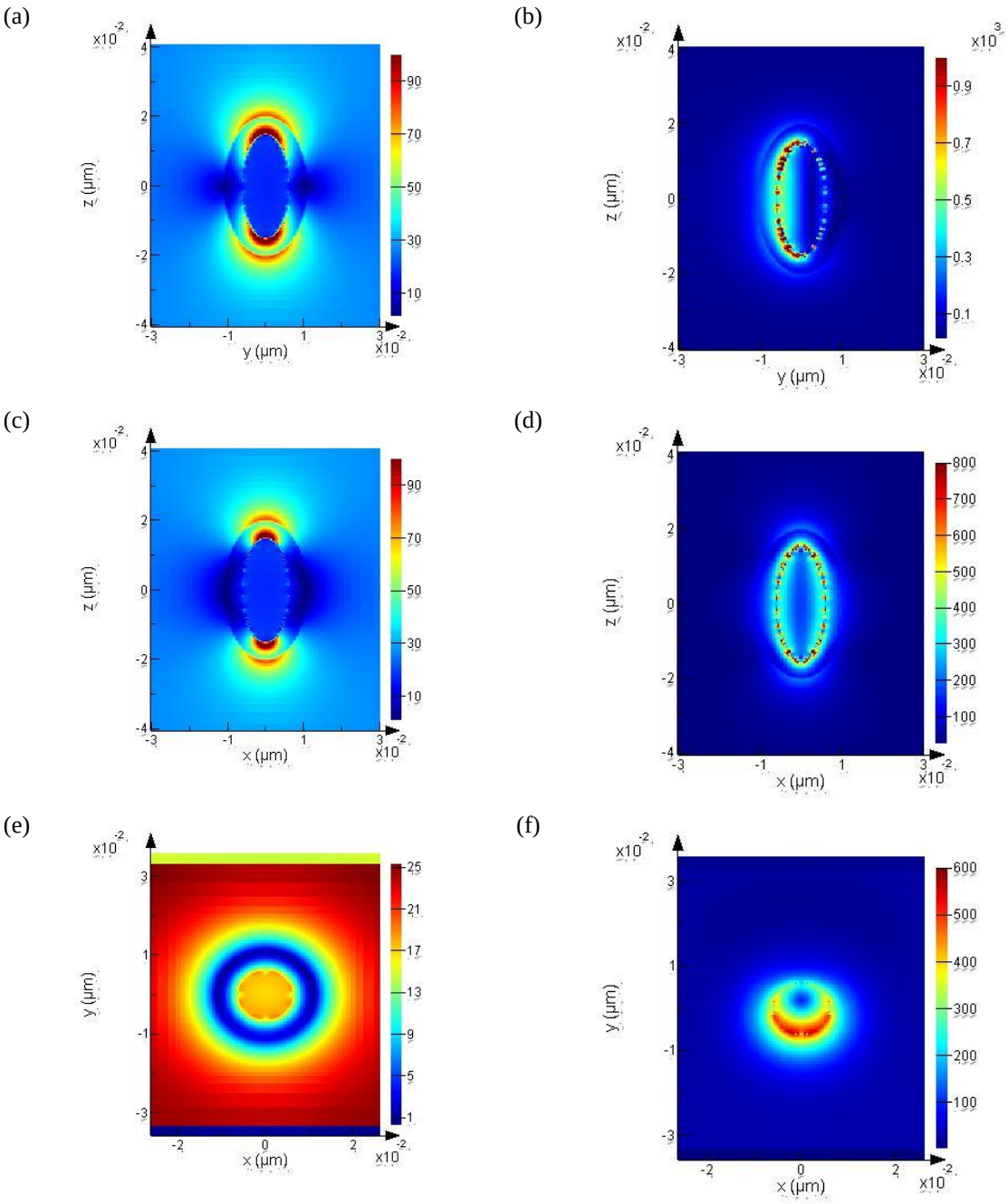


Figure 2.8 Simulation of Au/SiO_2 core/shell nanorods with Au cores of 12 nm and 30 nm in length (AR=2.5) and a 5 nm thick SiO_2 shell. The left column are off resonance (850 nm) near field simulation results for (a) ZY (c) ZX (e) YX orientations. The right column are on-resonance (655 nm) near field simulation results for (b) ZY (d) ZX (f) YX orientations

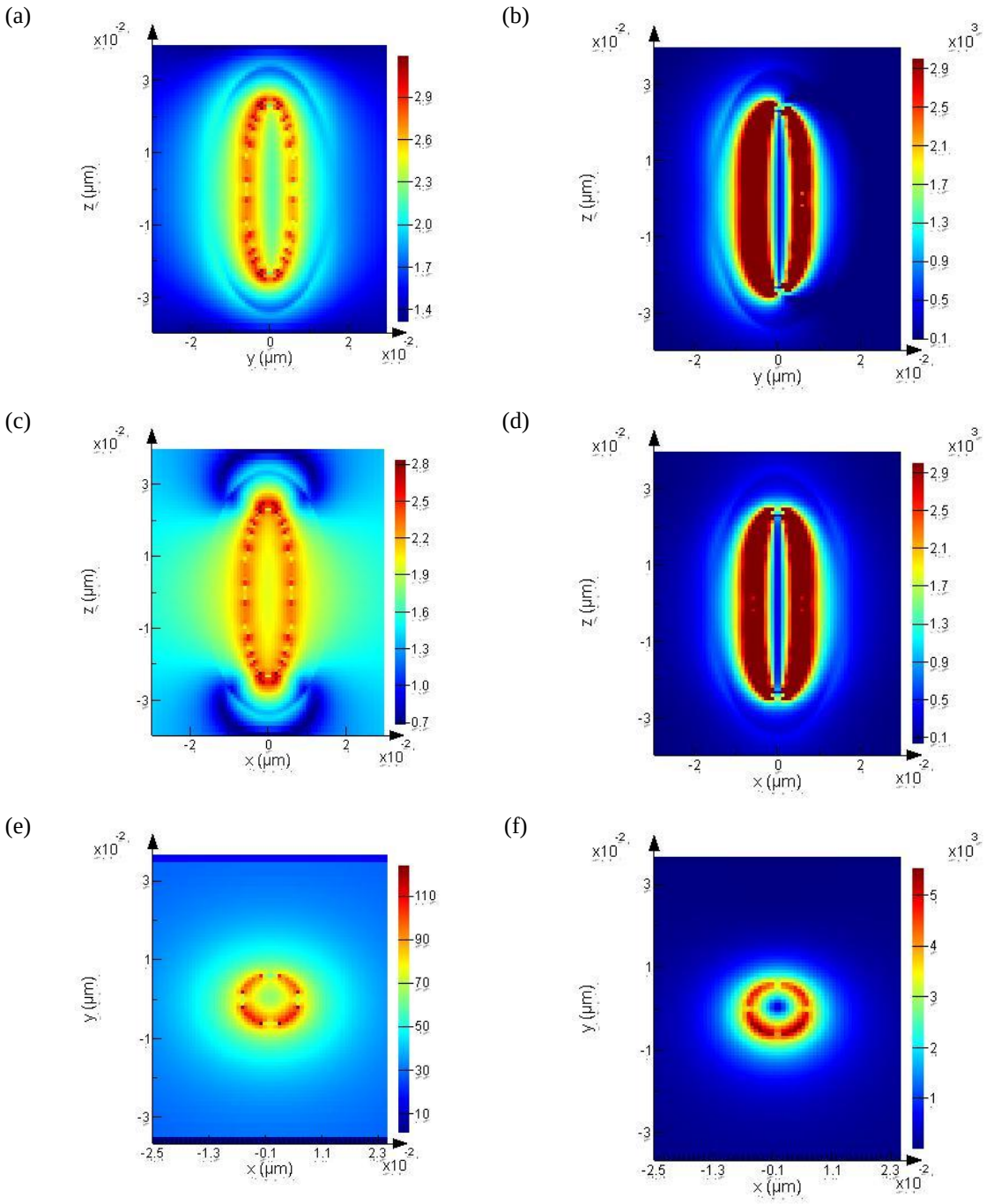


Figure 2.9 Simulation of Au/SiO_2 core/shell nanorods with Au cores of 12 nm diameter and 48 nm in length (AR=4) and a 10 nm thick SiO_2 shell. The left column are off resonance (555 nm) near field simulation results for (a) ZY (c) ZX (e) YX orientations. The right column are on-resonance (800 nm) near field simulation results for (b) ZY (d) ZX (f) YX orientations.

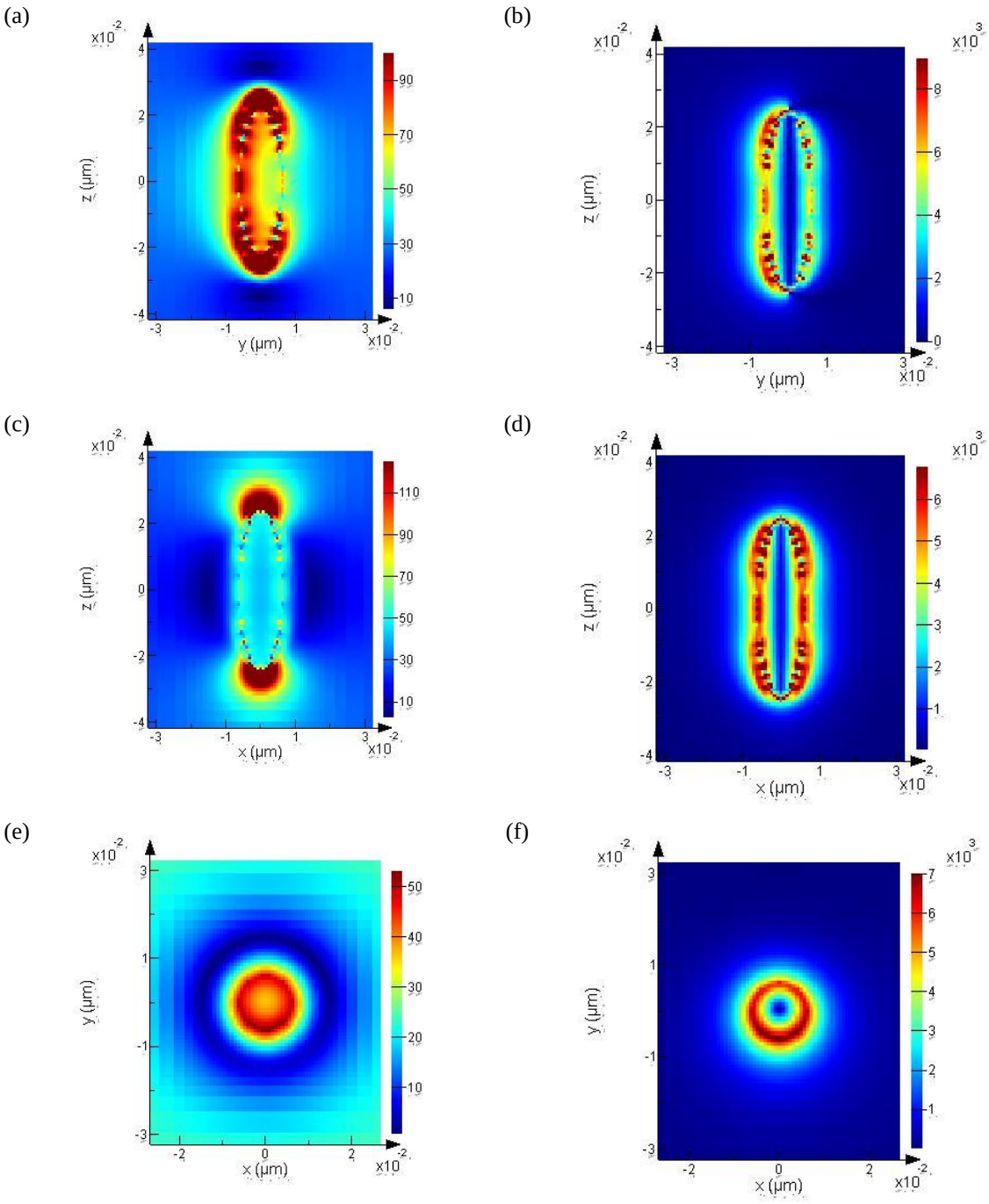


Figure 2.10 Simulation of Au/SiO_2 core/shell nanorods with Au cores of 12 nm diameter and 48 nm in length (AR=4) and a 5 nm thick SiO_2 shell. The left column are off resonance (555 nm) near field simulation results for (a) ZY (c) ZX (e) YX orientations. The right column are on-resonance (800 nm) near field simulation results for (b) ZY (d) ZX (f) YX orientations.

The absorption and emission cross sections of Er^{3+} in SiO_2 are quite small, typically on the order of 10^{-21} cm^2 for silica-based hosts (Miniscalco, 1991; Mertens, 2005). At above 1×10^{18} cm^{-3}, Er^{3+} in silica segregates to form platelets, 10-30 nm in diameter, and only a small fraction of Er^{3+} was optically active (Eaglesham, 1991). The low solubility of Er^{3+} in SiO_2 is attributed to its rigid structure (Arai, 1986). In pure silica, the tetrahedron $(SiO_4)^{2-}$ units are tightly bonded together through the bridging oxygen atoms. Erbium ions are incorporated into the small gaps in the rigid SiO_2 network and are coordinated by non-bridging oxygen atoms. At high concentrations, Er^{3+} ions tend to cluster around the limited non-bridging O to screen their electric charge, and in this way form precipitates and become optically inactive.

In contrast to SiO_2, metal oxides such as In_2O_3, Sc_2O_3 and Y_2O_3 have identical crystal structures to that of Er_2O_3 (Lide, 2001). Among these, Y_2O_3 is the ideal candidate due to its very similar lattice constant to Er_2O_3 and good ionic size match between Y^{3+} and Er^{3+} (0.90 Å versus 0.89 Å). By having the same valence states, bonding and coordination characteristics between the substituted cations, typical problems encountered in doped materials, such as lattice distortion and vacancy formation due to charge compensation, can essentially be eliminated. For comparison, a silica waveguide amplifier with an erbium concentration of ~ 4×10^{19} cm^{-3} showed a 0.6 dB/cm gain at a 1.54 μm wavelength and 264 mW pump power (Hattori, 1994). In contrast, a waveguide amplifier fabricated with Y_2O_3 can host up to 1.3×10^{20} cm^{-3} of Er, and showed a gain of 1.4 dB/cm at 1.54 μm and at a significantly lower pump power of only 12 mW (Kik, 2000).

The higher gain value obtained with the Y_2O_3 optical amplifier is derived from the higher fraction of optically active Er^{3+} in Y_2O_3 due to the higher emission cross section of Er^{3+} in Y_2O_3 compared to Er^{3+} in a SiO_2 host.

In the case of plasmonic nanocavities, a high concentration of optically active Er^{3+} is necessary to overcome optical losses associated with surface bound plasmon modes. Additionally, the emitter ions should be located in regions where the electromagnetic field is the most intense, in close proximity to the Au nanorod surface but not in contact with the metal. Based on the simulation results, an ideal $Au/SiO_2/Yb:Er:Y_2O_3$ core/shell nanorod optical cavity should have:

1. Single crystal Au nanorods of aspect ratio ~2.5 (plasmon resonance ~ 650 nm) and relatively large geometries (eg. 20 nm diameter x 50 nm length rods) in order to maximize the Au nanorod absorption cross section for optimal photo-thermal energy transduction.

2. A very thin SiO_2 shell (~ 1nm) to provide an oxide surface for the deposition of $Yb:Er:Y_2O_3$ and to mitigate the effects of luminescence quenching due to free electrons in the metal.

3. A 10 nm thick $Yb:Er:Y_2O_3$ with at least a 10^{20} cm^{-3} Er^{3+} ion concentration in the shell in order to provide sufficient gain to overcome optical losses associated with plasmon resonant electron oscillations at $\lambda = 650$ nm. This represents 5×10^4 Er^{3+} ions in a 10 nm Y_2O_3 shell around a 20x50nm Au nanorod, at a concentration of 10^{20} cm^{-3}.

An ideal $Au/SiO_2/Yb:Tm:Y_2O_3$ core/shell nanorod optical cavity should have:

1. Single crystal Au nanorods of aspect ratio ~ 4 (plasmon resonance ~ 800 nm) (eg. 10 nm diameter x 40 nm length rods)

2. A very thin SiO_2 shell (~ 1nm) to provide an oxide surface for the deposition of Yb:Er:Y_2O_3 and to mitigate the effects of luminescence quenching due to free electrons in the metal.

3. A 10 nm thick Yb:Tm:Y_2O_3 with at least a 10^{20} cm^{-3} Tm^{3+} ion concentration in the shell in order to provide sufficient gain to overcome optical losses associated with plasmon resonant electron oscillations at $\lambda = 800$ nm. This represents 5×10^4 Tm^{3+} ions in a 10 nm Y_2O_3 shell around a 20x50nm Au nanorod, at a concentration of 10^{20} cm^{-3}.

2.2 Synthesis of Au/SiO_2 and Au/SiO_2/Yb:Er:Y_2O_3 Core/Shell Nanorods

The next few sections describe the synthesis and characterization of spectrally tuned Au nanorods, Au/SiO_2 core/shell nanorods and Au/SiO_2/Yb:Er:Y_2O_3 core/shell nanorods. The synthesis of Au nanorods is first discussed with a focus on the role of cetyl ammonium trimethyl bromide (CTAB). Transmission electron microscopy (TEM) and optical spectroscopy characterization techniques are introduced in Sections 2.2.2 and 2.2.3. The correlation between the Au nanorod aspect ratio and the peak extinction wavelength of an Au nanorod colloidal solution is clarified. In Section 2.2.4, a layer by layer polyelectrolyte deposition process used to treat the Au nanorod surface in order to make it amenable to SiO_2 coating and the conditions required to deposit a thin SiO_2 shell are described. In Section 2.2.5, the protocol used to deposit a third layer consisting of Yb:Er:Y_2O_3 is discussed. In Section 2.2.6, characterization techniques including photoluminescence, radiative lifetime, photothermal measurement and external quantum efficiency measurements are described.

2.2.1 Au nanorod synthesis

Preparation of Au nanorods relies on the reduction of the Au precursor ($HAuCl_3$) preferentially on the [111] Au crystal lattice face through the use of a surfactant, cetyl tri-methyl ammonium bromide (CTAB) (Huang, 2009). CTAB is a micelle molecule with an ammonium trimethyl bromide hydrophyllic head group and a 16-carbon chain hydrophobic end and forms a chemisorbed bilayer on the surface of Au nanorods. Figure 2.11 (a) shows a schematic of an Au nanorod with a CTAB bilayer attached to the surface (Sau, 2005). The surfaces of CTAB-stabilized Au nanorods possess a positive surface charge due to the cationic head groups facing the solvent. This surface charge in turn affects the distribution of ions in the surrounding interfacial region, resulting in an increased concentration of counter ions (ions of opposite charge to that of the particle) close to the surface and leads to the formation of an electrical double layer around each particle. The liquid layer surrounding the particle exists as two parts; an inner region, called the Stern layer, where the ions are strongly bound and an outer, diffuse, region where they are less firmly attached as shown in Figure 2.11(b).

(a) (b)

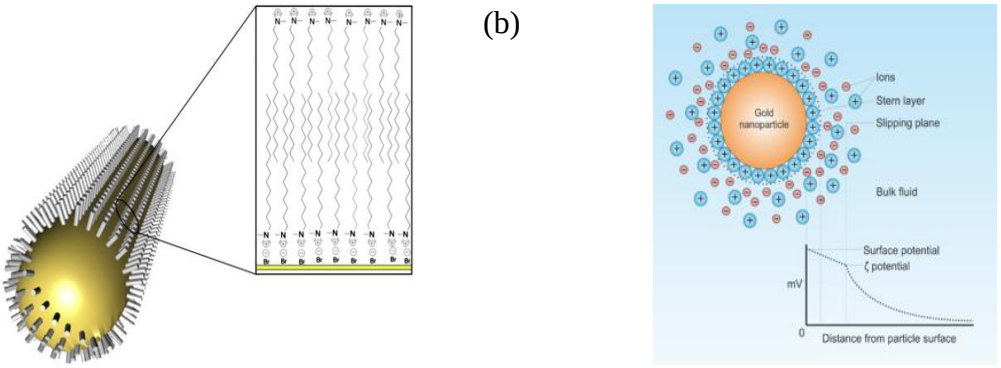


Figure 2.11 (a) Illustration of an Au nanorod with a CTAB bilayer attached (Alkilany, 2012) (b) Illustration of an Au nanoparticle in solution showing how counterions arrange themselves in response to a charged particle and the potential difference as a function of distance in the solution from the charged particle.

Within the diffuse layer there is a notional boundary inside which the ions and particles form a stable entity. When a particle moves (e.g. due to gravity), ions within the boundary move with it, but any ions beyond the boundary do not travel with the particle. This boundary is called the surface of hydrodynamic shear or slipping plane. The potential that exists at this boundary is known as the zeta potential. The magnitude of the zeta potential gives an indication of the potential stability of the colloidal system. If all the particles in suspension have a large negative or positive zeta potential then they tend to repel each other and there is no tendency to flocculate. However, if the particles have low zeta potential values then there is no force to prevent the particles coming together and flocculating. The general dividing line between stable and unstable suspensions is generally taken at either +15 mV or -15 mV. Particles with zeta potentials more positive than +15 mV or more negative than -15 mV are considered stable.

The synthesis of stable Au nanorod colloids relies on the high zeta potential of the CTAB surfactant. The protocol was first developed by Nikoobakht *et.al*.(Nikoobakht, 2003) and requires preparation of two solutions: a seed and a growth solution. In a typical synthesis, an Au seed solution is prepared by mixing 5 ml, 0.25 mM $HAuCl_4$, 5 ml, 0.1M CTAB, and 0.6 ml, 0.1 M ice cold $NaBH_4$ to produce <5nm CTAB-capped Au nanospheres. In the second phase, a growth solution is prepared by mixing 0.1 ml, 0.01 M $AgNO_3$, 20 ml, 0.5 mM $HAuCl_4$, 19.2 ml, 0.1M CTAB, and 0.7 ml, 0.77 M $C_6H_8O_6$. In order to synthesize the Au nanorods, 16 μl of the seed solution was added to the growth solution. After five minutes, the colorless growth solution transforms to a deep purple color indicating the presence of Au nanorods. In order to synthesize Au nanorods with

larger aspect ratios, different volumes of $AgNO_3$ are added to the growth solution ranging from around 0.2 ml to about 1.4 ml.

The rate of growth of the Au seeds in the presence of CTAB is controlled by the flux of Au-laden, cationic micelles to the CTAB-capped Au particles. When the surfactant-capped seed is introduced into the solution, the Au diffuses into the soft template while the surfactant becomes a part of the soft template. The template size and shape are functions of surfactant concentration and ionic strength of the solution. Au nanorods have four [110] facets that nanospheres do not. The CTAB bilayer protects the [111] crystalline plane and facilitates the growth on the [110] facets since CTAB binds more strongly to [110] facets (Alkilany, 2010). Since both the rods and the micelles possess very high zeta potentials (+90 mV), the rate of transfer of the Au(I) ions to the rods is drastically slowed down. Indeed, it is observed that Au seeds grow almost 1000 times more slowly in the presence of CTAB (Huang, 2009). The surface decays more quickly at the tips due to the higher curvature and consequently the micelle flux is higher at the tips. Calculations of the diffusion-migration rate of the micelles to the rods within the double layer confirm that the encounter rate is much higher at the tips of an Au nanorod as opposed to the sides due to the higher curvature (Rodriguez-Gonzalez, 2007). Preferential tip-oxidation of nanorods also has been reported (Perez-Juste, 2004) which strongly supports the electric field-directed interaction between Au nanoparticles and CTAB micelles. Surfactant-containing complexes are specifically incorporated into the [100] side edges, whereas non-complexed ion-pairs or Au(0) atoms/clusters are added to the [111] end faces (Pastoriza-Santos, 2010). The discrimination between sites could be due to the increased stability of the close-packed [111] surfaces. Moreover, the large

$[RNMe_3]^+$ headgroup of CTAB (diameter = 0.814 nm, area = 0.521 nm^2) and the long alkyl chain are more readily accommodated on the [100] side edges, than on close-packed [111] faces, where the Au-Au spacing is too small to facilitate epitaxy. As the nanorods grow in length, the area of the side faces increases, and this could facilitate the assembly of a bilayer of CTAB molecules at the crystal surface. The bilayer provides both stabilization and growth inhibition, and this could explain why elongation of the nanorods is rapid once the shape anisotropy has been established, in a zipping type of mechanism. Once rod formation has started, further growth is encouraged by the electric field distribution at the rod ends (Rodriguez-Gonzalez, 2007; Rodriguez-Lorenzo, 2010). Figure 2.12 (a) summarizes the synthesis protocol used to obtain Au nanorods while Figure 2.12 (b) is a schematic illustration showing a proposed growth mechanism.

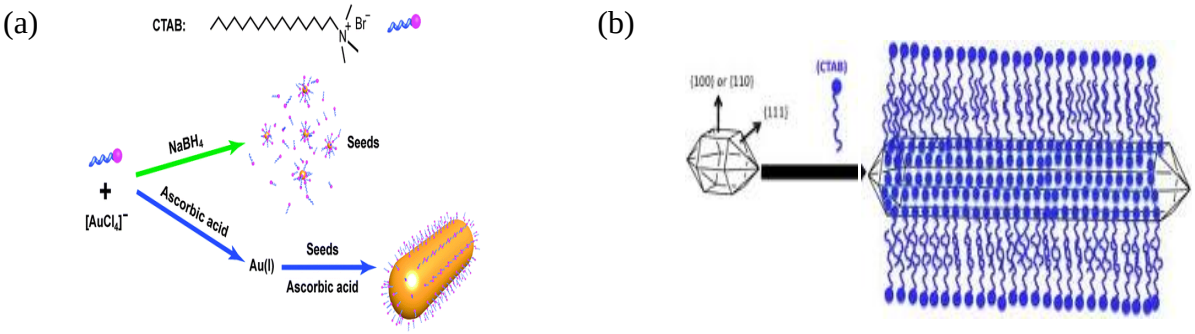


Figure 2.12 (a) Schematic illustration of the seed-mediated method for the growth of Au nanorods(Chen 2013) (b) Proposed growth mechanism of Au nanorods from an Au seed Adapted from (Alkilany 2010).

In order to investigate the role of precursor concentration on the geometry of the Au nanorods, the $AgNO_3$ concentration in the growth solution was varied while the concentrations of the other precursors were kept constant. The samples were prepared in 40ml-vials with differing amount of silver nitrate, ranging from 0.8 µmol to 3 µmol. To test the effect of $C_6H_8O_6$ growth solutions with different amounts of $C_6H_8O_6$ ranging

from 32 μmol to 100 μmol were prepared. Figure 2.13 shows (a) Au nanorod aspect ratio and peak extinction wavelength as a function of $AgNO_3$ precursor amount, (b) Au nanorod aspect ratio and peak extinction wavelength as a function of $C_6H_8O_6$ precursor amount and (c) Au nanorod longitudinal peak extinction intensity as a function of $AgNO_3$ amount, and (d) FDTD, empirical and experimentally obtained relationships between Au nanorod aspect ratio and the longitudinal plasmon peak wavelength.

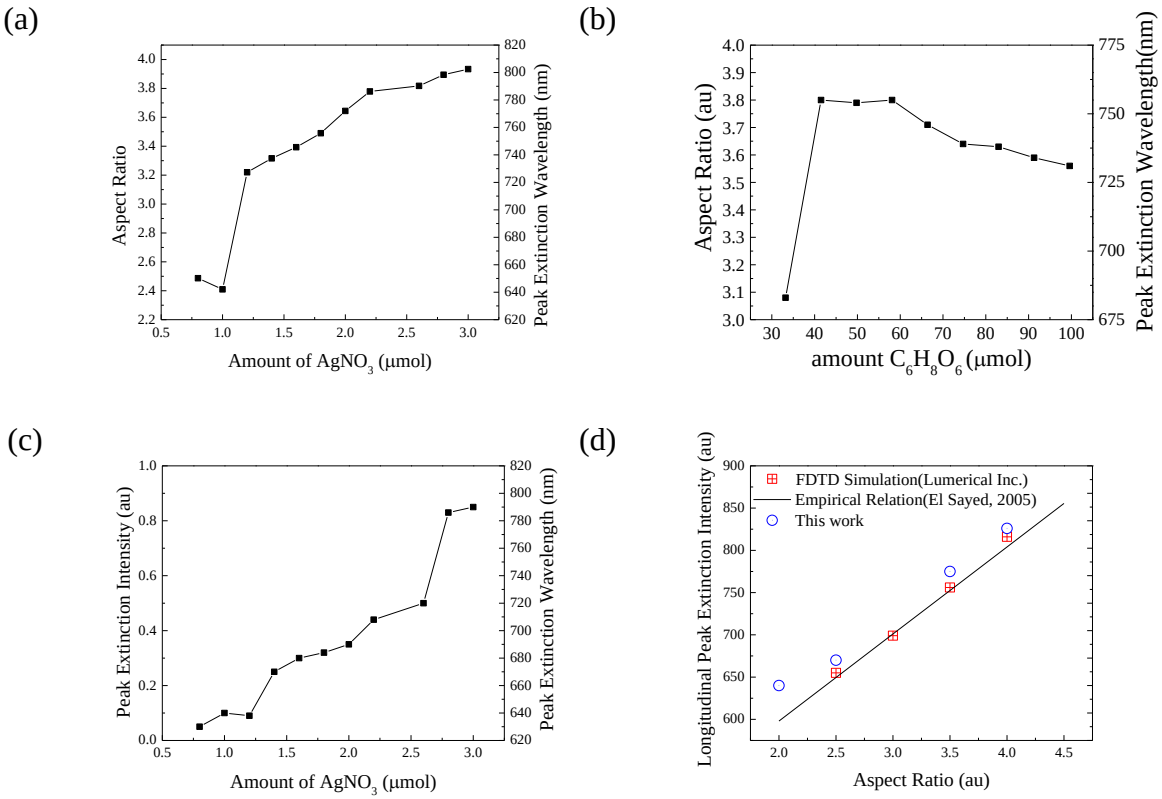


Figure 2.13 (a) Au nanorod aspect ratio and peak extinction wavelength as a function of $AgNO_3$ precursor amount (b) Au nanorod aspect ratio and peak extinction wavelength as a function of $C_6H_8O_6$ precursor amount (c) Au nanorod longitudinal peak extinction intensity as a function of $AgNO_3$ amount, and (d) FDTD, empirical and experimentally obtained relationships between Au nanorod aspect ratio and the longitudinal plasmon peak wavelength.

These results indicate that a higher concentration of $AgNO_3$ leads to an increase in peak extinction wavelength after a certain critical concentration that initiates the process (in the case of 40ml batches 1 μmol of Ag^+ ions is needed to initiate the process.

2.2.2 Silica shell deposition

The deposition of silica shells on Au nanoparticles typically requires intermediate coatings since Au metal has very little affinity for SiO_2 and does not form a passivating oxide film in solution. The surfactant plays an important role in determining what intermediate coatings are needed. SiO_2-coating of citrate-stabilized Au nanoparticles has been achieved by means of surface priming with either a silane coupling agent (Liz-Marzán, 1996) (aminopropyltrimethoxysilane, APS) or poly(vinylpyrrolidone) (PVP) (Graf, 2003), however, for CTAB-stabilized Au nanoparticles, the strong binding of the surfactant to the Au nanoparticle surface makes its displacement by APS or MPS (the equivalent mercapto-silane) molecules difficult, especially at the flat sides of the nanorods; displacement is more favorable at the tips, which has been exploited in Au nanorod end-to-end linkage protocols (Chang, 2005). Although Obare et al.(Obare, 2001) reported the use of MPS for the coating of high-aspect-ratio Au rods, other researchers have found that for small aspect ratio nanorods, the reproducibility is poor and particle aggregation (again, preferentially through the tips) is usually observed during the sodium silicate addition step (Pérez-Juste. 2004; Chang, 2005). Specifically, CTAB-coated nanoparticles were transferred into ethanol upon functionalization with the slightly negatively charged polymer, PVP, however, controlled hydrolysis and condensation of

TEOS on the nanoparticle surface could not be achieved, probably because the remaining CTAB monomers promote the formation of mesoporous SiO_2 (Pastoriza-Santos, 2004).

By exploiting electrostatic forces, polyelectrolytes (ionic polymers) have been shown to be effective at modifying the surface of metal colloids (Gittins, 2001). Polyelectrolytes have an advantage over uncharged polymers, because they can be deposited on surfaces layer-by-layer (LbL), enabling the total polymer thickness to be determined by the number of layers deposited (Decher, 1997). The LbL approach, in its simplest form, uses two solutions of oppositely charged polymers into which the substrate can be dipped (surface) (Hammond, 1999), or particles mixed (colloids)(Caruso, 2001). Sequential dipping or mixing causes material to be deposited on the surface because of electrostatic and hydrophobic interactions between the charged surface and polyelectrolyte. Once deposited, the layer of polyelectrolyte inverts the surface charge and enables a subsequent layer of polymer to be deposited from the second solution. This process can be repeated indefinitely to form a uniform multilayered film of polymeric materials.

Because of the high zeta potential of CTAB-stabilized Au nanorods ($\zeta \sim +20$ mV), LbL wrapping of negative polyelectrolyte chains around the metal nanoparticles is strongly favored. After removing excess surfactant by centrifugation, the particles were redispersed in DI water and added dropwise under vigorous stirring to an aqueous solution of polystyrene sulfonate (PSS) (2 g/L) and NaCl (6 mM). PSS adsorption was allowed to proceed for 3 h. The process was then repeated with a positively charged polyelectrolyte (poly(allylamine hydrochloride), PAH of concentration 2 g/L with 6 mM NaCl after a washing step to remove excess PSS. Two polyelectrolyte layers were found

to completely screen the effect of CTAB on the Au nanoparticle surface(Pastoriza-Santos 2006). The key point at this stage for successful SiO_2 coating is the transfer of the nanoparticles into an isopropanol (IPA)-water mixture, which is hindered by the high positive surface potential ($\zeta \sim +36$ mV) of PAH-coated nanoparticles, promoting rapid aggregation. PVP (slightly negatively charged under these experimental conditions) was used to partially screen the surface charge ($\zeta \sim +16$ mV) and allowed redispersion and ensured colloidal stability in IPA.

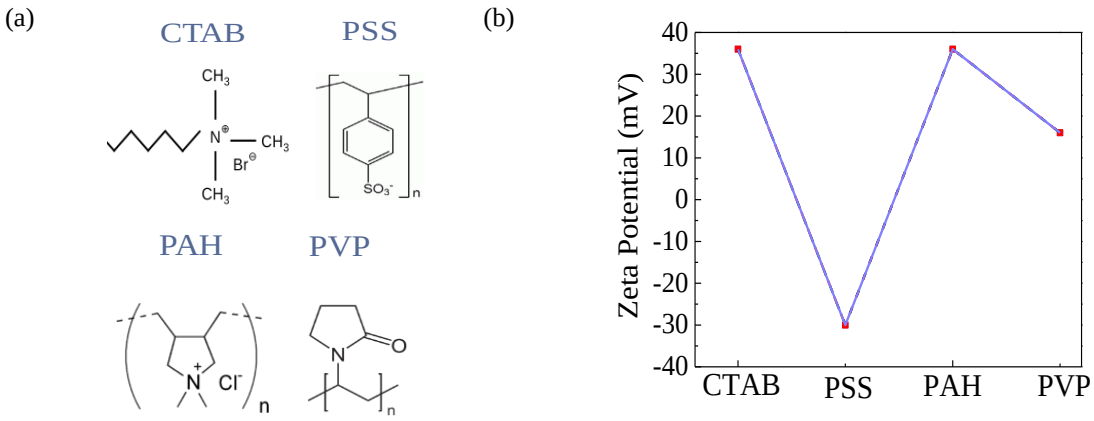


Figure 2.14 (a) Diagrams of molecular structures of CTAB, PSS, PAH and PVP surfactants (b) Zeta potential measurements of Au/CTAB, Au/PSS, Au/PAH and Au/PVP nanorods at pH 7, adapted from (Pastoriza-Santos 2006)

Once the nanorods were transferred into IPA, SiO_2 coating was achieved using the Stöber method (Stöber, 1968). The amount of TEOS precursor necessary to obtain a given thickness of SiO_2 was calculated from equation (2.29):

$$m_{TEOS} = \rho_{SiO_2}\left(V_{\frac{Au}{SiO_2}nr} - V_{Au\,nr}\right)\left(\frac{m_{Au}}{m_{Au\,nr}}\right)\left(\frac{MW_{TEOS}}{MW_{SiO_2}}\right) \quad (2.29)$$

where:

ρ_{SiO_2} : SiO_2 density (kg/m^3)

$V_{Au/SiO_2\ nr}$: Volume of 1 Au/SiO_2 core/shell nanorod (m^3)

$V_{Au\ nr}$: Volume of 1 Au nanorod (m^3)

MW_{SiO_2} : Molecular weight of SiO_2 (kg/mol)

MW_{TEOS} : Molecular weight of tetraethylorthosilicate (kg/mol)

m_{Au} : Mass of Au precursor (kg)

$m_{Au\ nr}$: Mass of 1 Au nanorod (kg)

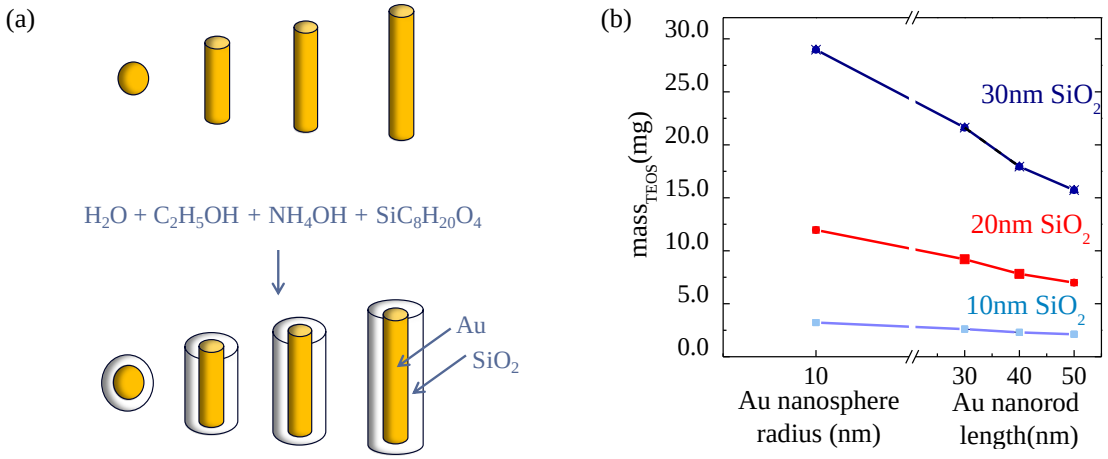


Figure 2.15 (a) Schematic diagram of SiO_2 coating process for Au nanospheres and Au nanorods of different aspect ratios (b) Mass of TEOS needed to coat 10, 20 and 30 nm SiO_2 shells on Au nanospheres and Au nanorods of 10nm radius and 30, 40 and 50nm lengths (10 ml, 0.5mM $AuCl_3$ basis).

2.2.3 Ytterbium, erbium, thulium co-doped yttria shell deposition

To coat the Au/SiO_2 core/shell nanorods with a layer of rare earth doped yttria, a sol-gel method was utilized. Deposition of the Er_2O_3 shell proceeded by creating a solution containing 5 mM urea while the mass of the $RECl_3$ salt is varied based on the desired shell thickness. The rare earth emitter doped yttria outer shell was deposited by adding the Au/SiO_2 core/shell nanorods prepared by the protocols described in 2.2.2 to a

growth solution containing chloride salts of the rare earth elements of interest in the desired concentration ratios. Equation (2.29) in which the SiO_2 density is replaced with Y_2O_3 density was used to determine the amount of YCl_3 salt needed to deposit conformal shells of Y_2O_3. The amounts of $TmCl_3$, $ErCl_3$ and $YbCl_3$ were determined from the desired ratio to the YCl_3 precursor. In order to achieve conformal coating, the mixture is stirred at 80°C for 5 hours.

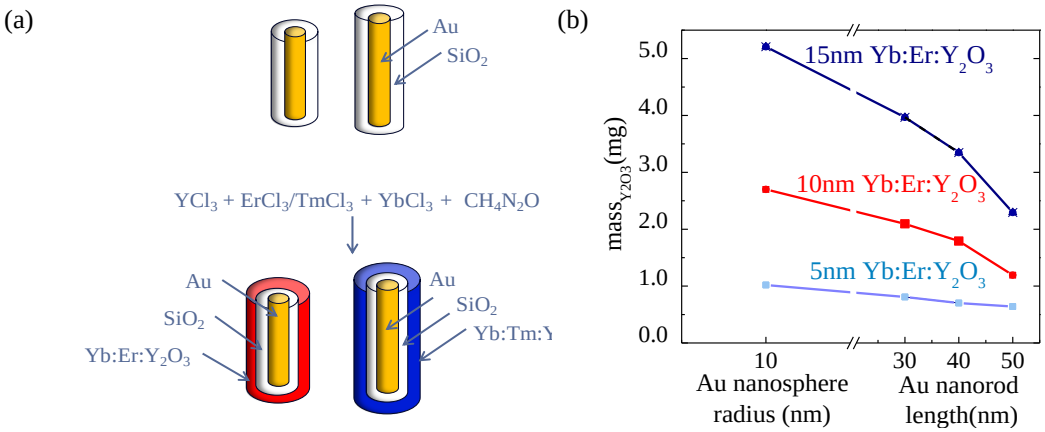


Figure 2.16 (a) Schematic diagram of $Au/SiO_2/Yb:Er:Y_2O_3$ core/shell nanorod synthesis procedure (b) Mass of Y_2O_3 needed to coat 5, 10 and 15 nm Y_3O_3 shells on Au nanospheres and Au nanorods of 10nm radius and 30, 40 and 50nm lengths (10 ml, 0.5mM $AuCl_3$ basis).

2.3 Characterization of Au Based Core/Shell Nanorods

2.3.1 Transmission Electron Microscopy

Transmission electron microscopy (TEM) with energy dispersive spectroscopy was utilized to characterize Au nanorod geometry and aspect ratio of the synthesized Au nanorods. In TEM, a beam of electrons is transmitted through the specimen and an image is formed from the interaction of the electrons transmitted through the specimen; the image is magnified and focused onto an imaging device, such as a fluorescent screen or a

charged coupled device (CCD) camera. High resolution transmission electron microscopy (HRTEM) is a method for imaging that can have resolution down to the atomic level. When used at the atomic scale, the crystal planes and growth direction can be easily calculated and indexed and can be used to determine the internal microstructure of the material. In this work, the TEM filament was excited by a high energy source and are accelerated by an electrostatic potential and focused onto a thin sample, no more than 200 nm, by a series of condenser lenses. Unlike an optical microscope, the condenser lenses do not focus the electrons based on curvature and index of refraction. A condenser lens uses a magnetic field to alter the path of the electron to converge through the thin sample and the image is projected onto a detector. To obtain diameter, size distribution and morphology information, Au nanorods were morphologically characterized using transmission electron microscopy (TEM, Tecnai 20; FEI Co., Eindhoven, Netherlands) at an acceleration voltage of 300 kV. To prepare the TEM samples, nanoparticles were diluted to a concentration of 1 mg/ml. Nanoparticle specimens for TEM were prepared by placing one drop of the diluted solution onto a carbon-coated copper grid, allowing it to dry at room temperature for 15 min. A schematic diagram of a TEM is shown in Figure 2.17 (a) while sample TEM images of Au nanorods synthesized according to the protocol described in Section 2.2.1 are shown in Figure 2.17 (b).

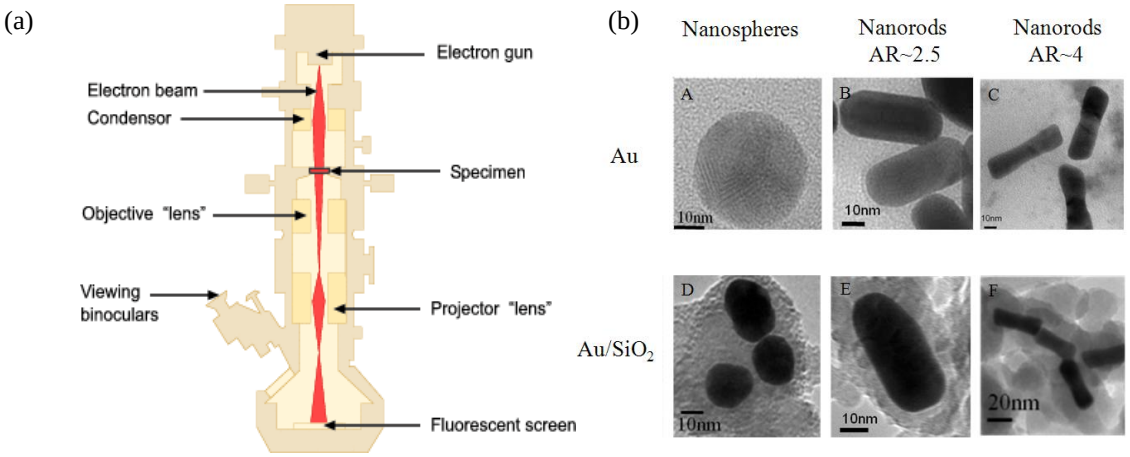


Figure 2.17 (a) Schematic diagram of a transmission electron microscope (TEM) (b) From left to right, TEM images of Au nanospheres, AR ~ 2.5 nanorods and AR ~ 4 nanorods (c) From left to right, TEM images of Au/SiO_2 nanospheres, AR ~ 2.5 and AR ~ 4 Au/SiO_2 core/shell nanorods

2.3.2 Optical Spectroscopy

As described in Section 2.1, the peak extinction wavelength of Au nanorods depends on the nanorod aspect ratio. In this section, the basics of optical spectroscopy are introduced. The effect of $AgNO_3$ and $C_6H_8O_6$ precursor concentration on Au nanorod aspect ratio using this technique are described.

Optical spectroscopy is an analytical technique that gives information about how a material interacts with light. The intensity of light passing through a sample (I) is compared to the intensity of light before it passes through the sample (I_o) over a range of wavelengths. The ratio I/I_o provides information about the spectral characteristics of electron energy transitions in the sample.

The basic parts of a spectrophotometer are a light source, a sample holder, a diffraction grating and a photodetector. In this study, the absorption spectrum is collected using a Shimadzu UV-3101PC with a measurement range between 190-3100 nm. The

system has two excitation sources, a tungsten lamp and a deuterium lamp. The tungsten lamp is the primary excitation source since measurements occur outside of the deuterium range (> 290 nm). Additionally, two types of detectors are used based on the measurement wavelength, with an InGaAs detector for wavelengths between 850-3100 nm and a Si detector for 290-850 nm. The probing energy is selected using a dual monochromator system with a resolution of 0.1nm. A schematic diagram of a UV-Vis absorption spectrometer is shown in Figure 2.18 (a) while sample absorption spectra of a colloidal solution of Au nanospheres, Au nanorods of aspect ratio 2.5 and Au nanorods of aspect ratio 4 are shown in Figure 2.18 (b).

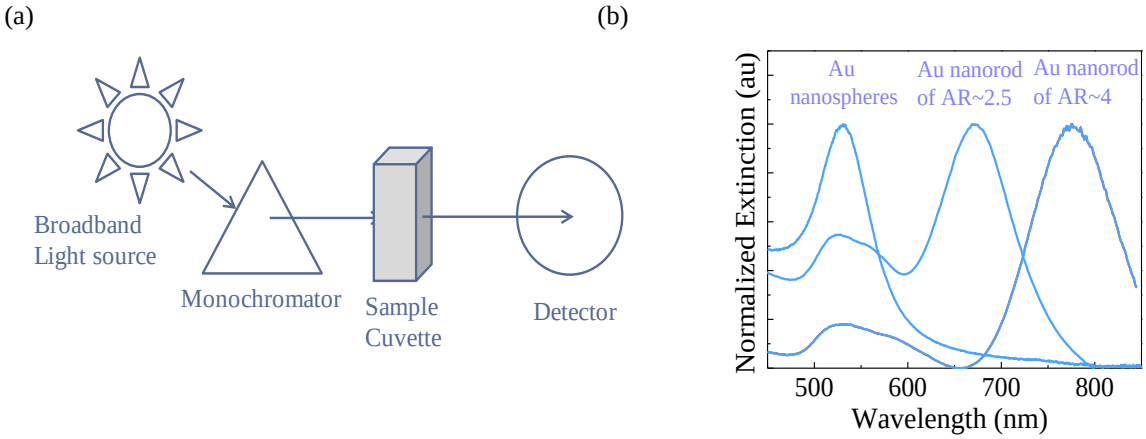


Figure 2.18 (a) Schematic diagram of a UV-Vis absorption spectrometer showing the main components of the system: a broadband light source (lamp), a monochromator, a sample cuvette and a photodetector (b) Extinction spectra of Au nanospheres (20 nm diameter), Au nanorods of aspect ratio ~ 2.5 (15 nm diameter, 37 nm length) and Au nanorods of aspect ratio ~4 (10 nm diameter, 40 nm length).

2.3.3 Photoluminescence Spectroscopy

Photoluminescence (PL) spectroscopy is a contactless, nondestructive method of probing the electronic structure of material. In PL spectroscopy, light directed onto a sample imparts energy onto the material and causes electrons within a material to move

into excited states. When these electrons return to their equilibrium states, the excess energy is released in radiative processes (light emission), or it is dissipated in nonradiative processes. In nonradiative relaxation, the energy is released as phonons. Nonradiative relaxation occurs when the energy difference between the levels is very small and typically occurs much faster than a radiative transition. Large nonradiative transitions do not occur frequently because the crystal structure generally cannot support large vibrations without destroying bonds. Meta-stable states form a very important feature that is exploited in the construction of lasers. Specifically, since electrons decay slowly from them, they can be populated at this state without too much loss and then stimulated emission can be used to increase an optical signal.

The energy of the emitted light is related to the difference in energy levels between the two electron states involved in the transition between the excited state and the equilibrium state, while the intensity of the emitted light is related to the relative contribution of the radiative process compared to nonradiative energy transitions. Sample excitation can be achieved with either a broadband, non-coherent light source like a lamp or a narrow band, coherent light source such as a laser. The excitation frequency can either be higher than the frequency of the emitted light in which case the PL is termed downconversion (since higher energy light is converted into lower energy light), or it can be lower than the emitted light, in which case the process is termed upconversion (since two or more photons of lower energy lead to the emission of a photon of higher energy). For theranostic applications, the upconverting properties of Au/SiO_2 and $Au/SiO_2/Yb:Er:Y_2O_3$ core/shell nanorods are of interest for reasons discussed in Section 1.4. The experimental setup used in this study is shown in Figure 2.19 (a). Light from a

fiber-coupled 980 nm laser diode (Sheaumann) was focused onto a sample. The upconverted light emitted from the sample passed through a 980nm optical filter to remove scattered excitation light and was then focused onto a monochromator (Orion Cornerstone 260) that separated the emitted light into its constituent wavelengths. A Si photodetector (SpectraPhysics S890) was used to measure the intensity of the upconverted light as a function of wavelength. A sample upconversion spectrum of Au/SiO_2 core/shell nanorod of aspect ratio ~ 4 is show in Figure 2.19 (b).

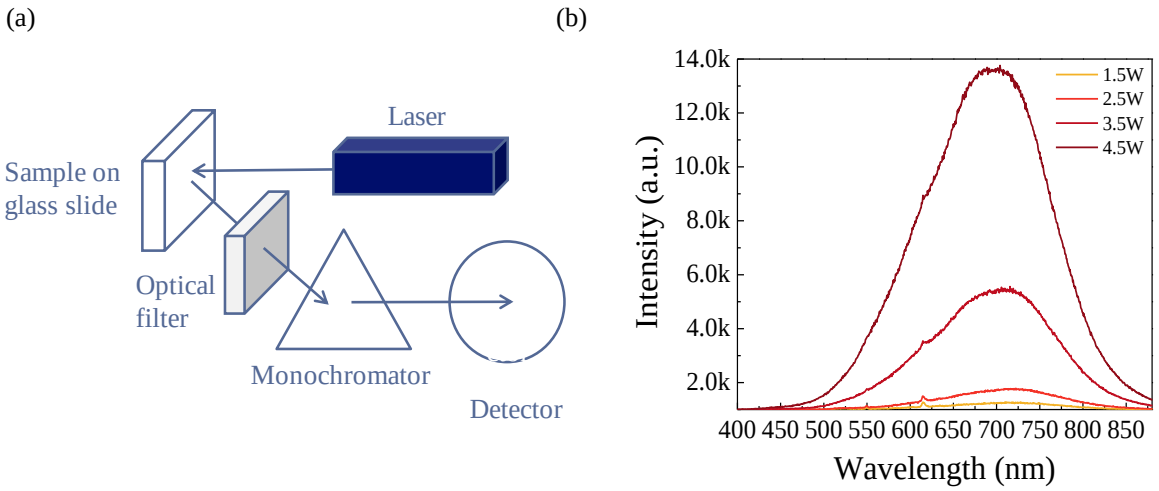


Figure 2.19 (a) Schematic diagram of an experimental setup used to measure upconversion photoluminescence (b) Upconversion spectra of Au/SiO_2 nanorods (15 nm diameter, 40 nm length, 5 nm SiO_2 shell thickness) as a function of excitation power.

2.3.4 Radiative Lifetime

The rate of light emission of a photo-excited species depends on the internal structure of the light emitter and the density of electromagnetic modes of the local environment around the emitter. Purcell showed that a high electromagnetic mode density increases the spontaneous emission rate of light emitters and this fact has been utilized to increase the brightness of emitter by placing them in resonant optical cavities, photonic

crystals or in the enhanced electromagnetic field that exists in the vicinity of plasmonic nanoparticles(1946; Rogobete 2007). This study compared the radiative liftetimes of Er^{3+} ions located in the near field of an Au nanorod (in which the emitter experiences an enhanced local electromagnetic field) with that of an Er^{3+} ion in an unperturbed electromagnetic environment.

Lifetime measurements were performed using a time-resolved fluorescence spectrometer (Edinburgh FLS920) with a nanosecond nitrogen filled flash-lamp, Czerny-Turner monochromator and a Si CCD detector. Radiative lifetimes were collected using the time correlated single photon counting (TCSPC) method with a 5000 photon minimum count. In TCSPC the sample is repetitively excited using a pulsed light source and the measurement builds a probability histogram relating the time between an excitation pulse and the observation of the first fluorescence photon. Samples were excited at 520 nm with a slit size of 5 nm and the lifetime emission was collected at 564 nm with 10 nm slits. Figure 2.20 (a) shows a simplified schematic of a TCPC experimental setup while Figure 2.20 (b) shows sample radiative lifetime measurements of SiO_2/Yb:Er:Y_2O_3 and Au/SiO_2/Yb:Er:Y_2O_3 core/shell nanoparticles.

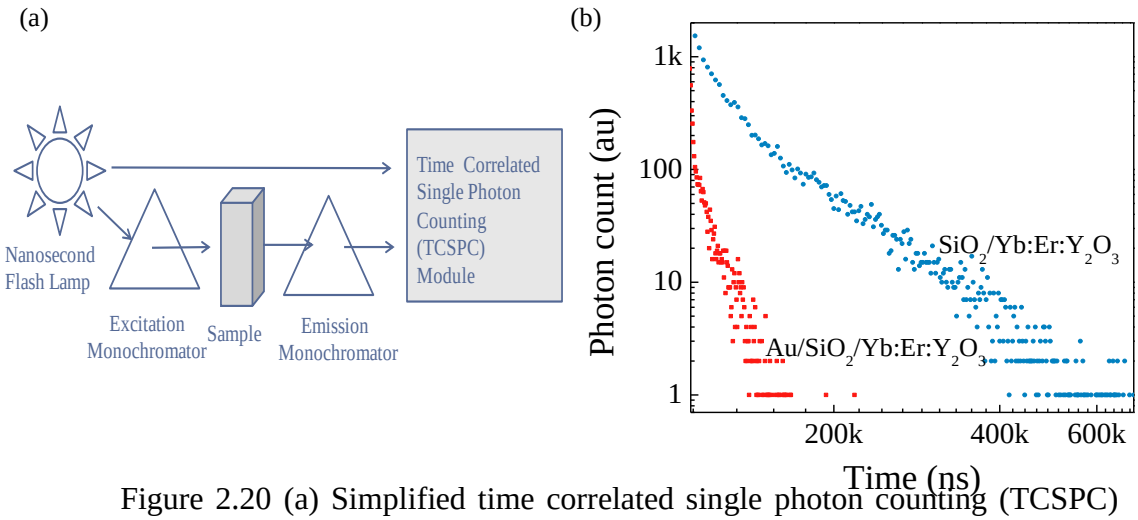


Figure 2.20 (a) Simplified time correlated single photon counting (TCSPC) experimental setup (b) Radiative lifetime measurements of SiO_2/Yb:Er:Y_2O_3 and Au/SiO_2/Yb:Er:Y_2O_3 core/shell nanoparticles.

2.3.5 External Quantum Efficiency

External quantum efficiency (EQE) measurements quantify the spectral response of a solar cell device by measuring device photocurrent as a function of wavelength. This work investigated the spectral response of organic photovoltaic (OPV) devices with and without plasmonic light trapping (PLT) Au/SiO_2 core/shell nanorods incorporated in the OPV device active layer. Figure 2.21(a) shows a schematic diagram of the EQE setup used in this work. Light from a 50W arc lamp was focused onto the entrance slit of an Orion Cornerstone 260 monochromator controlled with a USB port. A solar cell with its terminals connected to an optical power meter was attached to the exit slit of the mononchromator. EQE spectra were collected using Traq32 software. Figure 2.21 (b) shows a sample EQE spectra of a reference PBDTT-DPP.

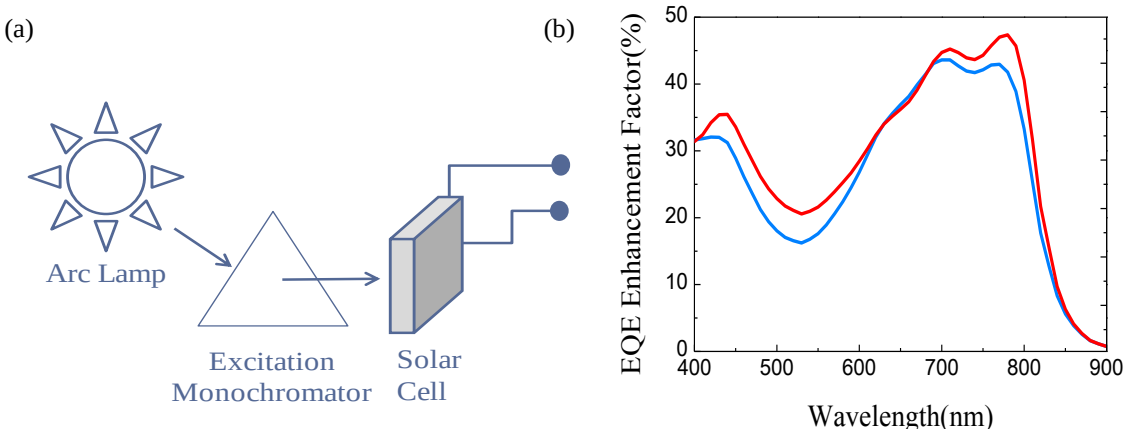


Figure 2.21 (a) Schematic diagram of an experimental setup used to measure photoluminescence; (b) Sample EQE spectrum of PBDTT-DPP:$PC_{60}BM$ and PBDTT-DPP:$PC_{60}BM$ with Au/SiO_2 core/shell nanorods embedded in the active layer.

2.3.6 Photo-thermal Energy Conversion Efficiency

Optical energy absorbed by a material that is not released as light is generally converted into heat in a photo-thermal transduction process. The efficiency of photo-thermal energy conversion of the sample depends on the absorption cross section of the colloidal nanoparticles, their concentration and the photo-thermal transduction efficiency (Chen 2010). For *ex vitro* experiments, Au nanorod solutions were irradiated by the 980-nm laser at 1 W/cm^2. Temperature was measured with a thermocouple placed inside the solution for a total of 6 min. The thermocouple was placed outside the path of the laser beam to avoid direct exposure of the thermocouple to the laser light. The photo-thermal energy conversion efficiency of Au/PVP, Au/SiO_2 and Au/SiO_2/Yb:Er:Y_2O_3 core/shell nanorods were measured using the experimental setup shown in Figure 2.22 (a) while sample heating and cooling curves for 3 different concentrations of Au/PVP colloidal solutions is shown in Figure 2.22 (b)

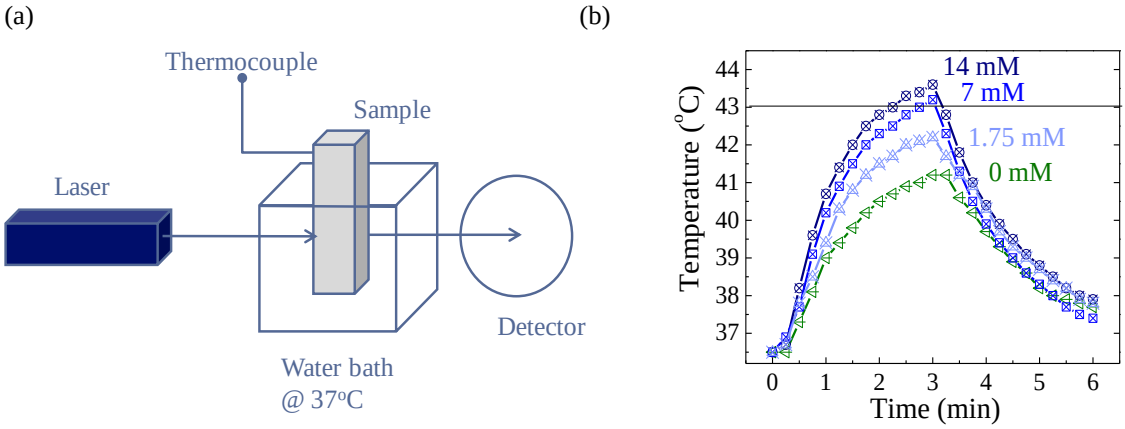


Figure 2.22 (a) Experimental setup used to measure photothermal energy conversion of Au, Au/SiO_2 and Au/SiO_2/Yb:Er:Y_2O_3 nanorods; (b) Photothermal heating rates of 400µl colloidal solutions of 14 mM, 7 mM, 1.75 mM Au/PVP nanorods and a control (H_2O).

CHAPTER 3 PLASMONIC LIGHT TRAPPING WITH Au/SiO_2 CORE/SHELL NANORODS

An increase in the short circuit current density (J_{sc}) and photon conversion efficiency (PCE) of two organic photovoltaic (OPV) polymer systems was demonstrated by incorporating octadecyltrimethoxysilane (OTMS)-functionalized Au/SiO_2 core/shell nanospheres and nanorods into their active layers. A SiO_2 shell layer was added onto the Au core nanospheres and nanorods to provide an electrically insulating surface that did not interfere with carrier generation and transport inside the active layer. Functionalization of the Au/SiO_2 core/shell nanoparticles with the OTMS organic ligand was necessary to transfer the nanoparticles into an OPV polymer-compatible solvent such as dichlorobenzene (DCB). The two polymer systems were poly(3-hexylthiophene):[6,6]-phenyl-C61-butyric acid methyl ester and poly[2,6-4,8-di(5-ethylhexylthienyl)benzo[1,2-b;3,4-b]dithiophene-alt-5-dibutyloctyl-3,6-bis(5-bromothiophen-2-yl) pyrrolo[3,4-c]pyrrole-1,4-dione], abbreviated as P3HT:$PCB_{60}M$ and PBDTT-DPP:$PC_{60}BM$, respectively. For the P3HT:$PC_{60}BM$ polymer with a band edge of ~ 670 nm, the addition of the core/shell nanorods with the corresponding extinction peak (AR ~ 2.5) resulted in a 7.1 % improvement in PCE, while for the PBDTT-DPP:$PC_{60}BM$ polymer with a band edge ~ 830 nm, the addition of core/shell nanorods of AR ~ 4 (extinction peak, λ_{peak} = 830 nm) resulted in a 14.4% improvement in PCE. The addition of Au/SiO_2 core/shell nanospheres to the P3HT:$PC_{60}BM$ and PBDTT-DPP:$PC_{60}BM$ polymers resulted in 2.7 % and 9.1 % improvement in PCE, respectively. The PCE and J_{sc} enhancements were consistent with the measured EQE enhancements.

3.1 Au/SiO_2 Core/Shell Nanoparticle Synthesis

The synthesis of Au nanospheres was achieved by reducing Au chloride ($HAuCl_4$) with sodium borohydride ($NaBH_4$) in the presence of a surfactant (cetyltrimethylammoniumbromide (CTAB)). To prepare 10.6 ml of Au nanospheres, 5 ml of a 0.5 mM $HAuCl_4$ solution were mixed with 5 ml of a 0.2M CTAB solution, followed by the addition of 0.6 ml of ice cold $NaBH_4$ to initiate the reaction. The protocol produces 2-5 nm diameter nanospheres which increased in size over a few days to be ~20 nm in diameter. The synthesis of Au nanorods required the preparation of two solutions: a seed solution and a growth solution. The seed solution was prepared by mixing 5 ml of 0.5 mM $HAuCl_4$, 5 ml of 0.2 M CTAB and 0.6 ml of 0.1M ice cold $NaBH_4$. A solution of Au nanorods with an aspect ratio of 2.5 was prepared using a growth solution that contained 0.6 ml of 0.01M $AgNO_3$, 20 ml of 0.5 mM $HAuCl_4$, 20 ml of 0.2 M CTAB and 0.7 ml of 0.77 M ascorbic acid. To prepare nanorods with an aspect ratio of 4, 0.9 ml of 0.01 M $AgNO_3$ was used instead of 0.6 ml of 0.01 M $AgNO_3$ in the growth solution. The growth process was initiated by injecting 26 μl of seed solution into the growth solution at a temperature of 27^oC. The reaction took approximately two hours to complete.

To coat the Au nanorods with SiO_2, experimental procedures outlined in Chapter 2 were followed. The nanorods were first rendered vitreophillic by treating them with consecutive polyelectrolyte layers. Au metal has little affinity for SiO_2 because, unlike most other metals, it does not form a passivating oxide film in solution. Furthermore, the stabilizing surfactant, CTAB, interferes with the SiO_2 coating process. In order to replace the CTAB stabilizer and modify the gold nanorod surface chemistry, consecutive polyelectrolyte layers were adsorbed onto the metal surface. This process proceeded in

the following manner: first, the as-synthesized, CTAB-stabilized Au nanorods were centrifuged, the precipitate was redissolved in 3 ml of distilled water. It was then added to 3 ml of an aqueous solution containing poly-styrene sulfonate (PSS) (2 mg/mL and 6 mM NaCl) and stirred for approximately three hours. The PSS-modified particles were centrifuged twice to remove any excess PSS and redispersed in 3 ml of deionized water. The colloid was then added drop-wise under vigorous stirring to 3 ml of an aqueous solution of 2 mg/ml poly(anilline hydrochloride) (PAH) and 6 mM NaCl). PAH adsorption was allowed to proceed for three hours. The sample was then centrifuged to remove excess polyelectrolyte and redispersed in 3 mL of deionized water. 3 ml of the PSS/PAH functionalized Au spheres were added to a polyvinylpyrrolidone (PVP) solution (4 mg/ml). The mixture was stirred for approximately twelve hours, centrifuged to remove any excess polymer, and redispersed in 0.2 mL of deionized water. This aqueous dispersion of PVP-coated nanoparticles was then added drop-wise and under vigorous stirring to 2 mL of isopropyl-alcohol (IPA). Once the Au nanoparticles were transferred into IPA without agglomeration, SiO_2 coating was carried out through the adjustment of the pH and addition of tertra-ethyl-orthosilicate (TEOS). The pH was adjusted to 10 by adding 1.5 ml, 4 vol% NH_3 in IPA (27% in water). Finally, 0.4 ml of TEOS (1 vol% in ethanol) was added under gentle stirring and the reaction was allowed to proceed for approximately twelve hours. In order to dissolve the Au/SiO_2 core/shell nanorods in an OPV-compatible solvent, like dichlorobenzene, functionalization with octadecyltrimethoxysilane (OTMS) was performed. The Au/SiO_2 core/shell nanorods were centrifuged and redissolved in 3 ml of ethanol containing 30 μl of NH_4OH (32%). 300 μl of OTMS chloroform solution (3%) was added drop-wise with vigorous stirring

and functionalization of the SiO_2 surface was achieved by hydrolysis of the methoxy groups and condensation of the resulting silane groups with SiOH groups on the SiO_2 surface. Transmission electron microscopy (TEM) using an FEI TF20 was used to confirm the morphology of the synthesized Au/SiO_2 core/shell nanorods, while UV-Vis spectroscopy was used to determine the extinction spectra of the nanorod solutions.

3.2 Plasmonic Organic Photovoltaic Device Fabrication

All the devices had the same structure: indium tin oxide (ITO)/ poly(ethylenedioxythiophene):polystyrenesulphonate (PEDOT:PSS)/active layer/calcium (Ca)/aluminum (Al). The PEDOT:PSS was pre-coated onto the ITO substrate and baked at 120^{o}C for 15 minutes before spin-casting the solutions. The P3HT:PC_{60}BM-based devices were spin-coated at 800 rpm for 40 seconds after which the wet films remained in the petri dishes until they dried (the color of the films changed from orange to dark-red). This solvent annealing process has been demonstrated to attain an optimized morphology for P3HT:PC_{60}BM-based organic solar cell devices. The PBDTT-DPP:PC_{60}BM-based devices were fabricated by spin-casting at 1800 rpm for 80 seconds with no other treatment. A bilayer cathode containing a Ca layer (20 nm) and a subsequent Al layer (100 nm) were deposited by thermal evaporation under high vacuum (<3×10^{-6} Torr). The active layer thickness of the P3HT:PC_{60}BM-based devices was ~210 nm while the thickness of the PBDTT-DPP:PC_{60}BM-based devices was ~ 90 nm. Polymer reference solutions consisted of 20 mg/mL of P3HT:PC_{60}BM (1:1 weight ratio) and 6 mg/mL PBDTT-DPP:PC_{60}BM (1:2.5 weight ratio). The plasmonic P3HT:PC_{60}BM solar cell device solution was prepared by adding a solution of the OTMS-functionalized Au/SiO_2

core/shell nanorods (AR~2.5) to the P3HT:$PC_{60}BM$ solution so that the final concentration of the nanorods was 0.6 mg/mL. The plasmonic PBDTT-DPP:$PC_{60}BM$ solar cell device solution was prepared by mixing the OTMS-functionalized Au/SiO_2 core/shell nanorod solution (AR ~ 4) with the PBDTT-DPP:$PC_{60}BM$ solution so that the final concentration of Au/SiO_2 core/shell nanorods was 0.2 mg/mL.

3.3 Plasmonic Organic Photovoltaic Device Characterization

In order to study the viability of this approach, Au/SiO_2 core/shell nanospheres and nanorods were incorporated into the active layers of two polymer OPV systems: P3HT:$PC_{60}BM$ and PBDTT-DPP:$PC_{60}BM$. The greatest enhancement due to the LSPR near field was expected to occur in spectral regions where the OPV polymer absorbs poorly, while the lowest enhancement where the OPV polymer absorbs efficiently. To investigate this hypothesis, EQE measurements on OPV devices with spectrally-tuned Au/SiO_2 nanoparticles were performed. For the P3HT:$PC_{60}BM$ system, Au/SiO_2 nanospheres with a peak extinction of ~540 nm (matching a spectral region of high polymer absorption) and Au/SiO_2 nanorods (AR~2.5) with a peak extinction of ~670 nm (matching the band edge of the P3HT:$PC_{60}BM$) were synthesized. For the PBDTT-DPP:$PC_{60}BM$ system, Au/SiO_2 nanospheres with a peak extinction of ~540 nm (matching a spectral region of moderate polymer absorption) and Au/SiO_2 nanorods (AR~4) with a peak extinction of ~830 nm (matching the OPV polymer band edge) were synthesized. The SiO_2 shell thickness in all samples was ~10 nm. Short-circuit current density (J_{sc}), open-circuit voltage (V_{oc}), and external quantum efficiency (EQE) measurements were performed on the devices. Blending the Au/SiO_2 nanospheres and nanorods into the

active layer resulted in enhanced J_{sc} and PCE in both the P3HT:PC_{60}BM and PBDTT-DPP:PC_{60}BM devices compared to the reference device. Figure 3.1 (a) shows the transmission electron microscopy (TEM) images of: Au nanospheres in water, Au nanorods of AR~2.5 in water, Au nanorods of AR~4 in water, Au/SiO_2 core/shell nanospheres in DCB, Au/SiO_2 nanorods of AR ~2.5 in DCB, Au/SiO_2 nanorods of AR~4 in DCB, while Figure 3.1 (b) shows the corresponding extinction spectra. Figure 3.1 (c) shows normalized extinction spectra of solutions D and E with a normalized EQE spectrum of P3HT:PC_{60}BM, while Figure 3.1(d) shows a normalized EQE spectrum of PBDTT-DPP:PC_{60}BM with normalized extinction spectra of solutions D and F. Figures 3.1(e) and 3.1(f) show the EQE spectra of the reference and plasmonic OPV device based on P3HT:PC_{60}BM and PBDTT-DPP:PC_{60}BM, respectively.

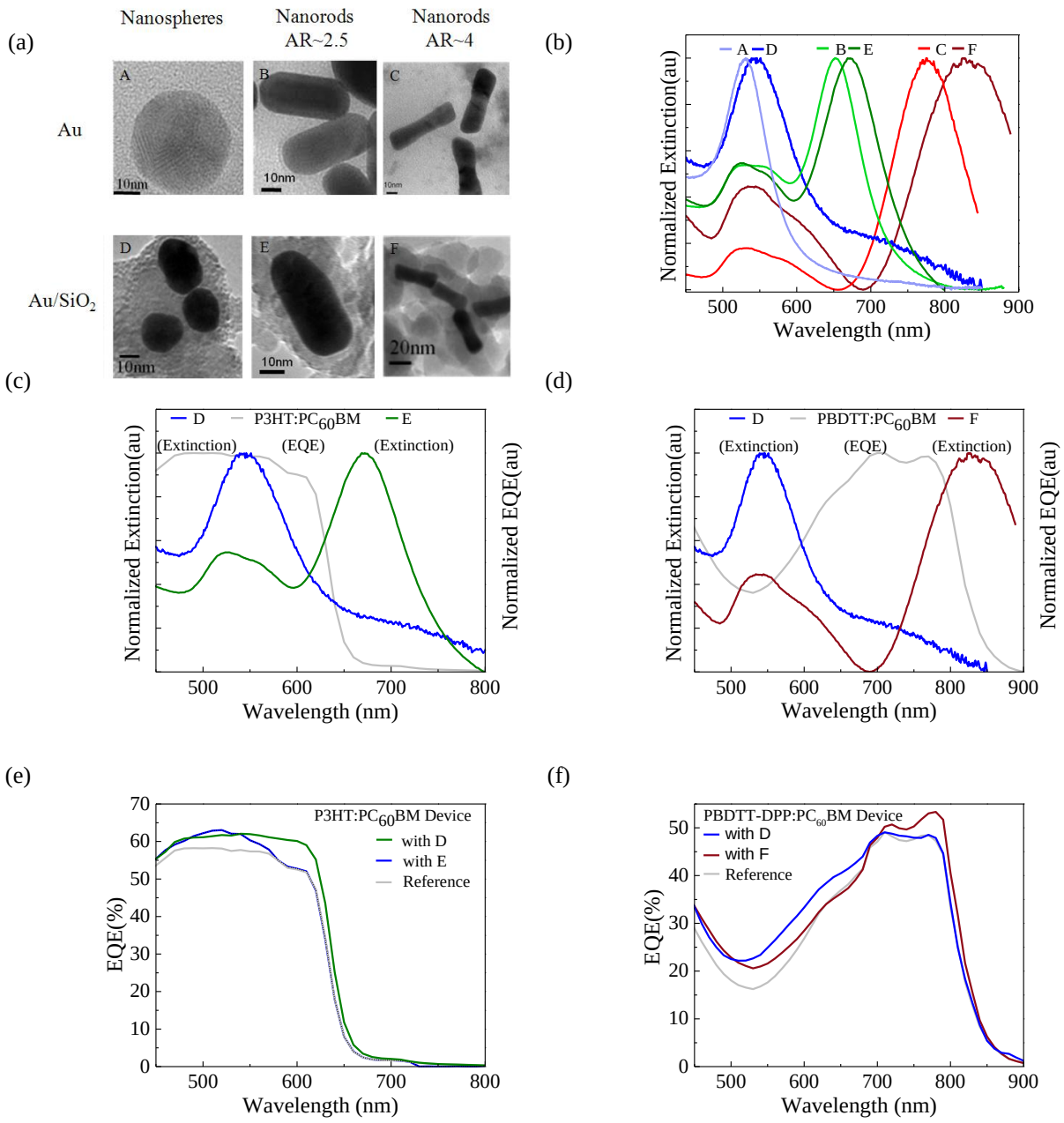


Figure 3.1 (a) TEM images and (b) Extinction spectra of various colloidal solutions: (A) Au nanospheres in water (B) Au nanorods of AR~2.5 in water (C) Au nanorods of AR~4 in water (D) Au/SiO_2 core/shell nanospheres in DCB (E) Au/SiO_2 nanorods of AR ~2.5 in DCB (F) Au/SiO_2 nanorods of AR ~4 in DCB; (c) EQE of P3HT:PC_{60}BM plotted with normalized extinction spectra from solutions D and E; (d) EQE of PBDTT-DPP:PC_{60}BM devices plotted with normalized extinction spectra from solutions D and F; (e) EQE from (e) P3HT:PC_{60}BM with solutions D, E and reference (f) PBDTT-DPP:PC_{60}BM with solutions D, F and reference.

To assess the EQE enhancement quantitatively, a spectral EQE enhancement percentage is defined as:

$$\frac{\Delta EQE}{EQE_{ref}}(\%) = \frac{EQE_{plasmonic}(\lambda) - EQE_{reference}(\lambda)}{EQE_{reference}(\lambda)} \cdot 100 \qquad (3.1)$$

Figure 3.2 shows EQE enhancement factors ($\Delta EQE/EQE_{ref}$) of OPV plasmonic devices compared to reference devices, plotted with the extinction spectra of Au/SiO_2 nanosphere and nanorod colloidal solutions embedded in their active layers.

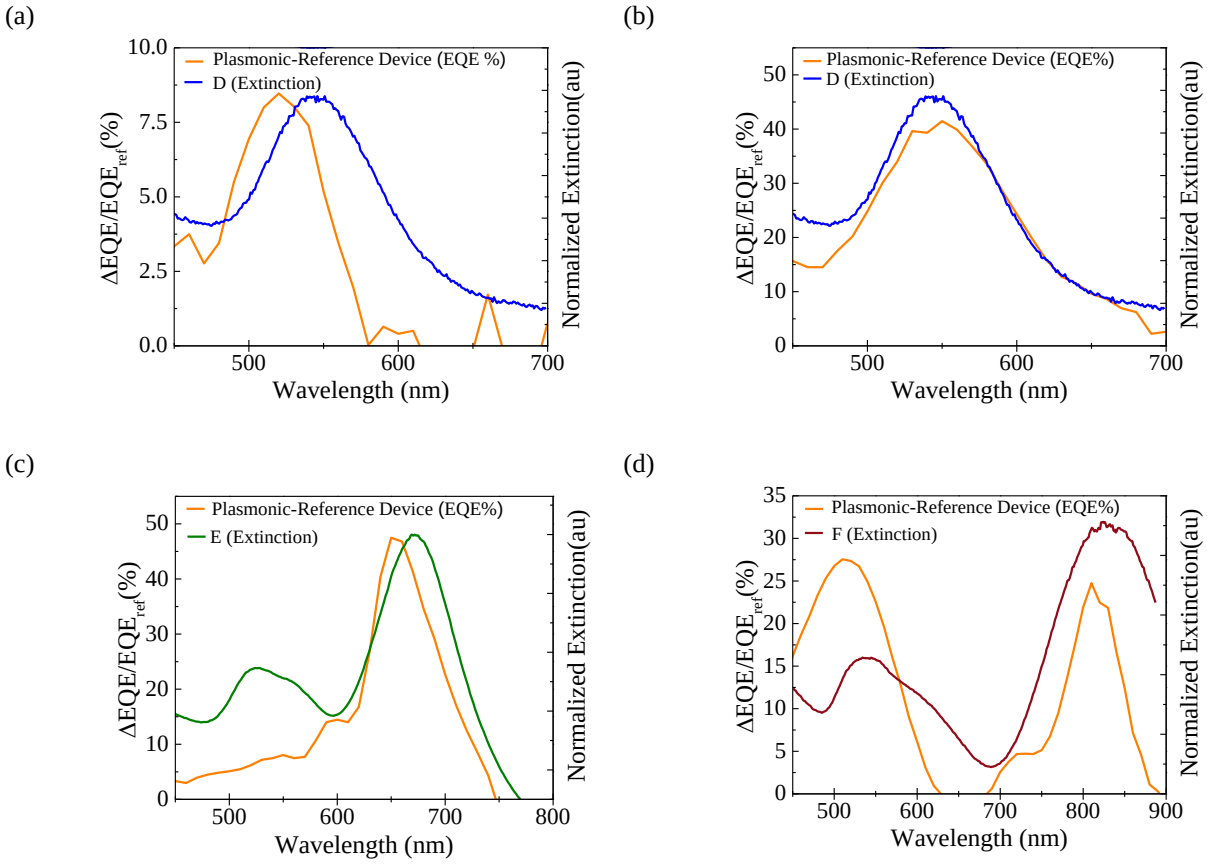


Figure 3.2 Spectral EQE enhancements of (a) P3HT-based device with Au/SiO_2 nanospheres (solution D) (b) PBDTT-DPP-based device with solution Au/SiO_2 nanospheres (solution D) (c) P3HT-based device with AR~2.5 Au/SiO_2 core/shell nanorods (solution E) (d) PBDTT-DPP-based device with AR~4 Au/SiO_2 core/shell nanorods (solution F)

EQE enhancements in both polymer systems spectrally matched the extinction spectra of the active layer-incorporated Au/SiO_2 core/shell nanospheres and nanorods. Au/SiO_2 core/shell nanorods of AR~4 incoporated into the active layer of the PBDTT-DPP:$PC_{60}BM$ system showed the highest EQE enhancement factors, while Au/SiO_2 nanospheres incorporated in the active layer of the P3HT:$PC_{60}BM$ system showed the lowest performance enhancement. In the low band gap polymer system, PBDTT-DPP:$PC_{60}BM$, the improvement was in two spectral regions matching both the longitudinal and the transverse oscillation modes of the Au/SiO_2 nanorods.

A concentration study of the Au/SiO_2 nanorod additive on the performance of the OPV devices was also conducted and revealed that OPV device performance depended on the amount of Au/SiO_2 core/shell nanospheres or nanorods incorporated into the active layer. Increasing the amount of Au/SiO_2 nanoparticles led to an initial increase in solar cell PCE. As the Au/SiO_2 concentration increased, however, a decrease in device performance was observed. For the P3HT:$PC_{60}BM$ system, the optimal Au/SiO_2 nanosphere concentration was 0.4 mg/ml and 0.6 mg/ml for the Au/SiO_2 nanorods; concentrations of nanospheres or nanorods greater than 2 mg/ml resulted in OPV device performance degradation. Similarly, optimal concentrations for the PBDTT-DPP:$PC_{60}BM$ system were 0.1 mg/ml for nanospheres and 0.2 mg/ml for nanorods (AR ~ 4) with a threshold concentration of 1 mg/ml. The results of the concentration study are summarized in Tables 3.1-3.4 and in Figure 3.3.

Table 3.1 Gold/Silica Core/Shell Nanospheres (radius=20 nm) in P3HT:$PC_{60}BM$

Devices	$J_{sc}(mA/cm^2)$	$V_{oc}(V)$	FF(%)	PCE(%)
Without Au/SiO_2	8.98±0.06	0.61±0.01	68.0±0.6	3.67±0.05
0.2mg/mL Au/SiO_2	9.20±0.05	0.60±0.00	67.9±0.6	3.73±0.03
0.4mg/mL Au/SiO_2	9.41±0.05	0.59±0.00	67.8±0.2	3.77±0.03
0.8mg/mL Au/SiO_2	9.30±0.15	0.59±0.00	65.5±1.1	3.61±0.09
1.5mg/mL Au/SiO_2	8.50±0.25	0.58±0.01	54.8±1.2	2.67±0.14

Table 3.2 Gold/Silica Core/Shell Nanospheres (radius=20 nm) in PBDTT-DPP:$PC_{60}BM$

Devices	$J_{sc}(mA/cm^2)$	$V_{oc}(V)$	FF(%)	PCE(%)
Without Au/SiO_2	10.35±0.14	0.75±0.00	63.7±0.5	4.93±0.09
0.1mg/mL Au/SiO_2	11.81±0.08	0.74±0.01	61.0±0.3	5.38±0.06
0.2mg/mL Au/SiO_2	11.36±0.05	0.75±0.01	59.1±0.5	5.02±0.05
0.4mg/mL Au/SiO_2	11.60±0.11	0.74±0.01	58.2±0.4	5.03±0.04
1.0mg/mL Au/SiO_2	11.33±0.15	0.74±0.01	57.1±0.8	4.84±0.04

Table 3.3 Gold/Silica Core/Shell Nanorods of AR~2.5 (radius=10 nm) in P3HT:$PC_{60}BM$

Devices	$J_{sc}(mA/cm^2)$	$V_{oc}(V)$	FF(%)	PCE(%)
Without Au/SiO_2	8.98±0.06	0.61±0.01	68.0±0.6	3.67±0.05
0.2mg/mL Au/SiO_2	9.15±0.05	0.61±0.01	67.9±0.5	3.76±0.02
0.6mg/mL Au/SiO_2	9.80±0.04	0.60±0.00	66.9±0.2	3.93±0.03
1.5mg/mL Au/SiO_2	9.61±0.04	0.60±0.00	66.0±0.5	3.79±0.06
3.0mg/mL Au/SiO_2	8.81±0.09	0.60±0.00	58.8±1.2	3.11±0.09

Table 3.4 Gold/Silica Core/Shell Nanorods of AR~4 (radius=8 nm) in PBDTT-DPP:$PC_{60}BM$

Devices	$J_{sc}(mA/cm^2)$	$V_{oc}(V)$	FF(%)	PCE(%)
Without Au/SiO_2	10.35±0.14	0.75±0.00	63.7±0.5	4.93±0.09
0.1mg/mL Au/SiO_2	11.41±0.09	0.75±0.00	63.0±0.6	5.36±0.07
0.2mg/mL Au/SiO_2	12.20±0.15	0.75±0.00	61.6±0.4	5.64±0.05
0.4mg/mL Au/SiO_2	12.35±0.25	0.74±0.01	60.4±1.5	5.48±0.10
1.0mg/mL Au/SiO_2	11.60±0.20	0.72±0.01	52.5±2.5	4.27±0.19

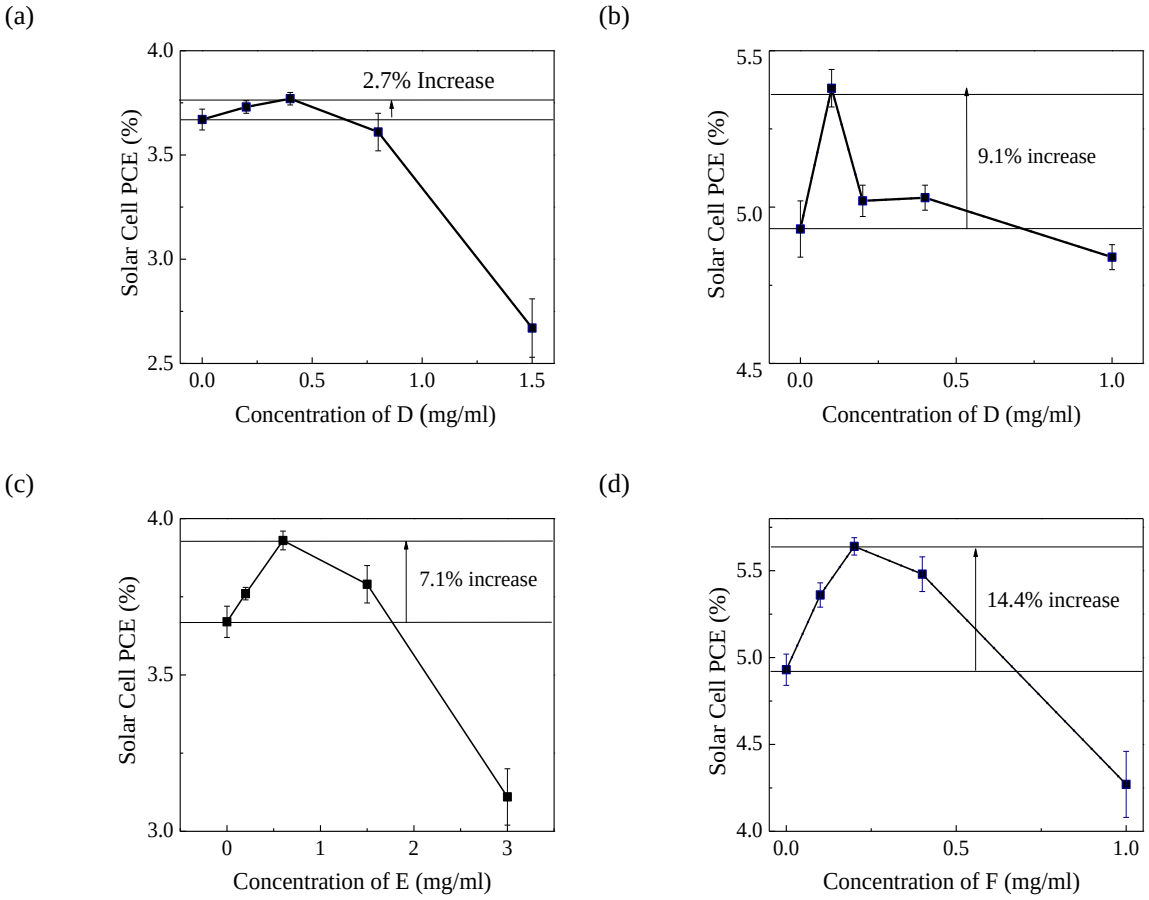


Figure 3.3 Solar cell PCE as a function of Au/SiO_2 nanosphere and nanorod concentrations for (a) D in P3HT:$PC_{60}BM$ (b) D in PBDTT-DPP:$PC_{60}BM$ (c) E in P3HT:$PC_{60}BM$ and (d) F in PBDTT-DPP:$PC_{60}BM$.

The reason for the observed trends may be attributed to disruption of the OPV cell morphology due to a high concentration of Au/SiO_2 core/shell additive, leading to lower carrier extraction. The lower optimal concentration of Au/SiO_2 nanospheres compared to nanorods was attributed to the fact that the Au/SiO_2 sphere colloidal solutions were dispersed less uniformly and contained aggregates, disrupting the OPV cell morphology to a greater extent. In order to investigate this further, atomic force microscopy (AFM) studies were conducted using a Bruker Dimension 5000 Scanning Probe Microscope (SPM) in "tapping" mode to examine the surfaces of the OPV cells with Au/SiO_2

core/shell nanospheres that yielded the highest and lowest PCEs along with reference devices for both the P3HT- and PBDTT-DPP-based OPV devices. The best plasmonic OPV devices show similar height and phase images as the reference devices, indicating a relatively unchanged morphology in the bulk heterojunction. On the other hand, the plasmonic OPV devices with higher Au nanorods loading show increased roughness as well as some abrupt protrusions on the surface, which might be the aggregations of the Au/SiO_2 nanoparticles. Figures 3.4 and 3.5 show AFM images of the reference, optimum and highest tested Au/SiO_2 nanosphere concentrations for the P3HT- and the PBDTT-DPP-based devices, respectively. The BHJ morphology evolution with different amounts of Au/SiO_2 nanoparticles is a critical factor affecting the overall device performance, *e.g.* the Au/SiO_2 nanoparticles might alter the crystallinity, molecular packing and donor/acceptor interface.

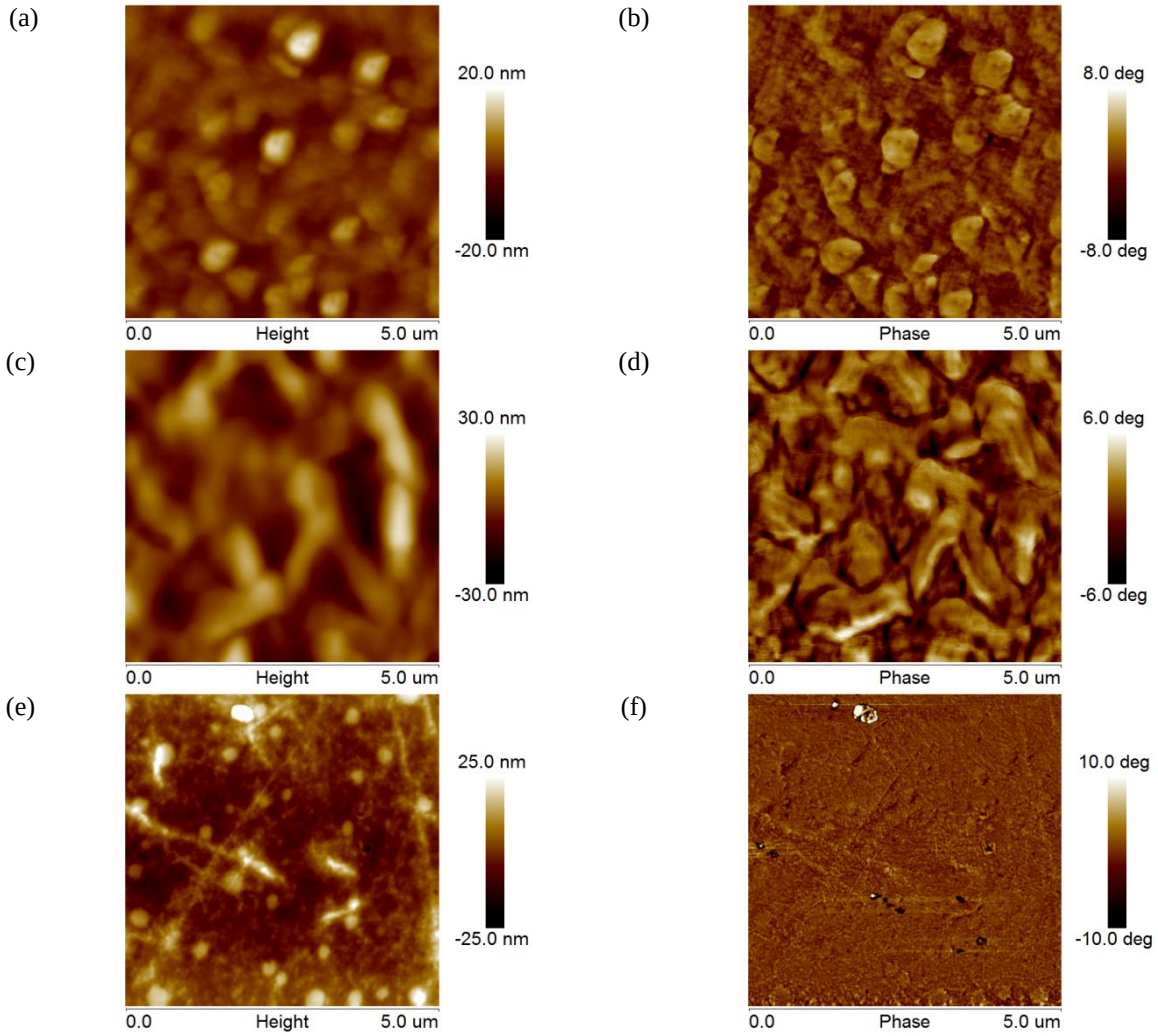


Figure 3.4 Atomic force microscopy images of P3HT:$PCB_{60}M$ devices (the left column is the height image and the right column the phase image): (a-b) Reference device, (c-d) Device with 0.6 mg/ml Au/SiO_2 nanospheres, and (e-f) Device with 3 mg/ml Au/SiO_2 nanospheres.

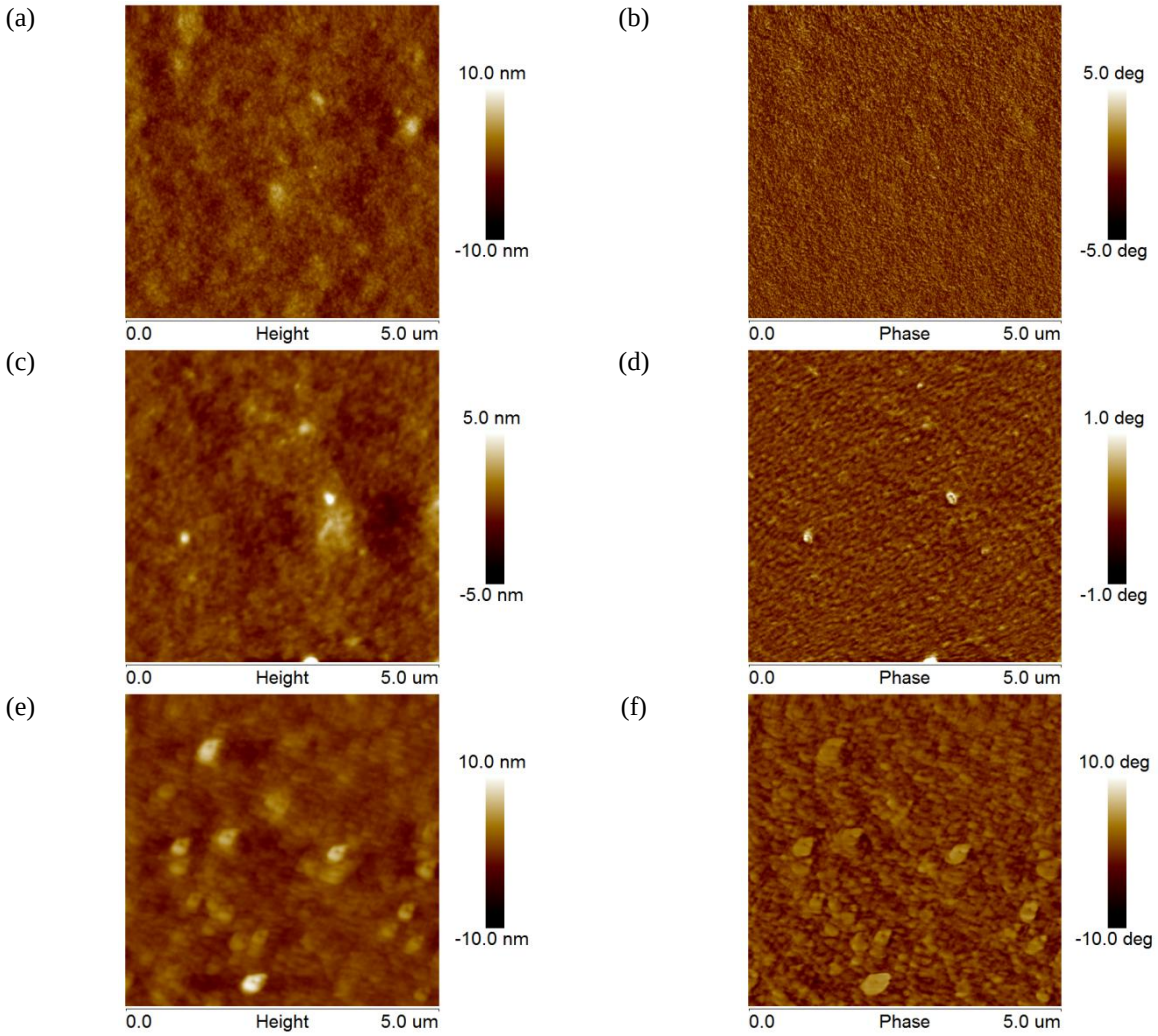


Figure 3.5 Atomic force microscopy image of PBDTT-DPP:$PCB_{60}M$ devices (the left column is the height image and the right column the phase image): (a-b) Reference device, (c-d) Device with 0.6 mg/ml Au/SiO_2 nanospheres, and (e-f) Device with 1 mg/ml Au/SiO_2 nanospheres.

For the P3HT:$PC_{60}BM$ system, the J_{sc} was improved by 8% while for the PBDTT-DPP:$PC_{60}BM$ system, the improvement was 16%. The V_{oc} were nearly the same for both systems, while the fill factor (FF) decreased 1.1% for the P3HT:$PC_{60}BM$ system and 2.6% for PBDTT-DPP:$PC_{60}BM$ system. This may be attributed to the fact that the

morphology of the device was altered after the incorporation of the Au/SiO_2 nanorods,. Further study is required to elucidate the mechanisms responsible for the observed trends.

In the low band gap polymer system, PBDTT-DPP:$PC_{60}BM$, a larger enhancement was observed than that in the P3HT:$PC_{60}BM$ system. From the EQE enhancement factor, it was found that the improvement was in two spectral regions: one ~ 830 nm that matched the longitudinal oscillation mode of the Au/SiO_2 nanorods, and another one at ~540 nm that matched the transverse oscillation mode. Variation of the active layer thickness and other processing variations were excluded since the shape of the EQE spectrum after adding Au/SiO_2 nanorods strongly differs from that of the reference device.

In conclusion, improvements in the PCE and J_{sc} were achieved in two OPV polymer systems by incorporating resonant light absorption and scattering Au/SiO_2 core/shell nanorods in their active regions. For the P3HT:$PC_{60}BM$, the incorporation of Au/SiO_2 core/shell nanospheres (~ 540 nm peak extinction) in the active layer led to a 1.9% increase in PCE. The incorporation of Au/SiO_2 nanorods with peak extinction wavelengths matched to the P3HT:$PC_{60}BM$ polymer band edge ~ 670 nm led to a 6.2% increase in the PCE of OPV devices. For the PBDTT:$PC_{60}BM$ system, the incorporation of Au/SiO_2 nanospheres with peak extinction wavelengths ~ 540 nm led to a 8.2% increase in PCE while Au/SiO_2 core/shell nanorods with extinction peaks matched to the band edge of PBDTT-DPP:$PC_{60}BM$ (~ 830 nm) showed a PCE increase of 13.3%. The results indicate that spectral tuning of the active layer plasmonic light trapping particles is a key consideration for active layer incorporated plasmonic light trapping. In order to maximize light trapping in practical applications, active layer-incorporated Au/SiO_2

nanoparticles should be spectrally tuned to match wavelength regions of poor light absorption. In spectral regions where the OPV polymer absorbs light efficiently, the effect of incorporating plasmonic light trapping nanoparticles is small.

These results also indicate that the concentration of the active layer- incorporated Au/SiO_2 core/shell nanoparticles needs to be optimized. After a certain critical concentration, the addition of core/shell nanoparticles degrades device performance. A high concentration of Au/SiO_2 core/shell particles in the active layer causes disruption of the OPV polymer morphology and leads to lower carrier extraction.

Au/SiO_2 core/shell nanorods may have utility as a flexible vehicle to study plasmonic light trapping in OPVs. The relative absorption or scattering contribution to the overall nanoparticle optical response can be designed by changing the size of Au nanosphere or nanorod core (Wang 2011). By increasing the SiO_2 shell thickness to > 15 nm, the near field enhancement from the LSPR is concentrated entirely in the SiO_2 shell and any observed EQE enhancement is derived from light scattering off of the nanoparticle. An ultra-thin layer of SiO_2 (< 2 nm) on the other hand ensure that the nanoparticles remain electrically insulating but that OPV material at the edge of the nanoparticle still experience an enhanced near field.

CHAPTER 4 PLASMONIC PHOTOTHERMAL THERAPY WITH $Au/SiO_2/Yb:Er:Y_2O_3$ NANORODS

Spectrally-tailored gold/silica/ytterbium, erbium co-doped yttria core/shell nanorods ($Au/SiO_2/Yb:Er:Y_2O_3$) were investigated for dual-mode bio-imaging and photo-thermal therapy applications in terms of their cytotoxic, photo-thermal and optical properties. The peak extinction wavelength of the $Au/SiO_2/Yb:Er:Y_2O_3$ core/shell nanorod was spectrally matched to the peak emission wavelength of the Er^{3+} ion $^4F_{9/2}\rightarrow{}^4I_{15/2}$ energy transition (660 nm) in order to increase the photonic density of states at that frequency and thus enhance the photo-luminescence (PL) intensity of the Er^{3+} ion. The Er^{3+} $^4F_{9/2}\rightarrow{}^4I_{15/2}$ transition was specifically chosen from four available Er^{3+} emission bands in the UV-visible regime (405 nm ($^2H_{9/2}\rightarrow{}^4I_{15/2}$), 520 nm ($^2H_{11/2}\rightarrow{}^4I_{15/2}$), 550 nm ($^4S_{3/2}\rightarrow{}^4I_{15/2}$) and 660 nm ($^4F_{9/2}\rightarrow{}^4I_{15/2}$)) because it falls within the biologically transparent window (~ 630 nm to ~ 930 nm).

The cell survival rate of MDA MB 231 breast cancer cells incubated with 7 mM Au/SiO_2 and $Au/SiO_2/Yb:Er:Y_2O_3$ core/shell nanorod colloidal solutions was quantified and compared to the cell survival rate of breast cancer cells incubated with 7 mM Au/PSS, Au/PAH and Au/PVP nanorod colloidal solutions. The cell survival rates of MDA MB 231 cells incubated with 7 mM Au/SiO_2 and $Au/SiO_2/Yb:Er:Y_2O_3$ core/shell nanorods were 68% and 83%, respectively, lower than those of cells incubated with 7 mM Au/PSS, Au/PAH, Au/PVP (> 90%). Cells embedded with Au/SiO_2 core/shell nanorods showed the lowest cell survival rate, possibly due to the fact that the surface of SiO_2 nanoparticles produces reactive oxygen species through disproportionated reaction

resulting in oxidative damage to protein and DNA. The cytotoxicity of $Au/SiO_2/Yb:Er:Y_2O_3$ nanoparticles occurs due to a similar reaction.

In-vitro studies of MDA MB 231 cells tumor cells exposed with 980 nm laser irradiation demonstrated that selective hyperthermia can be induced using 7mM Au/PAH, Au/PVP, Au/SiO_2 or $Au/SiO_2/Yb:Er:Y_2O_3$ nanorods. When irradiated with a 980 nm laser diode for 5 min at 1.7 W/cm^2, the cell survival rates of MDA MB 231 cells incubated with 7 mM Au/SiO_2 and $Au/SiO_2/Yb:Er:Y_2O_3$ core/shell nanorods were reduced 19% and 18%, respectively, while the cell survival rate of cells incubated with 7 mM Au/PAH and Au/PVP were reduced 18% and 25% respectively. The control sample only showed a 3% reduction in cell viability when irradiated with the same laser power and duration, demonstrating the effectiveness of Au nanorod based core-shell system, under near infra red laser radiation, to reduce the viability of tumor cells.

MDA MB-231 tumor cells incubated *in-vivo* in athymic nude male mice exhibited cell necrosis when irradiated for 10 minutes with 1.7 W/cm^2 of 980 nm laser irradiation in areas injected with 100 µl, 10 mM Au/PVP nanorods. Tumor areas treated with 980 nm laser irradiation but without the Au/PVP nanorods did not exhibit cell necrosis. This demonstrates the effectiveness of Au nanorod-based photo-thermal treatment to effectively destroy tumor cells in vivo.

4.1 Synthesis of Spectrally-Tailored $Au/SiO_2/Yb:Er:Y_2O_3$ Core/Shell Nanorods

Au nanorods with peak extinction wavelengths of ~ 650 nm were synthesized using a modified literature protocol that was detailed in Chapter 2. The LSPR peaks were chosen to be ~ 10 nm blue-shifted from the emission peak of erbium, since coating with silica and yttria red-shifts the LSPR peak wavelength (Chen 2013). The Au nanorods were coated with a 10 nm silica shell. The Au/SiO_2 nanorods were centrifuged and re-dissolved in 1 ml of DI H_2O. A rare earth yttria coating solution was prepared by mixing 0.89 g YCl_3, 0.1 g $YbCl_3$, 10 mg $ErCl_3$ and 5 g urea in 100 ml of DI water. To deposit a 5 nm thick shell of Y_2O_3 on the Au/SiO_2 core/shell nanorods, 1.4 ml of the coating solution was added to 1.6 ml of Au/SiO_2 core/shell nanorods. Finally, 2 ml of DI water was added and the solution was stirred at 80^oC for 5 hours to complete the deposition.

The cytotoxic, photo-thermal and optical properties of $Au/SiO_2/Yb:Er:Y_2O_3$ core/shell nanorods were assessed for dual-mode bio-imaging and photo-thermal therapy applications and the results were compared to previously reported Au nanorod-based nanostructures, including polystyrene sulfonate-coated Au nanorods (Au/PSS) (Tong 2009), polyanilline hydrochloride-coated Au nanorods (Au/PAH) (Tong, 2012), polyvinylpyrrolidone-coated Au nanorods (Au/PVP) (Sortino, 2012) and silica-coated Au nanorods (Au/SiO_2) (Rodríguez, 2007). Spectrally tailored $Au/SiO_2/Yb:Er:Y_2O_3$ showed comparable photo-thermal properties to these four material systems as well as spectrally sharp photoluminescence peaks around 660 nm, well matched with the biologically transparent window and thus suitable for dual photo-thermal therapy/bio-imaging applications.

4.2 Cell Viability and Morphology Evaluation

4.2.1 Hydrogel Preparation

A gelatin stock solution was prepared by mixing 100 g of gelatin (porcine skin type A 300 bloom, Sigma-Aldrich, MO) in 500 mL of distilled water and stored at 4˚C. The gelatin stock solution was further diluted to a final 7.5% by weight solution and left at room temperature for 2 hours. Microbial transglutaminase (TGase) obtained from Streptomyces membrane (ACTIVA TI Ajinomoto, Japan) was purified by a Sepharose Fast Flow (FF) column. Crude TGase (2g) was dissolved in 20 mM phosphate and 2 mM EDTA at a pH of 6 (Buffer A) and mixed with 3 mL of pre-equilibrated S Sepharose FF beads. After overnight incubation at 4˚C, the mixture of protein solution and beads was loaded into the FF column. After washing with 3 mL of Buffer A, TGase was eluted with Buffer B (Buffer A with 800 mM NaCl). Protein concentration was monitored by the Bradford method (Bio-Rad) utilizing BSA as a standard. Enzyme crosslinking activity was quantified by a spectrophotometric assay using o-phthaldialdehyde (Dinnella, 2002).

4.2.2 Cell Embedment, Viability and Morphology

MDA MB-231 mouse mesenchymal stem cells were purchased from ATCC and cultured in Dulbecco's Modified Eagle Medium (DMEM) (Mediatech, VA) with 10% fetal bovine serum (Lonza, MD). Cells were detached with 0.25% trypsin in Hanks' balanced salts mix (HBSS) (Mediatech, VA). Cells were centrifuged and dispersed in 7.5% gelatin. The supernatant was replaced with a mixture of 200 µL cell-gel. Solutions of 7 mM Au/PSS, Au/PAH, Au/PVP, Au/SiO_2 and Au/SiO_2/Yb:Er:Y_2O_3 core/shell nanorods were synthesized as described in Chapter 2 and homogenously dispersed in the

cell-gel mixture. 12 µL of TGase was added and mixed with each sample. Finally, 20 µL were pipetted into a 48-well plate and incubated at 37˚C for 30 minutes for polymerization. The solidified samples were cultured with DMEM medium with 10% FBS for 48 hours. The CCkit8 reagent was diluted in a 5µL of stock in 200 µL medium ratio and samples were incubated for 3 hours. The cell viability test is a colorometric test which measures the percentage of viable cells in a sample based on the strength of the dye incorporated in the kit. Stronger color is the result of more electrons donated to the dye from viable cells while non-viable cells do not donate electrons to the dye and no color change is produced. Cell survival percentage is determined as a ratio of absorbance measured at 450 nm at the beginning of the experiment and at the end according to calibration standards provided in the kit. The cell morphology changes were observed by microscope (Leitz WETZLAR, Germany) and recorded by a digital camera (Nikon, Japan).

4.2.3 Gelatinolytic Zymograph Assay

The culture medium was dissolved in DMEM without serum and cultured for 24 hours. An SDS sample buffer (250 mM Tris at pH 6.8, 10% SDS, 50% glycerol, and 2.5 mg/ml of bromophenol blue) was added to aliquots of the collected media at a 1:1 ratio. The gel was incubated with 2.5% Triton X-100 and subsequently replaced with a developing buffer containing 50 mM Tris, 5 mM $CaCl_2$, and 200 mM NaCl at a pH of 7.5 at 37°C for 24 hours. The gelatinolytic activities were visualized by staining with Coomassie blue solution (62.5% ethanol, 25% acetic acid and 0.125% Coommasie blue

R250 (Biorad)) and later with the destaining solution (30% methanol and 1% formic acid).

4.2.4 *In-vitro* Tumor Model

MDA MB 231 breast cancer cells incubated with 7mM Au/PSS, Au/PAH, Au/PVP, Au/SiO_2 and Au/SiO_2/Yb:Er:Y_2O_3 nanorods and a control sample were embedded into Tg-gelatin gel 100 µL and cultured for a week. Cell viability was analyzed with a CCkit8 test to establish the baseline. Then cells received 1.7 W/cm^2 of 980 nm laser diode radiation treatment for 5 minutes and cell viability was again analyzed to determine the effect of the laser radiation on the tumor cells.

4.2.5 *In-vivo* Model

Athymic nude male mice were used for the experiment. The protocol was approved by the Institutional Animal Care and Use Committee, University of Southern California. Animals were anesthetized with ketamine/xylazine (10:1 weight ratio) before the injection of MDA MB-231 tumor cells that were mixed with transglutaminase-gelatin gel. The mixture of cell and gel were subcutaneously injected on the back of mouse. After injection, the mice were incubated for 28 days. When tumor size was suitable for treatment, the tumor was injected with 100 µl of 10 mM Au/PVP nanorods. After 5 minutes, the tumor received 1.7 W/cm^2 of 980 nm laser treatment for 10 minutes. The mouse was terminated after 3 days incubation. The tumor was dissected from the mouse and fixed in 10% neutral buffered formalin solution for 18 hours. Explant tumor samples were paraffin-embedded and sectioned before hematoxylin and eosin (H&E) staining was performed.

4.3 Optical Characterization

Upconversion spectra of Au/SiO_2, $SiO_2/Yb:Er:Y_2O_3$ and $Au/SiO_2/Yb:Er:Y_2O_3$ core/ shell nanorods were collected using the experimental setup described in Chapter 2. The specific parameters for the three samples that were investigated are summarized in Table 4.1.

Table 4.1 Summary of sample parameters for Au/SiO_2 and $Au/SiO_2/Yb:Er:Y_2O_3$ core/shell nanorods and $SiO_2/Yb:Er:Y_2O_3$ core/shell nanospheres

Sample	Au Nanorod	SiO_2	$Yb:Er:Y_2O_3$
Au/SiO_2	20 nm diameter 50 nm length	10 nm shell	N/A
$SiO_2/Yb:Er:Y_2O_3$	N/A	400 nm SiO_2 Sphere	10 nm shell 10 wt% Yb, 1 wt% Er
$Au/SiO_2/Yb:Er:Y_2O_3$	20 nm diameter 50 nm length	5nm shell	10 nm shell 10 wt% Yb, 1 wt% Er

Figure 4.1(a) shows the normalized extinction spectra of $Au/SiO_2/Yb:Er:Y_2O_3$, $SiO_2/Yb:Er:Y_2O_3$ and Au/SiO_2 core/shell nanorod solutions along with emission spectrum associated with the Er^{3+} $^4F_{9/2} \rightarrow {}^4I_{15/2}$ radiative energy transition. Figure 4.1(b) show the TEM images of $Au/SiO_2/Yb:Er:Y_2O_3$, $SiO_2/Yb:Er:Y_2O_3$ and Au/SiO_2 core/ shell nanorods.

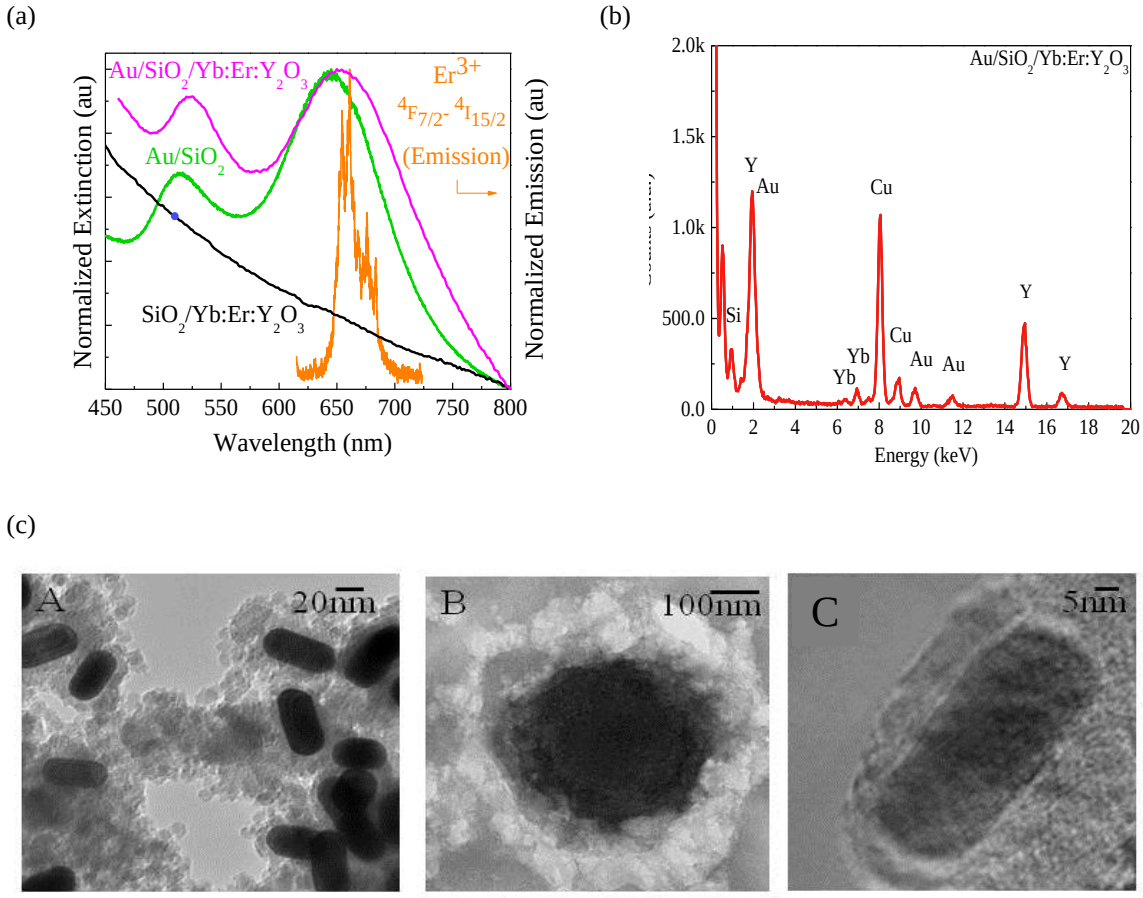


Figure 4.1 (a) Normalized extinction spectra of $Au/SiO_2/Yb:Er:Y_2O_3$, $SiO_2/Yb:Er:Y_2O_3$ and Au/SiO_2 solutions along with emission spectrum associated with the Er^{3+} $^4F_{9/2} \rightarrow {}^4I_{15/2}$ radiative energy transition (b) EDX of $Au/SiO_2/Yb:Er:Y_2O_3$ core/shell nanorods. (c) From left to right: TEM image of (A) Au/SiO_2 (B) $SiO_2/Yb:Er:Y_2O_3$ and (C) $Au/SiO_2/Yb:Er:Y_2O_3$

The extinction wavelength of the $Au/SiO_2/Yb:Er:Y_2O_3$ core/shell nanorod solution spectrally matched the peak emission wavelength of the Er^{3+} $^4F_{9/2} \rightarrow {}^4I_{15/2}$ radiative energy transition in order to optimize energy transfer between the plasmonic and fluorescent components of the hybrid core/shell nanorod. The extinction spectrum of the $Au/SiO_2/Yb:Er:Y_2O_3$ qualitatively resembled the extinction spectrum of the Au/SiO_2 core/shell nanorod reference solution core/shell nanorod solution, however, the extinction

intensity of the $Au/SiO_2/Yb:Er:Y_2O_3$ core/shell nanorod colloidal solution was higher in the 450 nm – 550 nm region than the extinction of the Au/SiO_2 core/shell nanorod colloids. The increased extinction intensity is attributed to the $Yb:Er:Y_2O_3$ shell. The extinction spectrum of $SiO_2/Yb:Er:Y_2O_3$ core/shell nanospheres shows increasing extinction with increasing frequency, typical of Rayleigh scattering.

The PL emission spectra of Au/SiO_2 and $SiO_2/Yb:Er:Y_2O_3$ as a function of 980 nm laser diode excitation power are shown in Figures 4.2 (a) and (b). The PL emission spectrum of Au/SiO_2 showed a broadband luminescence characteristic (Yorulmaz, 2012), while that of $SiO_2/Yb:Er:Y_2O_3$ core/shell nanospheres showed spectrally sharp lines cooresponding to 4f orbital electron transitions.

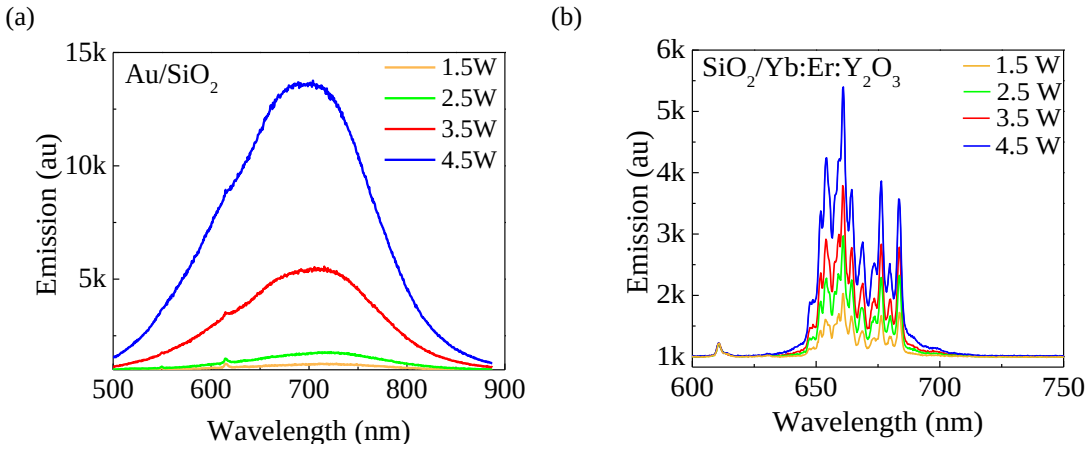


Figure 4.2 Upconversion power spectra (980nm laser diode excitation) of (a) Au/SiO_2, (b) $SiO_2/Yb:Er:Y_2O_3$.

The PL emission spectra of $Au/SiO_2/Yb:Er:Y_2O_3$ as a function of 980 nm laser diode excitation power are shown in Figures 4.3.

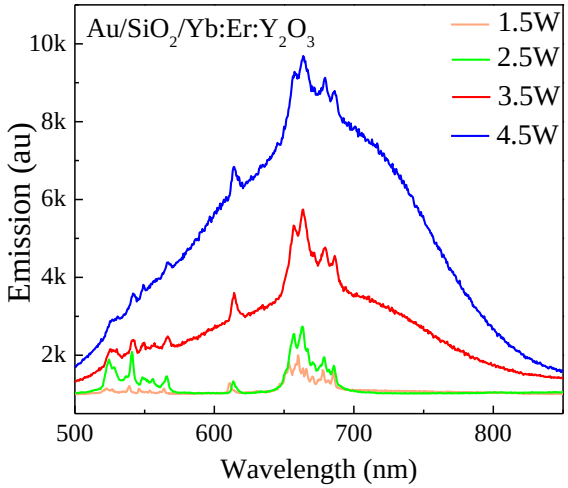


Figure 4.3 Upconversion power spectra (980nm laser diode excitation) of $Au/SiO_2/Yb:Er:Y_2O_3$.

At low excitation powers, the spectral signature of the hybrid plasmonic/fluorescent core/shell nanorods resembled the emission spectrum of the Er^{3+} $^4F_{9/2}\rightarrow{}^4I_{15/2}$ radiative energy transition. With increasing excitation power, the broadband luminescence characteristics of Au inter-band transitions, became more evident. Overall, the core/shell nanorods showed photoluminescence characteristics that displayed the broadband spectral features of Au interband transitions as well as the sharp spectral lines of the Er^{3+} $^4F_{9/2}\rightarrow{}^4I_{15/2}$ energy transition upon excitation with a 980 nm laser diode. Their peak luminescence intensity at 660 nm was 1.81 times higher than that of $SiO_2/Yb:Er:Y_2O_3$ nanospheres at the same wavelength and excitation power (4.5 W/cm^2).

The logarithmic peak PL emission intensity as a function of excitation power for $Au/SiO_2/Yb:Er:Y_2O_3$ and $SiO_2/Yb:Er:Y_2O_3$ are shown in Figure 4.4 (a). The radiative

lifetime measurements for the Er^{3+} $^4F_{9/2} \rightarrow {}^4I_{15/2}$ energy transition in samples $Au/SiO_2/Yb:Er:Y_2O_3$ and $SiO_2/Yb:Er:Y_2O_3$ are shown in Figure 4.4(b). The upconversion PL intensity versus pump power relationship was probed to determine the statistical photon requirement (n) for the upconversion from 980 nm excitation wavelength to the 660 nm emission wavelength. The PL intensity of the $SiO_2/Yb:Er:Y_2O_3$ scaled linearly with pump power. The PL intensity *versus* excitation log-log slope of 1.4 indicates a multi-photon upconversion process. The Au/SiO_2 and $Au/SiO_2/Yb:Er:Y_2O_3$ core/shell nanorods on the other hand displayed non-linear optical characteristics with increasing excitation power.

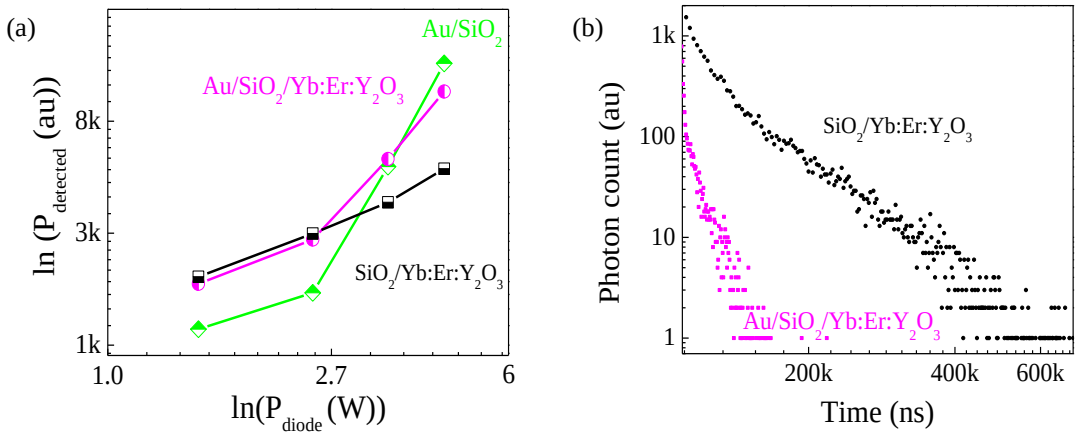


Figure 4.4 (a) Power dependence spectra of samples $Au/SiO_2/Yb:Er:Y_2O_3$, $SiO_2/Yb:Er:Y_2O_3$ and Au/SiO_2. (b) The radiative lifetime measurements for $Au/SiO_2/Yb:Er:Y_2O_3$ and $SiO_2/Yb:Er:Y_2O_3$.

4.4 Plasmonic Photo-Thermal Therapy

Figure 4.5 (a) shows the heating rate of 0 mM (control), 1.75 mM, 7 mM and 14 mM Au/PSS nanorod solutions under 1.7 W/cm^2 980nm laser irradiation. The photo-thermal results indicated that an Au nanorod concentration of 7 mM is needed to achieve

a temperature of > 43°C, at which protein denaturation and disruption of the cellular membrane occurs (Dickerson, 2008). The cell viability is nominally 100% with the control solution, however, as the Au/PSS nanorod concentration increased to 14 mM, in the absence of radiation, the cell viability signal in cell assay was decreased to 91%, as shown in Figure 4.5(b). This result serves as the comparison for Au/SiO_2 and $Au/SiO_2/Yb:Er:Y_2O_3$.

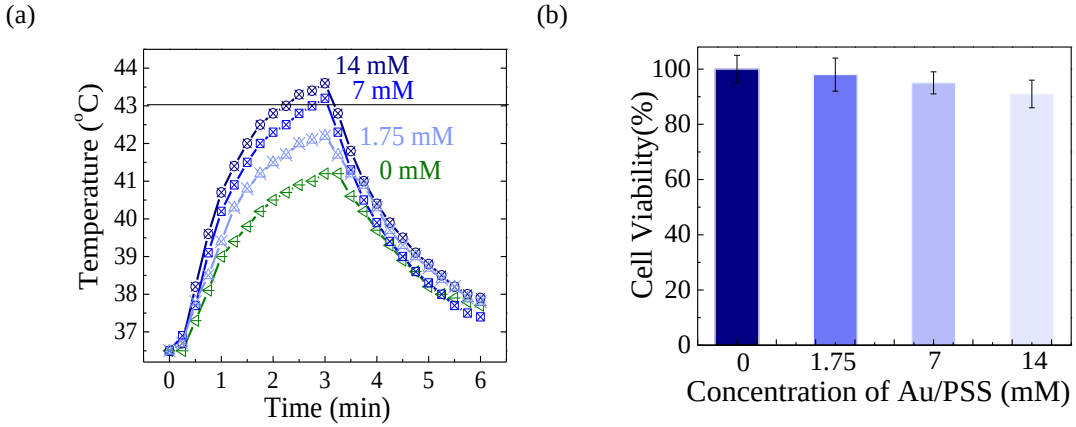


Figure 4.5 (a) Photo-thermal properties of 400 µl of control (0 mM), 1.75 mM, 7 mM and 14 mM Au/PSS nanorods (b) Cell viability of breast cancer cells after incubation with 0 mM, 1.75 mM, 7 mM and 14 mM Au/PSS nanorods.

The photothermal property of 7 mM solutions of $Au/SiO_2/Yb:Er:Y_2O_3$ nanorods is compared to that of Au/PSS, as shown in Figure 4.6 (a). The $Au/SiO_2/Yb:Er:Y_2O_3$ core/shell nanorods showed photo-thermal properties that were comparable to Au/PSS nanorods. The peak temperature of a 400 µL solution of 7 mM $Au/SiO_2/Yb:Er:Y_2O_3$ core/shell nanorods was 0.5°C lower than the peak temperature of Au/PSS after 3 minutes of laser irradiation with 1.7 W/cm^2 980 nm laser diode.

The cytotoxic properties of 7 mM Au/PSS, Au/PAH, Au/PVP, Au/SiO_2 and $Au/SiO_2/Yb:Er:Y_2O_3$ nanorods in the absence of radiation are shown in Figure 4.6 (b). Specifically, the cell survival rate of MDA MB 231 cells incubated with 7 mM Au/SiO_2 and $Au/SiO_2/Yb:Er:Y_2O_3$ core/shell nanorods was 68% and 83%, respectively, while the cell survival rates of MDA MB 231 cells incubated with 7 mM Au/PSS, Au/PAH, Au/PVP were 95%, 91% and 93%, respectively. Cells incubated with Au/SiO_2 particles displayed the lowest cell survival rate (68%), possibly due to the fact that the surface of SiO_2 nanoparticles produces reactive oxygen species through disproportionated reaction resulting in oxidative damage to protein and DNA, making it most cytotoxic (Yang, 2010; Zhang, 2011). The cytotoxicity of $Au/SiO_2/Yb:Er:Y_2O_3$ nanoparticles occurs due to a similar reaction and depends strongly on the nanoparticle geometry as well as the surface chemistry (Andelman, 2011).

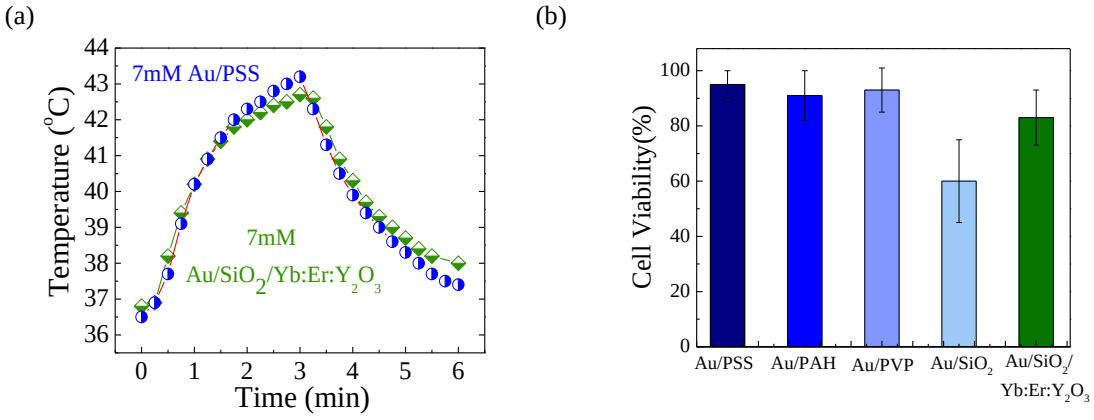


Figure 4.6 (a) Photo-thermal properties of 7 mM Au/PSS and $Au/SiO_2/Yb:Er:Y_2O_3$ core/shell nanorods (b) Cell viability of 7 mM Au/PSS, Au/PAH, Au/PVP, Au/SiO_2 and $Au/SiO_2/Yb:Er:Y_2O_3$ nanorods.

Figure 4.7 shows the results of *in-vitro* tumor photo-thermal therapy using Au/PAH, Au/PVP, Au/SiO_2 and Au/SiO_2/Yb:Er:Y_2O_3 core/shell nanorods, where the MDA MB 231 cells incubated with these core/shell nanorods were irradiated with 5 minutes of 980 nm laser at 1.7 W/cm^2. The control sample showed a 3% reduction in cell viability when irradiated with the same laser power and duration. The cell survival percentage of tumor cells incubated with 7 mM Au/PAH, Au/PVP, Au/SiO_2 and Au/SiO_2/Yb:Er:Y_2O_3 decreased from 91% to 75%, 93% to 70%, 68% to 55% and 83% to 68%, respectively. This translates to a respective reduction of cell viability by 18%, 25% 19%, 18%, demonstrating the effectiveness of the Au nanorod-based core-shell system, under radiation, to reduce the viability of tumor cells. The highest reduction in cell viability was demonstrated by Au/PVP nanorods. This is potentially due to the strong NIR absorption and photo-thermal properties of the polypyrrole polymer in the organic shell of the Au/PVP nanorods (Wang, 2013; Chen, 2011).

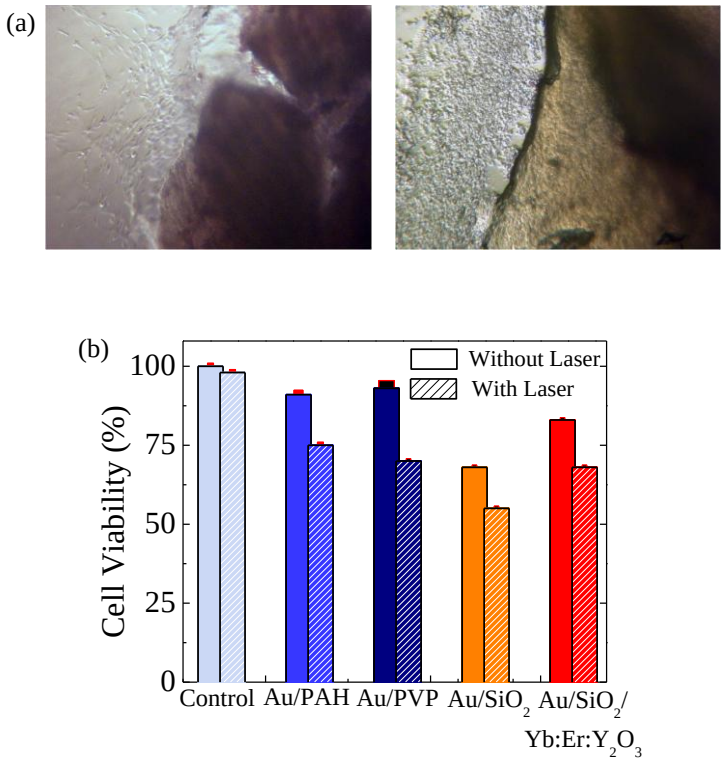


Figure 4.7 (a) Photograph of tumor cells without (left) and with 5 minutes of 1.7 W/cm^2 laser irradiation (right). (b) Cyto-toxicity assay results of breast cancer tumors with 7 mM Au/PAH, Au/PVP, Au/SiO_2 and $Au/SiO_2/Yb:Er:Y_2O_3$ nanorods prior to laser irradiation and after 5 min of 1.7 W/cm^2 980nm laser irradiation.

Figure 4.8 shows the results of *in-vivo* photo-thermal therapy with Au/PVP nanorods. The hemalum-stained nuclei of the cancer cells are the black circles, while the pink regions in the image represent cell necrosis. The results indicate selective hyperthermia in regions where Au/PVP nanorods were injected and exposed to laser irradiation.

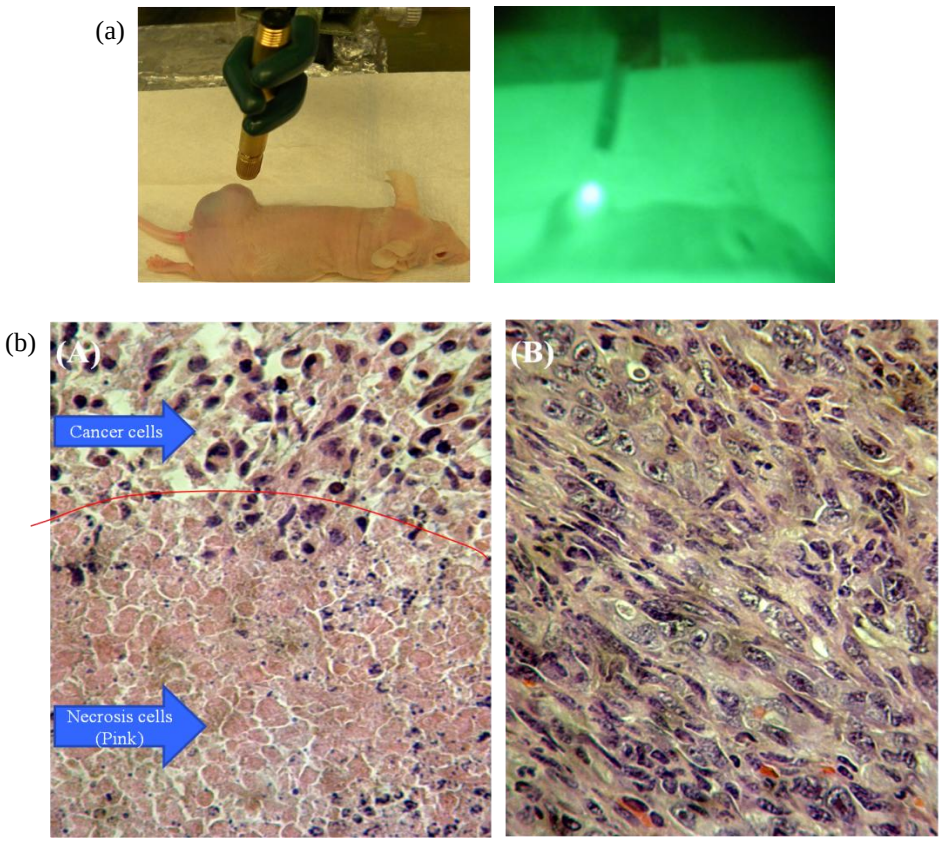


Figure 4.8 (a) Photograph (left) and near infra-red scope image (right) of an athymic nude mouse with a MDA MB 231 breast cancer tumor on its back receiving laser treatment (b) (A) Histology cross section of breast cancer tumor explanted from mouse model after 10 minutes of 1.7 W/cm^2 laser irradiation of a tumor section into which 100 µl of 10mM Au/PVP nanorods were injected (left) and area which received laser treatment but was not injected with Au/PVP nanorods (right).

In conclusion, Au/SiO_2/Yb:Er:Y_2O_3 core/shell nanorods were synthesized, characterized and evaluated as a photo-sensitizer nanomaterial for photo-thermal therapy applications. The peak extinction wavelength of the Au/SiO_2/Yb:Er:Y_2O_3 core/shell nanorod was spectrally matched to the peak emission wavelength of the Er^{3+} ion $^4F_{9/2} \rightarrow {}^4I_{15/2}$ energy transition (~ 660 nm) in order to increase the photonic density of states at that frequency and to enhance the photo-luminescence (PL) intensity of the Er^{3+}

ion (Schietinger, 2009). The $^4F_{9/2} \rightarrow {}^4I_{15/2}$ transition was chosen from the four available Er^{3+} emission bands in the UV-visible regime: 405 nm ($^2H_{9/2} \rightarrow {}^4I_{15/2}$), 520 nm ($^2H_{11/2} \rightarrow {}^4I_{15/2}$), 550 nm ($^4S_{3/2} \rightarrow {}^4I_{15/2}$) and 660 nm ($^4F_{9/2} \rightarrow {}^4I_{15/2}$)) because it falls within the biologically transparent window (Wang, 2011). Upconversion PL spectra as a function of power with 980 nm laser diode excitation were collected for SiO_2/Yb:Er:Y_2O_3 core/shell nanospheres, Au/SiO_2/Yb:Er:Y_2O_3 and Au/SiO_2 core/shell nanorod powders. Both Au interband and Er^{3+} 4f energy transitions were present in the upconverted PL spectra of Au/SiO_2/Yb:Er:Y_2O_3 core/shell nanorod powders. At excitation powers less than 2.5W/cm^2, Au/SiO_2/Yb:Er:Y_2O_3 powders show sharp spectral lines, characteristic of the Er^{3+} 4f orbital energy transitions. Spectrally broad light emission characteristic of Au interband energy transitions was observed with excitation powers above 2.5 W/cm^2. Radiative lifetime measurements were performed on SiO_2/Yb:Er:Y_2O_3 and on Au/SiO_2/Yb:Er:Y_2O_3 powders in order to evaluate whether the radiative dipole oscillation modes of the Au/SiO_2 core/shell nanorods were coupling with the photonic modes associated with the Er^{3+} 4f electronic transitions. The radiative lifetime of the Er^{3+} $^4F_{9/2} \rightarrow {}^4I_{15/2}$ energy transition was 25 μs with the Er^{3+} ion in the Y_2O_3 shell of a SiO_2/Yb:Er:Y_2O_3 nanosphere and 10 μs with the Er^{3+} in the Y_2O_3 shell of a Au/SiO_2/Yb:Er:Y_2O_3 core/shell nanorod. The 2.5-fold decrease in radiative lifetime indicates that the Er^{3+} emitter environment has indeed been modified by the presence of the Au nanorod through the Purcell effect.

CHAPTER 5 CONCLUSION

This work demonstrated that spectrally-tailored plasmonic core/shell nanorods can be utilized to increase the efficiencies of organic photovoltaic devices and can also serve as effective photo-thermal sensitizers in cancer photothermal therapy.

Specifically, for the solar energy application, octadecyltrimethoxysilane-functionalized Au/SiO_2 core/shell nanorods were incorporated into the active layers of two OPV polymer systems: P3HT:$PCB_{60}M$ and PBDTT-DPP:$PC_{60}BM$. For the P3HT:$PC_{60}BM$ polymer with a band edge ~ 670 nm, addition of Au/SiO_2 core/shell nanospheres resulted in a 2.7% improvement in PCE while the addition of the core/shell nanorods of AR ~ 2.5 (extinction peak, λ_{peak} = 670nm) resulted in an 7.1% improvement. For the PBDTT-DPP:$PC_{60}BM$ polymer with a band edge ~ 830 nm, the addition of Au/SiO_2 core/shell nanospheres resulted in a 9.2% improvement, while the addition of core/shell nanorods of AR ~ 4 (extinction peak, λ_{peak} = 830nm) resulted in a 14.4% improvement in PCE. The PCE and J_{sc} enhancements were consistent with external quantum efficiency (EQE) measurements and the EQE enhancements spectrally matched the extinction spectra of Au/SiO_2 nanospheres and nanorods in both OPV polymer systems.

For the cancer photo-thermal therapy application, Au/SiO_2/Yb:Er:Y_2O_3 core/shell nanorods in which the photonic modes of the Yb:Er:Y_2O_3 shell were spectrally and spatially matched to the Au nanorod plasmonic modes were designed, synthesized, characterized and employed in photo-thermal therapy of breast cancer both *in-vitro* and *in-vivo*. The plasmonic/fluorescent Au/SiO_2/Yb:Er:Y_2O_3 core/shell nanorods exhibited

both the broadband photoluminescence characteristic of Au interband transitions and the sharp emission lines characteristic of the Er^{3+} $^4F_{9/2}$ → $^4I_{15/2}$ energy transition upon excitation with 980 nm laser irradiation. The $Au/SiO_2/Yb:Er:Y_2O_3$ showed a 1.81-fold more intense emission signal and a 2.5-fold shorter radiative lifetime compared to $SiO_2/Yb:Er:Y_2O_3$ nanospheres at a wavelength of 655 nm, corresponding to the Er^{3+} $^4F_{9/2}$ → $^4I_{15/2}$ energy transition. In cyto-toxicity assays, the $Au/SiO_2/Yb:Er:Y_2O_3$ core/shell nanorods exhibited comparable cell viability to polystyrene-coated Au nanorods. In photo-thermal therapy treatment tests, selective hyperthermia was induced in breast cancer tumors both *in-vitro* and *in-vivo*.

The gold/dielectric core/shell nanorod structure is well suited to study a number of plasmonic effects. For example, by increasing the SiO_2 shell thickness to > 20nm, it is possible to confine electromagnetic near field of the Au nanorod in the SiO_2 shell. Observed EQE enhancements derived from incorporation of Au/SiO_2 core/shell nanoparticles with thick SiO_2 shells (> 20nm) in OPV devices would stem primarily from light scattering off of the nanoparticles as opposed to near field effects. A thin layer of SiO_2 (< 5nm) on the other hand would ensure that the nanoparticles remain electrically insulating but that the OPV material at the edge of the nanoparticle experiences the enhanced electromagnetic field due to the nanoparticle LSPR near field. A follow up study to this work might include the synthesis of Au/SiO_2 core/shell nanorods with different SiO_2 thicknesses and their incorporation into OPV device active layers in order to study the relative contribution of the near field *versus* light scattering to the overall performance enhancement in plasmonic solar cell devices. The relative contribution of the near field can also be studied using surface enhanced Raman scattering (SERS) by

coating the Au/SiO_2 core/shell nanorods with a Raman active molecule such as pyridine. Au/SiO_2 core/shell nanorods with a thin SiO_2 layer are expected to have stronger SERS signatures.

By pairing Au/SiO_2 core/shell nanorods with different SiO_2 shell thicknesses with quantum emitters (either rare earth ions, quantum dots or laser dye) it is possible to study the effect of the enhanced electromagnetic near field on the spontaneous emission rate of the quantum emitters. Additionally, by controlling the Au nanorod aspect ratio, the effect of spectral match between the plasmonic mode and the fluorescent mode can be systematically studied.

The experimental results of both the solar and the cancer photo-thermal therapy indicated that the concentration of the Au/SiO_2 core/shell nanorods plays a vital role. In the case of active layer-incorporated Au/SiO_2 core/shell nanoparticles, addition of small amounts of plasmonic nanorods increased the device PCE at first, but after a certain critical concentration, the addition of core/shell nanorods was found to degrade device performance. The deleterious effect of a high concentration of Au/SiO_2 core/shell particles in the active layer was shown to be due to the disruption of the OPV polymer morphology. Further study of the mechanisms by which OPV device morphologies are disrupted would assist in the design of plasmonic OPV cells with optimized Au/SiO_2 core/shell nanorod concentrations. This work also demonstrated that in order to achieve maximum heating rates, the concentration of the photo-sensitizer nanorods should be maximized and that the surface chemistry of the nanorods is key to minimize the deleterious effects of incorporating nanorods into cell.

The relative light absorption or scattering contribution to the overall nanoparticle optical response can be designed by changing the size and geometry of Au nanosphere or nanorod core, since larger nanoparticles generally scatter light more efficiently than smaller particles which tend to absorb the majority of the incident light upon them. OPV devices with plasmonic materials embedded in their active layers have to make a tradeoff between incorporating small (< 30 nm) nanoparticles that preferentially absorb light, but disturb active layer morphology to a lesser degree, and larger (> 50 nm) nanoparticles that preferentially scatter light but potentially disturb active layer morphology to a greater degree.

Besides the solar and medical applications discussed in this work, these hybrid core/shell nanorods also have potential as subwavelength optical antennas and as non-linear optical materials. For this purpose, the silica shell should be as thin as possible. An ideal $Au/SiO_2/Yb:Er:Y_2O_3$ core/shell nanorod optical cavity should have a. single crystal Au nanorods of aspect ratio ~2.5 (plasmon resonance ~ 650 nm) and relatively large size (eg. 20 nm diameter x 50 nm length rods). The geometry to maximizes the Au nanorod absorption cross section for optimal photo-thermal energy transduction along with a thin SiO_2 shell (~ 1nm) and a 10 nm thick $Yb:Er:Y_2O_3$ with at least a 10^{20} cm^{-3} Er^{3+} ion concentration in the shell in order to provide sufficient gain to overcome optical losses associated with plasmon resonant electron oscillations at $\lambda = 650$ nm. This represents 5×10^4 Er^{3+} ions in a 10 nm Y_2O_3 shell around a 20x50nm Au nanorod, at a concentration of 10^{20} cm^{-3}.

Similary, an ideal $Au/SiO_2/Yb:Tm:Y_2O_3$ core/shell nanorod optical cavity should have single crystal Au nanorods of aspect ratio ~ 4 (plasmon resonance ~ 800 nm) (eg. 10

nm diameter x 40 nm length rods), a very thin SiO_2 shell (~ 1nm) and a 10 nm thick Yb:Tm:Y_2O_3 with at least a 10^{20} cm^{-3} Tm^{3+} ion concentration. This represents 5×10^4 Tm^{3+} ions in a 10 nm Y_2O_3 shell around a 20x50nm Au nanorod, at a concentration of 10^{20} cm^{-3}.

APPENDICES

APPENDIX A: Light Scattering and Absorption Simulation Code

A.1 Scattering and Absorption Cross Section Calculation of Core/shell Nanospheres

```
close all;
clear all;
global c d1 d2 d3
c=2.99792*10^8;

% load Si_LNK.txt
% lambda0 = Si_LNK(:,1);
% nSiv = Si_LNK(:,2);
% kSiv = Si_LNK(:,3);
% epsRealfile = nSiv.^2-kSiv.^2;
% epsImagfile = 2*nSiv.*kSiv;

lambda_array=zeros(905,2);
load AU.txt
lambda0 = AU(:,1);
epsRealfile = AU(:,2);
epsImagfile = AU(:,3);

%Set wavelength array in nm
lambda=lambda0;
k = 2*pi./lambda;
%lambda=[400:1:1200];
%Frequency (rad/s)
w=2*pi*(c)./(lambda.*10^-9);
%Energy
eV_Drude=(1241.341)./lambda;
Number=length(lambda);

Air_n = 1.00;
SiO2_n=1.48;

e1=epsRealfile+i*epsImagfile; % core (gold)
e2=((SiO2_n)^2)*ones(size(w)); % shell (Silica)
e0=((Air_n)^2)*ones(size(w)); % Medium

% Gain shell with same real part as e1
e2g = e2+i*(-9e-2);


a2 = 200; % Outer radius in nm
a1 = 20; % Inner radius in nm
st = a2-a1; % Shell thickness
f = a1.^(3) / a2.^(3);  % Ratio of inner to outer volume

% % Step through some shell thicknesses
```

```
 for a1=20:40:200;
     st = a2-a1; % Shell thickness
     f = a1.^(3) / a2.^(3);  % Ratio of inner to outer volume

 % Polarizability of a coated sphere
 % B&H 5.36
 alpha=4*pi*a2.^(3).*((e2-e0).*(e1+2*e2)+f*(e1-
e2).*(e0+2*e2))./((e2+2*e0).*(e1+2*e2)+f*(2*e2-2*e0).*(e1-e2));

 absorp= k.*imag(alpha);

 plot(lambda, absorp,'Color',[1-a1/250,.8,a1/200]);

 array=[array,lambda,absorp];

 hold on
 end

% Compare with and without Gain in the core
alpha=4*pi*a2.^(3).*((e2-e0).*(e1+2*e2)+f*(e1-
e2).*(e0+2*e2))./((e2+2*e0).*(e1+2*e2)+f*(2*e2-2*e0).*(e1-e2));

absorp= k.*imag(alpha);
%plot(lambda, absorp,'k');
lambda_array=[lambda_array,lambda,absorp];

hold on
% % Step through some gains
NN=202;
step=0;
for logGain=-.008:.4:-0.01;

%step=step+1;
    e2g = e2+i*(logGain);
% Polarizability of a coated sphere
% B&H 5.36
alphaGain=4*pi*a2.^(3).*((e2-e0).*(e1+2*e2g)+f*(e1-
e2g).*(e0+2*e2g))./((e2g+2*e0).*(e1+2*e2g)+f*(2*e2g-2*e0).*(e1-e2g));
absorpGain= k.*imag(alphaGain);
if abs(max(absorpGain))>abs(min(absorpGain));
%    plot(lambda, absorpGain,'r');
    lambda_array=[lambda_array,lambda,absorpGain];
else
%   plot(lambda, absorpGain,'b');
   lambda_array=[lambda_array,lambda,absorpGain];
end


save au_core_shell.txt lambda_array -ascii;

hold on
end
xlim([300,700]);
```

A.2. Scattering and Absorption Cross Section Calculation of Core/Shell Nanorods

```
clear all; %clear variables and stuff
clc; %clear command window
clf(figure(1));
clf(figure(2));
clf(figure(3));
%clf(figure(4));

%Load dielectric function of metal from file
load AU.txt
c=3*10^8;
lambda=10^-1*AU(:,1); %wavelength in nm



omegaAU=2*pi*c./(lambda*10^-9);
n=AU(:,2); k=AU(:,3);
epsPalikReal=n.^2-k.^2;
epsPalikImag=2*n.*k;
%Spline eps as a function of omega.
epsRealSpline=spline(omegaAU,epsPalikReal);
epsImagSpline=spline(omegaAU,epsPalikImag);

%drude dispersion relation parameters
epsAuStatic=10.54;
epsAuHigh=9.54;
omegaPAu=2*pi*2.149e15;
gammaAu=2*pi*12.5e13;

%lorentz-drude dispersion relation parameters in eV
AuLD_f0=0.760;
AuLD_Gamma0=0.053;
AuLD_omegaP=9.03;
AuLD_f=[0.024,0.010,0.071,0.601,4.384];
AuLD_Gamma=[0.241,0.345,0.870,2.494,2.214];
AuLD_omega=[0.415,0.830,2.969,4.304,13.32];
%hbar in eV*s; energy = omega*hbar
hbar=6.5821e-16;

%generate uniform vector of omegas
omega=10^15*[0.005:0.005:6];
for ii=1:length(omega)
   %create Palik vector of epsilon(omega)
   epsReal(ii)=ppval(epsRealSpline,omega(ii));
   epsImag(ii)=ppval(epsImagSpline,omega(ii));
   %create Drude vector of epsilon(omega)
   epsAuDrude(ii)=                                epsAuHigh-((epsAuStatic-
epsAuHigh)*omegaPAu^2/(omega(ii)^2+i*omega(ii)*gammaAu));

   %create Lorentz-Drude vector of epsilon
   %note omega is in radians while all LD parameters are in eV --
   %therefore hbars in formula
   epsAuLD_Bound=0; %initialize
```

```
   for ll=1:length(AuLD_f);

epsAuLD_Bound=epsAuLD_Bound+(AuLD_f(ll)*AuLD_omegaP^2)/((AuLD_omega(ll)
^2-(omega(ii)*hbar)^2)-i*omega(ii)*hbar*AuLD_Gamma(ll));
   end
   epsAuLD(ii)=1-
(AuLD_f0*AuLD_omegaP^2)/(omega(ii)*hbar*(omega(ii)*hbar+i*AuLD_Gamma0))
+epsAuLD_Bound;
end

epsAuPalik=epsReal+i*epsImag;
epsAir=1*ones(1,length(omega));
epsWater=1.69*ones(1,length(omega));
epsSiO2=2.10*ones(1,length(omega));    % from Alfons' group (slightly
porous?)
%epsSiO2=2.14*ones(1,length(omega));  % from internet
epsGlass=2.5*ones(1,length(omega));
epsQuartz=(1.46)^2*ones(1,length(omega));
%epsFlintGlass=(1.66)^2*ones(1,length(omega));
epsITO=(1.9)^2*ones(1,length(omega));     %  Weakly  dispersive;  n=1.9
around 730 nm
%epsDiamond=(2.5)^2*ones(1,length(omega));
epsUser = 0.7*epsAir+0.3*epsSiO2;

%spherical particles? (else spheroidal)
sphere=0;
    %prolate? (cigar shaped) (else, oblate)
    prolate=1;
%coreshell particle?
coreshell=1;
%normalize results to particle volume?
normalizeToVolume=1;
%normalize results to 1? (discard absolute magnitude information...)
normalizeResults=0;

%major radius of particle (only radius, if sphere) (core, if core-
shell)

r1 = 240*10^-9;
%minor radius of particle (core, if core-shell)
r3 = 20*10^-9;
if r3 > r1
    fprintf('Error: r3 greater than r1\n');
end

%epsilon of core
epsC = epsAuDrude;
%epsilon of matrix
epsM = epsAir;
if coreshell
    %dielectric of shell
    epsS=epsSiO2;
    shellthickness=55*10^-9;
    %major radius of shell
    r1Shell=r1+shellthickness;
```

```
    %minor radius of shell
    r3Shell=r3+shellthickness;
end

%direction of incident beam in relative to [r1,r2,r3]
xInc = [1,1,1];
    %normalize to unit vector
    xInc = xInc/norm(xInc);
    %vector weighting doodles
    a11 = dot(xInc,[1,0,0]);
    a21 = dot(xInc,[0,1,0]);
    a31 = dot(xInc,[0,0,1]);

%L factors
if sphere
    L=[1/3,1/3,1/3];
    r2=r1;
    r3=r1;
    if coreshell
        r2Shell=r1Shell;
        LShell=[1/3,1/3,1/3];
    end
else %spheroid
    %eccentricity
    e=sqrt(1-r3^2/r1^2);
    g=sqrt((1-e^2)/e^2);
    if coreshell
        eShell=sqrt(1-r3Shell^2/r1Shell^2);
        gShell=sqrt((1-eShell^2)/eShell^2);
    end
    if prolate
        r2=r3;
        L(1)=g^2*(-1+1/(2*e)*log((1+e)/(1-e)));
        L(3)=(1-L(1))/2;
        L(2)=L(3);
        if coreshell
            r2Shell=r3Shell;
            LShell(1)=gShell^2*(-1+1/(2*eShell)*log((1+eShell)/(1-
eShell)));
            LShell(3)=(1-LShell(1))/2;
            LShell(2)=LShell(3);
        end
    else %oblate
        r2=r1;
        L(1)=g/(2*e^2)*(pi/2-atan(g))-g^2/2;
        L(2)=L(1);
        L(3)=1-2*L(1);
        if coreshell
            r2Shell=r1Shell;
            LShell(1)=gShell/(2*eShell^2)*(pi/2-atan(gShell))-
gShell^2/2;
            LShell(2)=LShell(1);
            LShell(3)=1-2*LShell(1);
        end
    end
```

```
end

if coreshell
    %volume of total particle
    volume=4/3*pi*r1Shell*r2Shell*r3Shell;
    %core fraction
    fraction=r1*r2*r3/(r1Shell*r2Shell*r3Shell);
else
    volume=4/3*pi*r1*r2*r3;
end

imagWavevector=0;

for jj=1:length(omega)
    %incident wavevector -- k^2 = omega^2 * eps * mu
    %eps = eps * eps0  -- mu = mu * mu0
    %eps0 * mu0 = 1/c^2

    k_inc(jj) = sqrt(omega(jj).^2.*epsM(jj)/c^2);
    if imag(k_inc(jj))
        imagWavevector=1;
    end

    if coreshell
        %polarizability
        alpha1(jj)   =   volume*((epsS(jj)-epsM(jj))*(epsS(jj)+(epsC(jj)-
epsS(jj))*(L(1)-fraction*LShell(1)))+fraction*epsS(jj)*(epsC(jj)-
epsS(jj)))...
            /((epsS(jj)+(epsC(jj)-epsS(jj))*(L(1)-
fraction*LShell(1)))*(epsM(jj)+(epsS(jj)-
epsM(jj))*LShell(1))+fraction*LShell(1)*epsS(jj)*(epsC(jj)-epsS(jj)));
        alpha2(jj)   =   volume*((epsS(jj)-epsM(jj))*(epsS(jj)+(epsC(jj)-
epsS(jj))*(L(2)-fraction*LShell(2)))+fraction*epsS(jj)*(epsC(jj)-
epsS(jj)))...
            /((epsS(jj)+(epsC(jj)-epsS(jj))*(L(2)-
fraction*LShell(2)))*(epsM(jj)+(epsS(jj)-
epsM(jj))*LShell(2))+fraction*LShell(2)*epsS(jj)*(epsC(jj)-epsS(jj)));
        alpha3(jj)   =   volume*((epsS(jj)-epsM(jj))*(epsS(jj)+(epsC(jj)-
epsS(jj))*(L(3)-fraction*LShell(3)))+fraction*epsS(jj)*(epsC(jj)-
epsS(jj)))...
            /((epsS(jj)+(epsC(jj)-epsS(jj))*(L(3)-
fraction*LShell(3)))*(epsM(jj)+(epsS(jj)-
epsM(jj))*LShell(3))+fraction*LShell(3)*epsS(jj)*(epsC(jj)-epsS(jj)));
    else %not core shell
        %polarizability
        alpha1(jj)              =              4*pi*r1*r2*r3*(epsC(jj)-
epsM(jj))/(3*epsM(jj)+3*L(1)*(epsC(jj)-epsM(jj)));
        alpha2(jj)              =              4*pi*r1*r2*r3*(epsC(jj)-
epsM(jj))/(3*epsM(jj)+3*L(2)*(epsC(jj)-epsM(jj)));
        alpha3(jj)              =              4*pi*r1*r2*r3*(epsC(jj)-
epsM(jj))/(3*epsM(jj)+3*L(3)*(epsC(jj)-epsM(jj)));
    end
    %extinction cross section
    %  imag(k.*alpha)  ==  k.*imag(alpha)  for  real  k,  and  is  more
correct(?)
```

```
    % for complex k
    C_ext1(jj) = imag(k_inc(jj).*alpha1(jj));
    C_ext2(jj) = imag(k_inc(jj).*alpha2(jj));
    C_ext3(jj) = imag(k_inc(jj).*alpha3(jj));
    C_sca1(jj) = (k_inc(jj).^4/(6*pi).*abs(alpha1(jj))^2);

    lambdaFree(jj) = 2*pi*c./omega(jj);

    C_ext(jj) = imag(k_inc(jj).*(alpha1(jj)*a11^2 + alpha2(jj)*a21^2 +
alpha3(jj)*a31^2));


 end

if normalizeResults
    C_ext1 = C_ext1/max(C_ext1);
    C_ext2 = C_ext2/max(C_ext2);
    C_ext3 = C_ext3/max(C_ext3);
    C_ext = C_ext/max(C_ext);
    C_sca1 = C_sca1/max(C_sca1);
else
    if normalizeToVolume
        C_ext1 = C_ext1/volume;
        C_ext2 = C_ext2/volume;
        C_ext3 = C_ext3/volume;
        C_ext = C_ext/volume;
        C_sca1 = C_sca1/volume;
    end
end
end
%{
%figure(4)
%plot(lambdaFree,2*pi./k_inc,'k');
%hold on;
%plot(lambdaFree,2*pi./imag(k_inc),'r');
%}

%figure(4)
%plot(lambdaFree,C_sca1,'k');
%xlim([300e-9 1500e-9]);
%xlabel('lambda');
%if normalizeResults
%    ylabel('scattering?, arbitrary units');
%else
%    if normalizeToVolume
%        ylabel('scattering? per volume');
%    else
%        ylabel('scattering? per particle');
%    end
%end


figure(1)
plot(lambdaFree,C_ext,'k');
```

```
A=[lambdaFree;C_ext];
B=rot90(A);

save feb_24020.txt B -ASCII



hold on
%if not(sphere)
    %plot(lambda,C_ext1,'r');
    %plot(lambda,C_ext3,'b');
%end
xlim([300e-9 1500e-9]);
xlabel('lambda');
if normalizeResults
    ylabel('extinction, arbitrary units');
else
    if normalizeToVolume
        ylabel('extinction cross section per volume');
    else
        ylabel('extinction cross section per particle');
    end
end

figure(2)
plot(omega,C_ext,'k');
hold on
if not(sphere)
    plot(omega,C_ext1,'r');
    plot(omega,C_ext3,'b');
end
xlabel('omega');
if normalizeResults
    ylabel('extinction, arbitrary units');
else
    if normalizeToVolume
        ylabel('extinction cross section per volume');
    else
        ylabel('extinction cross section per particle');
    end
end

if imagWavevector
    fprintf('Warning: Imaginary incident wavevector.  Maybe look at
scattering power instead of Cext?');
    %for voids in metal, you might get negative Cext.  This reflects
that
    %the scattering is more than compensated by a lack of absorption in
the
    %surrounding metal 'medium'!
end

figure(3)
plot(omegaAU, epsPalikReal,'.k');
hold on
```

```
plot(omegaAU, epsPalikImag,'.k');
plot(omega,epsReal,'k');
plot(omega,epsImag,'--k');
plot(omega,real(epsAuDrude),'b');
plot(omega,imag(epsAuDrude),'--b');
plot(omega,real(epsAuLD),'r');
plot(omega,imag(epsAuLD),'--r');
ylim([-200 50]);
xlim([1 6]*1e15);
ylabel('epsilon');
xlabel('omega');



statusString='';
if sphere
    statusString=strcat(statusString,' Spherical');
else
    if prolate
        statusString=strcat(statusString,' Prolate');
    else
        statusString=strcat(statusString,' Oblate');
    end
end
if coreshell
    statusString=strcat(statusString,' Coreshell\n');
else
    statusString=strcat(statusString,' Solid\n');
end
fprintf(statusString);
```

APPENDIX B: Core/Shell Nanorod Synthesis

B.1. Au nanorod synthesis

The precursor concentrations used to synthesize the Au nanorod solutions are summarized in Table B.1.

Table B.1 Precursor concentrations and volumes

Precursor	Concentration	Volume
$HAuCl_4$	1 mM	20 ml
CTAB	0.1 M	20 ml
$C_6H_8O_6$	100 mM	300 μl
$AgNO_3$	5 mM	0.3 ml – 1.5 ml
Au seed soln	0.5 mM	25 μl

In order to synthesize Au nanorods, first a seed solution is prepared. The seed solution is prepared by mixing 5 ml of 0.5mM $HAuCl_4$ with 5 ml of 0.1M CTAB. The seed solution should be an orange-brown color. If the seed solution is dark yellow, corresponding to charge transfer bands in Au^{3+} ions, it means that not enough reducing agent ($NaBH_4$) was added. If the seed solution is red, that means the solution contains Au nanospheres of diameter greater than 5nm. Using this solution will for Au nanorod synthesis will yield Au nanorods with diameters greater than 10nm in general or spheres.

B.2. Polyelectrolyte coating

Precursor concentrations required for the polyelectrolyte layer by layer process are summarized in Table B.2.

Table B.2 Polyelectrolyte layer by layer precursor concentrations and volumes

Precursor	Concentration	Volume
PSS	2 g/L	20 ml
PAH	2 g/L	20 ml
PVP	4 g/L	20 ml

In order to coat the as-synthesized, CTAB-stabilized Au nanorods, 10 ml of CTAB-stabilized Au nanorod solution were centrifuged and redissolved in 3 ml of distilled water. This and then added to 3 ml of an aqueous solution containing poly-styrene sulfonate (PSS) (2 mg/mL and 6 mM NaCl) and stirred for approximately three hours. The PSS-modified particles were centrifuged twice to remove any excess PSS and redispersed in 3 ml of deionized water. The dispersion was then added drop-wise under vigorous stirring to 3 ml of an aqueous solution of 2mg/ml poly(anilline hydrochloride) (PAH) and 6 mM NaCl). PAH adsorption was allowed to proceed for three hours. The sample was then centrifuged to remove excess polyelectrolyte and redispersed in 3 mL of deionized water. Finally, 3 ml of the PSS/PAH functionalized Au spheres were added to a polyvinylpyrrolidone (PVP) solution (4mg/ml). The mixture was stirred for approximately twelve hours, centrifuged to remove any excess polymer, and redispersed in 0.2 mL of deionized water

B.3. Silica Shell Deposition

Precursor concentrations required for deposition of a SiO_2 shell on Au nanorods are summarized in Table B.3.

Table B.3 Silica shell deposition precursor concentrations and volumes

Precursor	Concentration	Volume
C_2H_5OH	100%	1 ml
H_2O	n/a	0.6 ml
NH_3	2 M	0.1 ml
Au/PVP soln	0.8M	0.2 ml

PVP-coated nanorods are first added to 2 mL of isopropyl-alcohol (IPA). Once the Au nanoparticles are transferred into IPA, the pH is adjusted to ~ 10 by adding 1.5 ml, 5 vol % NH_3 in IPA (30% in water)., 0.5 ml of TEOS (1 vol% in ethanol) is added under gentle stirring and the reaction is allowed to proceed overnight.

B.4. Organosilane Coating

Precursor concentrations required for deposition of an OTMS layer on Au/SiO_2 core/sh nanorods are summarized in Table B.4.

Table B.4 Organosilane functionalization of Au/SiO_2 core/shell nanorod precursor concentrations and volumes

Precursor	Concentration	Volume
OTMS in Chloroform	3%	300 µl
Chloroform	100%	1 ml
NH_3	2 M	30 µl
Au/SiO_2 soln	0.8 M	0.1 ml

Au/SiO_2 core/shell nanorods are centrifuged and redissolved in 3 ml of ethanol containing 30 µl of NH_4OH (32%). 300 µl of OTMS chloroform solution (3%) is added with vigorous stirring and left overnight.

APPENDIX C: Photoluminescence

C.1 Safety Measures

Make sure the following measures are met before operating the laser:

1. Entryway access control include:

a. Doorway interlock: allowing entry only when the laser is off. This is controlled by the Entry-Guard laser interlock system (Figure 1), which is integrated to the key pad located on the left wall outside of the lab, allowing for the key to turn only when the laser is off.

b. Illuminated entryway laser warning sign to denote the laser operating condition: "Laser On" and "Laser Off".

2. Wooden Door (1/4" thick)

a. Semi-permanently mount to the floor by bolting. Note: the door can be removed by unbolting when wide access to the entry lab door is necessary b. Paint with fire-resistant black paint to minimize reflection of the laser beam

3. Black laser Curtain (heavy duty 35-ounce 0.044"-thick flame retardant, nonfraying and chemical resistant flexible fabric)

a. Rail tracks installed on the ceiling right above the sliding door and the wall (see Figure 3 below)

b. The 42"W x 96" L table is enclosed by the black curtain (96" H). The curtain can only slide to the portion parallel to the sliding door.

C.2 Emergency Shutdown

Push in the red button labeled "EMERGENCY STOP" to shut down the laser.

C.3. Operating Procedures

Check and enable all safety measures described in section 2

· Functional doorway interlock (i.e. illuminated sign for “Laser Off” is on)

· Wooden door

· Black curtain enclosed experimental area

· Mounted laser on the table

Put on laser eyewear protection

To turn on the Argon ion laser:

1. Make sure the sample and laser beam path are all properly aligned for the experiment so as to minimize the experimenters time inside the enclosed laser area.

2. Close the laser curtain.

3. Set the beam shutter on the laser head to OPEN position

4. Turn on the chiller (Neslab HX-50) and make sure the cooling water flow rate is at least 2.2 gallon per minute.

5. Turn on the circuit breaker

6. On the Entry-Guard panel, insert and turn the key to ON position (top-left corner). The POWER ON light will light

7. Insert the key and turn on the LOCK switch on the laser power supply.

Note: the white LASER EMISSION light will be on. The FAULT light and WATER FLOW light will also come on for half a second to verify the water flow.

8. Select AUTO start. A green light above the selected switch will come on.

9. Adjust the WAVELENGTH calibrator to the operating wavelength.

10. Select the desired power by adjusting the power range selector.

11. Press the PRESS TO START button on the Entry-Guard panel

12. Press the START button on the laser power supply. The START DELAY indicator on the laser power supply will be on for 30 seconds.

To turn off the Argon ion laser:

1. Decrease the laser power to ~1 A.

2. Press STOP on the laser power supply.

3. On the Entry-Guard panel, turn the key to OFF position and remove the key.

4. Turn off the LOCK switch on the laser power supply and remove the key.

5. Turn off the circuit breaker (Pnl N2 panel 8·10·12).

6. Set the beam shutter on the laser head to CLOSE position

7. Wait 15 minutes for the laser to cool down

8. Turn off the chiller (Neslab HX-50).

BIBLIOGRAPHY

Aina, O. H., T. C. Sroka, M.-L. Chen and K. S. Lam (2002). "Therapeutic cancer targeting peptides." Peptide Science **66**(3): 184-199.

Alivisatos, A. P., W. Gu and C. Larabell (2005). "Quantum dots as cellular probes." Annual Review of Biomedical Engineering **7**(1): 55-76.

Alkilany, A. M., L. B. Thompson, S. P. Boulos, P. N. Sisco and C. J. Murphy (2012). "Gold nanorods: Their potential for photothermal therapeutics and drug delivery, tempered by the complexity of their biological interactions." Advanced Drug Delivery Reviews **64**(2): 190-199.

Alkilany, A. M., L. B. Thompson and C. J. Murphy (2010). "Polyelectrolyte Coating Provides a Facile Route to Suspend Gold Nanorods in Polar Organic Solvents and Hydrophobic Polymers." ACS Applied Materials & Interfaces **2**(12): 3417-3421.

Andelman, T., Gordonov, S., Busto, G., Moghe, P. and R. Riman (2010). "Synthesis and Cytotoxicity of Y_2O_3 Nanoparticles of Various Morphologies." Nanoscale Res Lett 5: 263-273.

Anger, P., P. Bharadwaj and L. Novotny (2006). "Enhancement and quenching of single-molecule fluorescence." Physical Review Letters **96**(11).

Atwater, H. A. and A. Polman (2010). "Plasmonics for improved photovoltaic devices." **9**(3): 205-213.

Auzel, F. (2003). "Upconversion and Anti-Stokes Processes with f and d Ions in Solids." Chemical Reviews **104**(1): 139-174.

Beversluis, M. R., A. Bouhelier and L. Novotny (2003). "Continuum generation from single gold nanostructures through near-field mediated intraband transitions." Physical Review B **68**(11).

Bian, R. X., R. C. Dunn and X. S. Xie (1995). "Single molecule emission characteristics in near-field microscopy." Physical Review Letters **75**(26): 4772-4775.

Bouhelier, A., M. R. Beversluis and L. Novotny (2003). "Characterization of nanoplasmonic structures by locally excited photoluminescence." Applied Physics Letters **83**(24): 5041-5043.

Boyd, G. T., T. Rasing, J. R. R. Leite and Y. R. Shen (1984). "Local field enhancement on rough surfaces of metals, semi-metal and semi-conductors with the use of optical 2nd harmonic generation." Physical Review B **30**(2): 519-526.

Boyd, G. T., Z. H. Yu and Y. R. Shen (1986). "Photoinduced luminescence from the noble metals and its enhancement on roughened surfaces." Physical Review B **33**(12): 7923-7936.

Brady, M. A., G. M. Su and M. L. Chabinyc (2011). "Recent progress in the morphology of bulk heterojunction photovoltaics." Soft Matter **7**(23): 11065-11077.

Brust, M., M. Walker, D. Bethell, D. J. Schiffrin and R. Whyman (1994). "Synthesis of thiol-derivatised gold nanoparticles in a two-phase Liquid-Liquid system." Journal of the Chemical Society, Chemical Communications(7): 801-802.

Campbell, S. D. and R. W. Ziolkowski (2012). "The Performance of Active Coated Nanoparticles Based on Quantum-Dot Gain Media." Advances in OptoElectronics **5 (**2): 115-119.

Caruso, F. (2001). "Nanoengineering of Particle Surfaces." Advanced Materials **13**(1): 11-22.

Catchpole, K. R. and A. Polman (2008). "Plasmonic solar cells." Opt. Express **16**(26): 21793-21800.

Chang, J.-Y., H. Wu, H. Chen, Y.-C. Ling and W. Tan (2005). "Oriented assembly of Au nanorods using biorecognition system." Chemical Communications **0**(8): 1092-1094.

Chen, C. K., A. R. B. Decastro and Y. R. Shen (1981). "Surface enhanced 2^{nd} harmonic generation." Physical Review Letters **46**(2): 145-148.

Chen, G., J. Shen, T. Y. Ohulchanskyy, N. J. Patel, A. Kutikov, Z. Li, J. Song, R. K. Pandey, H. Ågren, P. N. Prasad and G. Han (2012). "(α-$NaYbF_4$:Tm^{3+})/CaF_2 Core/Shell Nanoparticles with Efficient Near-Infrared to Near-Infrared Upconversion for High-Contrast Deep Tissue Bioimaging." ACS Nano **6**(9): 8280-8287.

Chen, H., L. Shao, Q. Li and J. Wang (2013). "Gold nanorods and their plasmonic properties." Chemical Society Reviews.

Chen, L.-C., C.-W. Wei, J. S. Souris, S.-H. Cheng, C.-T. Chen, C.-S. Yang, P.-C. Li and L.-W. Lo (2010). "Enhanced photoacoustic stability of gold nanorods by silica matrix confinement." Journal of Biomedical Optics **15**(1): 016010-016010.

Chen, M., X. Fang, S. Tang and N. Zheng (2012). "Polypyrrole nanoparticles for high-performance in vivo near infrared photothermal cancer therapy." Chem. Commun. **48**: 8934-8936.

Chen, Y.-S., W. Frey, S. Kim, K. Homan, P. Kruizinga, K. Sokolov and S. Emelianov (2010). "Enhanced thermal stability of silica-coated gold nanorods for photoacoustic imaging and image-guided therapy." Opt. Express **18**(9): 8867-8878.

Cheng, P.-P., G.-F. Ma, J. Li, Y. Xiao, Z.-Q. Xu, G.-Q. Fan, Y.-Q. Li, S.-T. Lee and J.-X. Tang (2012). "Plasmonic backscattering enhancement for inverted polymer solar cells." Journal of Materials Chemistry **22**(42): 22781-22787.

Choi, W. I., J.-Y. Kim, C. Kang, C. C. Byeon, Y. H. Kim and G. Tae (2011). "Tumor Regression In Vivo by Photothermal Therapy Based on Gold-Nanorod-Loaded, Functional Nanocarriers." ACS Nano **5**(3): 1995-2003.

Cortesi, R., E. Esposito, E. Menegatti, R. Gambari and C. Nastruzzi (1996). "Effect of cationic liposome composition on in vitro cytotoxicity and protective effect on carried DNA." International Journal of Pharmaceutics **139**(1–2): 69-78.

Creighton, J. A., C. G. Blatchford and M. G. Albrecht (1979). "Plasma resonance enhancement of Raman scattering by pyridine adsorbed on silver or gold sol particles of size comparable to the excitation wavelength." Journal of the Chemical Society, Faraday Transactions 2: Molecular and Chemical Physics **75**(0): 790-798.

Cyrankiewicz, M., T. Wybranowski and S. Kruszewski (2007). "Study of SERS efficiency of metallic colloidal systems." Journal of Physics: Conference Series **79**(1): 012013.

Dahlin, A., M. Zäch, T. Rindzevicius, M. Käll, D. S. Sutherland and F. Höök (2005). "Localized Surface Plasmon Resonance Sensing of Lipid-Membrane-Mediated Biorecognition Events." Journal of the American Chemical Society **127**(14): 5043-5048.

Decher, G. (1997). "Fuzzy Nanoassemblies: Toward Layered Polymeric Multicomposites." Science **277**(5330): 1232-1237.

Deckman, H. W., C. B. Roxlo and E. Yablonovitch (1983). "Maximum statistical increase of optical absorption in textured semiconductor films." Opt. Lett. Optics Letters **8**(9): 491-493.

Dickerson, E. B., E. C. Dreaden, X. Huang, I. H. El-Sayed, H. Chu, S. Pushpanketh, J. F. McDonald and M. A. El-Sayed (2008). "Gold nanorod assisted near-infrared plasmonic photothermal therapy (PPTT) of squamous cell carcinoma in mice." Cancer Letters **269**(1): 57-66.

Dickson, R. M. and L. A. Lyon (2000). "Unidirectional plasmon propagation in metallic nanowires." Journal of Physical Chemistry B **104**(26): 6095-6098.

Dinnella, C., M. T. Gargaro, R. Rossano and E. Monteleone (2002). "Spectrophotometric assay using o-phtaldialdehyde for the determination of transglutaminase activity on casein." Food Chemistry **78**(3): 363-368.

Dougherty, T. J. (1987). "Photosensitizers: Therapy and detection of malignant tumors." Photochemistry and Photobiology **45**: 879-889.

Dreaden, E. C., A. M. Alkilany, X. Huang, C. J. Murphy and M. A. El-Sayed (2012). "The golden age: gold nanoparticles for biomedicine." Chemical Society Reviews **41**(7): 2740-2779.

Dreaden, E. C., M. A. Mackey, X. Huang, B. Kang and M. A. El-Sayed (2011). "Beating cancer in multiple ways using nanogold." Chemical Society Reviews **40**(7): 3391-3404.

Dulkeith, E., T. Niedereichholz, T. A. Klar, J. Feldmann, G. von Plessen, D. I. Gittins, K. S. Mayya and F. Caruso (2004). "Plasmon emission in photoexcited gold nanoparticles." Physical Review B **70**(20).

Duong, D. T., B. Walker, J. Lin, C. Kim, J. Love, B. Purushothaman, J. E. Anthony and T. Q. Nguyen (2012). "Molecular solubility and Hansen solubility parameters for the analysis of phase separation in bulk heterojunctions." Journal of Polymer Science Part B-Polymer Physics **50**(20): 1405-1413.

El-Sayed, M. A. (2001). "Some Interesting Properties of Metals Confined in Time and Nanometer Space of Different Shapes." Accounts of Chemical Research **34**(4): 257-264.

Englebienne, P. (1998). "Use of colloidal gold surface plasmon resonance peak shift to infer affinity constants from the interactions between protein antigens and antibodies specific for single or multiple epitopes." Analyst **123**(7): 1599-1603.

Faraday, M. (1857). "The Bakerian Lecture: Experimental Relations of Gold (and Other Metals) to Light." Philosophical Transactions of the Royal Society of London **147**: 145-181.

Ferry, V. E., M. A. Verschuuren, H. B. T. Li, E. Verhagen, R. J. Walters, R. E. I. Schropp, H. A. Atwater and A. Polman (2010). "Light trapping in ultrathin plasmonic solar cells." Opt. Express **18**(S2): A237-A245.

Fischer, S., F. Hallermann, T. Eichelkraut, G. von Plessen, K. W. Krämer, D. Biner, H. Steinkemper, M. Hermle and J. C. Goldschmidt (2012). "Plasmon enhanced

upconversion luminescence near gold nanoparticles;simulation and analysis of the interactions." Opt. Express **20**(1): 271-282.

Frederix, F., J.-M. Friedt, K.-H. Choi, W. Laureyn, A. Campitelli, D. Mondelaers, G. Maes and G. Borghs (2003). "Biosensing Based on Light Absorption of Nanoscaled Gold and Silver Particles." Analytical Chemistry **75**(24): 6894-6900.

Gans, R. (1912). "Über die Form ultramikroskopischer Goldteilchen." Annalen der Physik **342**(5): 881-900.

Gather, M. C. (2012). "A rocky road to plasmonic lasers." Nat Photon **6**(11): 708-708.

Gittins, D. I. and F. Caruso (2001). "Tailoring the Polyelectrolyte Coating of Metal Nanoparticles." The Journal of Physical Chemistry B **105**(29): 6846-6852.

Goetzberger, A., C. Hebling and H.-W. Schock (2003). "Photovoltaic materials, history, status and outlook." Materials Science and Engineering: R: Reports **40**(1): 1-46.

Graf, C., D. L. J. Vossen, A. Imhof and A. van Blaaderen (2003). "A General Method To Coat Colloidal Particles with Silica." Langmuir **19**(17): 6693-6700.

Hammond, P. T. (1999). "Recent explorations in electrostatic multilayer thin film assembly." Current Opinion in Colloid & Interface Science **4**(6): 430-442.

Hauck, T. S., A. A. Ghazani and W. C. W. Chan (2008). "Assessing the Effect of Surface Chemistry on Gold Nanorod Uptake, Toxicity, and Gene Expression in Mammalian Cells." Small **4**(1): 153-159.

Heer, S., K. Kömpe, H. U. Güdel and M. Haase (2004). "Highly Efficient Multicolour Upconversion Emission in Transparent Colloids of Lanthanide-Doped NaYF4 Nanocrystals." Advanced Materials **16**(23-24): 2102-2105.

Heine, C. and R. H. Morf (1995). "Submicrometer gratings for solar energy applications." Appl. Opt. **34**(14): 2476-2482.

Hirai, T., T. Orikoshi and I. Komasawa (2002). "Preparation of Y_2O_3:Yb,Er Infrared-to-Visible Conversion Phosphor Fine Particles Using an Emulsion Liquid Membrane System." Chemistry of Materials **14**(8): 3576-3583.

Hiramoto, M., H. Fujiwara and M. Yokoyama (1991). "Three-layered organic solar cell with a photoactive interlayer of codeposited pigments." Applied Physics Letters **58**(10): 1062-1064.

Hiramoto, M., H. Fujiwara and M. Yokoyama (1992). "p-i-n like behavior in three-layered organic solar cells having a co-deposited interlayer of pigments." Journal of Applied Physics **72**(8): 3781-3787.

Hu, X. and X. Gao (2011). "Multilayer coating of gold nanorods for combined stability and biocompatibility." Physical Chemistry Chemical Physics **13**(21): 10028-10035.

Huang, H.-C., S. Barua, G. Sharma, S. K. Dey and K. Rege (2011). "Inorganic nanoparticles for cancer imaging and therapy." Journal of Controlled Release **155**(3): 344-357.

Huang, X., I. H. El-Sayed, W. Qian and M. A. El-Sayed (2006). "Cancer Cell Imaging and Photothermal Therapy in the Near-Infrared Region by Using Gold Nanorods." Journal of the American Chemical Society **128**(6): 2115-2120.

Huang, X., I. H. El-Sayed, W. Qian and M. A. El-Sayed (2007). "Cancer Cells Assemble and Align Gold Nanorods Conjugated to Antibodies to Produce Highly Enhanced, Sharp, and Polarized Surface Raman Spectra: A Potential Cancer Diagnostic Marker." Nano Letters **7**(6): 1591-1597.

Huang, X., P. K. Jain, I. H. El-Sayed and M. A. El-Sayed (2007). "Gold nanoparticles: interesting optical properties and recent applications in cancer diagnostic and therapy." Nanomedicine **2**(5): 681-693.

Huang, X., W. Qian, I. H. El-Sayed and M. A. El-Sayed (2007). "The potential use of the enhanced nonlinear properties of gold nanospheres in photothermal cancer therapy." Lasers in Surgery and Medicine **39**(9): 747-753.

Huang, X. H., S. Neretina and M. A. El-Sayed (2009). "Gold Nanorods: From Synthesis and Properties to Biological and Biomedical Applications." Advanced Materials **21**(48): 4880-4910.

Huff, T. B., M. N. Hansen, Y. Zhao, J. X. Cheng and A. Wei (2007). "Controlling the cellular uptake of gold nanorods." Langmuir **23**(4): 1596-1599.

Jain, P. K., X. Huang, I. H. El-Sayed and M. A. El-Sayed (2008). "Noble Metals on the Nanoscale: Optical and Photothermal Properties and Some Applications in Imaging, Sensing, Biology, and Medicine." Accounts of Chemical Research **41**(12): 1578-1586.

Jin, Y. and X. Gao (2009). "Plasmonic fluorescent quantum dots." Nature Nanotechnology **4**(9): 571-576.

Jing, S., S. Feng, T. Hao, H. Lin, Z. Feng, T. Jianguo, Z. Guangyin, C. Zhenxiang and C. Huanchu (2006). "Phonon-assisted mechanisms and concentration dependence of Tm 3+ blue upconversion luminescence in codoped $NaY(WO_4)_2$ crystals." Journal of Physics D: Applied Physics **39**(10): 2094.

Johnson, P. B. and R. W. Christy (1972). "Optical constants of noble." Physical Review B **6**(12): 4370-4379.

Kao, C.-S., F.-C. Chen, C.-W. Liao, M. H. Huang and C.-S. Hsu (2012). "Plasmonic-enhanced performance for polymer solar cells prepared with inverted structures." Applied Physics Letters **101**(19): 193902-4.

Kiess, H. and W. Rehwald (1995). "On the ultimate efficiency of solar cells." Solar Energy Materials and Solar Cells **38**(1–4): 45-55.

Kirihata, H. and M. Uda (1981). "Externally quenched air counter for low-energy electron emission measurements." Review of Scientific Instruments **52**(1): 68-70.

Kleppner, D. (1981). "Inhibited Spontaneous Emission." Physical Review Letters **47**(4): 233-236.

Klopfer, M. and R. K. Jain (2011). "Plasmonic quantum dots for nonlinear optical applications [Invited]." Opt. Mater. Express **1**(7): 1353-1366.

Kneipp, J., H. Kneipp, M. McLaughlin, D. Brown and K. Kneipp (2006). "In Vivo Molecular Probing of Cellular Compartments with Gold Nanoparticles and Nanoaggregates." Nano Letters **6**(10): 2225-2231.

Lakowicz, J. R. (2005). "Radiative decay engineering 5: metal-enhanced fluorescence and plasmon emission." Analytical Biochemistry **337**(2): 171-194.

Larsson, E. M., J. Alegret, M. Käll and D. S. Sutherland (2007). "Sensing Characteristics of NIR Localized Surface Plasmon Resonances in Gold Nanorings for Application as Ultrasensitive Biosensors." Nano Letters **7**(5): 1256-1263.

Lee, K.-S. and M. A. El-Sayed (2005). "Dependence of the Enhanced Optical Scattering Efficiency Relative to That of Absorption for Gold Metal Nanorods on Aspect Ratio, Size, End-Cap Shape, and Medium Refractive Index." The Journal of Physical Chemistry B **109**(43): 20331-20338.

Lee, S.-M., H. Park and K.-H. Yoo (2010). "Synergistic Cancer Therapeutic Effects of Locally Delivered Drug and Heat Using Multifunctional Nanoparticles." Advanced Materials **22**(36): 4049-4053.

Li, G., R. Zhu and Y. Yang (2012). "Polymer solar cells." Nat Photon **6**(3): 153-161.

Li, W. W., Y. Zhou, B. V. Andersson, L. M. Andersson, Y. Thomann, C. Veit, K. Tvingstedt, R. P. Qin, Z. S. Bo, O. Inganas, U. Wurfel and F. L. Zhang (2011). "The Effect of additive on performance and shelf-stability of HSX-1/PCBM photovoltaic devices." Organic Electronics **12**(9): 1544-1551.

Li, X., F.-J. Kao, C.-C. Chuang and S. He (2010). "Enhancing fluorescence of quantum dots by silica-coated gold nanorods under one- and two-photon excitation." Opt. Express **18**(11): 11335-11346.

Link, S., C. Burda, M. B. Mohamed, B. Nikoobakht and M. A. El-Sayed (1999). "Laser Photothermal Melting and Fragmentation of Gold Nanorods: Energy and Laser Pulse-Width Dependence." The Journal of Physical Chemistry A **103**(9): 1165-1170.

Link, S. and M. A. El-Sayed (1999). "Size and Temperature Dependence of the Plasmon Absorption of Colloidal Gold Nanoparticles." The Journal of Physical Chemistry B **103**(21): 4212-4217.

Liu, N., B. S. Prall and V. I. Klimov (2006). "Hybrid gold/silica/nanocrystal-quantum-dot superstructures: Synthesis and analysis of semiconductor-metal interactions." Journal of the American Chemical Society **128**(48): 15362-15363.

Liu, N., W. Qin, G. Qin, T. Jiang and D. Zhao (2011). "Highly plasmon-enhanced upconversion emissions from Au@β-$NaYF_4$:Yb,Tm hybrid nanostructures." Chemical Communications **47**(27): 7671-7673.

Liz-Marzán, L. M., M. Giersig and P. Mulvaney (1996). "Synthesis of Nanosized Gold−Silica Core−Shell Particles." Langmuir **12**(18): 4329-4335.

Lodahl, P., A. F. van Driel, I. S. Nikolaev, A. Irman, K. Overgaag, D. Vanmaekelbergh and W. L. Vos (2004). "Controlling the dynamics of spontaneous emission from quantum dots by photonic crystals." Nature **430**(7000): 654-657.

Loutfy, R. O. and J. H. Sharp (1979). "Photovoltaic properties of metal-free phthalocyanines. I. Al/H_2Pc Schottky barrier solar cells." The Journal of Chemical Physics **71**(3): 1211-1217.

Ma, W., C. Yang, X. Gong, K. Lee and A. J. Heeger (2005). "Thermally Stable, Efficient Polymer Solar Cells with Nanoscale Control of the Interpenetrating Network Morphology." Advanced Functional Materials **15**(10): 1617-1622.

Marks, R. N., J. J. M. Halls, D. D. C. Bradley, R. H. Friend and A. B. Holmes (1994). "The photovoltaic response in poly(p-phenylene vinylene) thin-film devices." Journal of Physics: Condensed Matter **6**(7): 1379-1383.

Martin, C. R. (1991). "Template synthesis of polymeric and metal microtubules." Advanced Materials **3**(9): 457-459.

Masuda, H., H. Tanaka and N. Baba (1990). "Preparation of Porous Material by Replacing Microstructure of Anodic Alumina Film with Metal." Chemistry Letters **19**(4): 621-622.

Matsuura, D., H. Hattori and A. Takano (2005). "Upconversion luminescence properties of Y_2O_3 nanocrystals doped with trivalent rare-earth ions." Journal of the Electrochemical Society **152**(3): H39-H42.

Mei, X., L. Lu, B. J. Tremolet de Villers, S. Huajun, Z. Jinfeng, Y. Zhibin, A. Z. Stieg, P. Qibing, B. J. Schwartz and K. L. Wang (2011). "Charge-carrier dynamics in hybrid plasmonic organic solar cells with Ag nanoparticles." Applied Physics Letters **98**(25): 253302-253306.

Melkumov, M. A., A. Y. Laptev, M. V. Yashkov, N. N. Vechkanov, A. N. Guryanov and I. A. Bufetov (2010). "Effects of Yb^{3+} and Er^{3+} concentrations and doping procedure on excitation transfer efficiency in Er-Yb doped phosphosilicate fibers." Inorganic Materials **46**(3): 299-303.

Mertens, H. and A. Polman (2006). "Plasmon-enhanced erbium luminescence." Applied Physics Letters **89**(21).

Mohamed, M. B., V. Volkov, S. Link and M. A. El-Sayed (2000). "The 'lightning' gold nanorods: fluorescence enhancement of over a million compared to the gold metal." Chemical Physics Letters **317**(6): 517-523.

Mohamed, M. B., V. Volkov, S. Link and M. A. El-Sayed (2000). "The `lightning' gold nanorods: fluorescence enhancement of over a million compared to the gold metal." Chemical Physics Letters **317**(6): 517-523.

Moon, S.-J., E. Baranoff, S. M. Zakeeruddin, C.-Y. Yeh, E. W.-G. Diau, M. Gratzel and K. Sivula (2011). "Enhanced light harvesting in mesoporous TiO_2/P_3HT hybrid solar cells using a porphyrin dye." Chemical Communications **47**(29): 8244-8246.

Mooradia.A (1969). "Photoluminescence of metals." Review Letters **22**(5): 185.

Morel, D. L., A. K. Ghosh, T. Feng, E. L. Stogryn, P. E. Purwin, R. F. Shaw and C. Fishman (1978). "High-efficiency organic solar cells." Applied Physics Letters **32**(8): 495-497.

Morfa, A. J., K. L. Rowlen, T. H. Reilly, Iii, M. J. Romero and J. van de Lagemaat (2008). "Plasmon-enhanced solar energy conversion in organic bulk heterojunction photovoltaics." Applied Physics Letters **92**(1): 013504-3.

Moskovits, M. (1985). "Surface enhanced spectroscopy." Reviews of Modern Physics **57**(3): 783-826.

Moskovits, M. (2005). "Surface-enhanced Raman spectroscopy: a brief retrospective." Journal of Raman Spectroscopy **36**(6-7): 485-496.

Murphy, C. J., T. K. Sau, A. M. Gole, C. J. Orendorff, J. Gao, L. Gou, S. E. Hunyadi and T. Li (2005). "Anisotropic Metal Nanoparticles: Synthesis, Assembly, and Optical Applications." The Journal of Physical Chemistry B **109**(29): 13857-13870.

Nabika, H. and S. Deki (2003). "Enhancing and quenching functions of silver nanoparticles on the luminescent properties of europium complex in the solution phase." Journal of Physical Chemistry B **107**(35): 9161-9164.

Nakamura, T., A. Tamura, H. Murotani, M. Oishi, Y. Jinji, K. Matsuishi and Y. Nagasaki (2010). "Large payloads of gold nanoparticles into the polyamine network core of stimuli-responsive PEGylated nanogels for selective and noninvasive cancer photothermal therapy." Nanoscale **2**(5): 739-746.

Nath, N. and A. Chilkoti (2001). "A Colorimetric Gold Nanoparticle Sensor To Interrogate Biomolecular Interactions in Real Time on a Surface." Analytical Chemistry **74**(3): 504-509.

Niidome, T., M. Yamagata, Y. Okamoto, Y. Akiyama, H. Takahashi, T. Kawano, Y. Katayama and Y. Niidome (2006). "PEG-modified gold nanorods with a stealth character for in vivo applications." Journal of Controlled Release **114**(3): 343-347.

Nikoobakht, B. and M. A. El-Sayed (2003). "Preparation and Growth Mechanism of Gold Nanorods (NRs) Using Seed-Mediated Growth Method." Chemistry of Materials **15**(10): 1957-1962.

Noginov, M. A., G. Zhu, A. M. Belgrave, R. Bakker, V. M. Shalaev, E. E. Narimanov, S. Stout, E. Herz, T. Suteewong and U. Wiesner (2009). "Demonstration of a spaser-based nanolaser." Nature **460**(7259): 1110-U68.

Noginova, N., Y. Barnakov, H. Li and M. A. Noginov (2009). "Effect of metallic surface on electric dipole and magnetic dipole emission transitions in Eu3+ doped polymeric film." Opt. Express **17**(13): 10767-10772.

Obare, S. O., N. R. Jana and C. J. Murphy (2001). "Preparation of polystyrene- and silica-coated gold nanorods and their use as templates for the synthesis of hollow nanotubes." Nano Letters **1**(11): 601-603.

Padinger, F., R. S. Rittberger and N. S. Sariciftci (2003). "Effects of Postproduction Treatment on Plastic Solar Cells." Advanced Functional Materials **13**(1): 85-88.

Park, S. H., A. Roy, S. Beaupre, S. Cho, N. Coates, J. S. Moon, D. Moses, M. Leclerc, K. Lee and A. J. Heeger (2009). "Bulk heterojunction solar cells with internal quantum efficiency approaching 100%." **3**(5): 297-302.

Pastoriza-Santos, I., R. A. Alvarez-Puebla and L. M. Liz-Marzan (2010). "Synthetic Routes and Plasmonic Properties of Noble Metal Nanoplates." European Journal Of Inorganic Chemistry(27): 4288-4297.

Pastoriza-Santos, I., D. Gomez, J. Perez-Juste, L. M. Liz-Marzan and P. Mulvaney (2004). "Optical properties of metal nanoparticle coated silica spheres: a simple effective medium approach." Physical Chemistry Chemical Physics **6**(21): 5056-5060.

Pastoriza-Santos, I., J. Perez-Juste and L. M. Liz-Marzan (2006). "Silica-coating and hydrophobation of CTAB-stabilized gold nanorods." Chemistry of Materials **18**(10): 2465-2467.

Pastoriza-Santos, I., J. Pérez-Juste and L. M. Liz-Marzán (2006). "Silica-Coating and Hydrophobation of CTAB-Stabilized Gold Nanorods." Chemistry of Materials **18**(10): 2465-2467.

Paudel, H. P., L. Zhong, K. Bayat, M. F. Baroughi, S. Smith, C. Lin, C. Jiang, M. T. Berry and P. S. May (2011). "Enhancement of Near-Infrared-to-Visible Upconversion Luminescence Using Engineered Plasmonic Gold Surfaces." The Journal of Physical Chemistry C **115**(39): 19028-19036.

Pérez-Juste, J., M. A. Correa-Duarte and L. M. Liz-Marzán (2004). "Silica gels with tailored, gold nanorod-driven optical functionalities." Applied Surface Science **226**(1–3): 137-143.

Perez-Juste, J., L. M. Liz-Marzan, S. Carnie, D. Y. C. Chan and P. Mulvaney (2004). Adv. Funct. Mater. **14**(null): 571.

Peumans, P., V. Bulovic and S. R. Forrest (2000). "Efficient photon harvesting at high optical intensities in ultrathin organic double-heterostructure photovoltaic diodes." Applied Physics Letters **76**(19): 2650-2652.

Pitsillides, C. M., E. K. Joe, X. Wei, R. R. Anderson and C. P. Lin (2003). "Selective Cell Targeting with Light-Absorbing Microparticles and Nanoparticles." Biophysical Journal **84**(6): 4023-4032.

Poh, C.-H., L. Rosa, S. Juodkazis and P. Dastoor (2011). "FDTD modeling to enhance the performance of an organic solar cell embedded with gold nanoparticles." Opt. Mater. Express **1**(7): 1326-1331.

Priyam, A., N. M. Idris and Y. Zhang (2012). "Gold nanoshell coated $NaYF_4$ nanoparticles for simultaneously enhanced upconversion fluorescence and darkfield imaging." Journal of Materials Chemistry **22**(3): 960-965.

Purcell, E. M. (1946). "Spontaneous Emission Probabilities At Radio Frequencies." Physical Review **69**(11-1): 681-681.

Pustovit, V. N. and T. V. Shahbazyan (2012). "Fluorescence quenching near small metal nanoparticles." The Journal of Chemical Physics **136**(20): 204701-6.

Qiao, L., D. Wang, L. Zuo, Y. Ye, J. Qian, H. Chen and S. He (2011). "Localized surface plasmon resonance enhanced organic solar cell with gold nanospheres." Applied Energy **88**(3): 848-852.

Qiaoqiang, G., F. J. Bartoli and Z. H. Kafafi (2012). "Research Highlights on Organic Photovoltaics and Plasmonics." Photonics Journal, IEEE **4**(2): 620-624.

Rai, V. K., L. d. S. Menezes, C. B. de Araujo, L. R. P. Kassab, D. M. da Silva and R. A. Kobayashi (2008). "Surface-plasmon-enhanced frequency upconversion in Pr^{3+} doped tellurium-oxide glasses containing silver nanoparticles." Journal of Applied Physics **103**(9).

Ren, B. X., F. Yang, G. H. Zhu, Z. X. Huang, H. Ai, R. Xia, X. J. Liu, M. Lu and B. Song (2012). "Magnetic resonance tumor targeting imaging using gadolinium labeled human telomerase reverse transcriptase antisense probes." Cancer Science **103**(8): 1434-1439.

Rodríguez-Fernández, J., I. Pastoriza-Santos, J. Pérez-Juste, F. J. García de Abajo and L. M. Liz-Marzán (2007). "The Effect of Silica Coating on the Optical Response of Sub-micrometer Gold Spheres." The Journal of Physical Chemistry C **111**(36): 13361-13366.

Rodriguez-Gonzalez, B., P. Mulvaney and L. M. Liz-Marzan (2007). "An electrochemical model for gold colloid formation via citrate reduction." Zeitschrift Fur Physikalische Chemie-International Journal Of Research In Physical Chemistry & Chemical Physics **221**(3): 415-426.

Rodriguez-Lorenzo, L., P. Aldeanueva-Potel, R. A. Alvarez-Puebla, L. M. Liz-Marzan and F. J. G. de Abajo (2010). "SERS-Based Ultrasensitive Detection with Tips-shaped Anisotropic Particles." Xxii International Conference On Raman Spectroscopy **1267**: 927-927.

Rodríguez-Lorenzo, L., R. n. A. Álvarez-Puebla, I. Pastoriza-Santos, S. Mazzucco, O. Stéphan, M. Kociak, L. M. Liz-Marzán and F. J. García de Abajo (2009). "Zeptomol Detection Through Controlled Ultrasensitive Surface-Enhanced Raman Scattering." Journal of the American Chemical Society **131**(13): 4616-4618.

Rogobete, L., F. Kaminski, M. Agio and V. Sandoghdar (2007). "Design of plasmonic nanoantennae for enhancing spontaneous emission." Opt. Lett. **32**(12): 1623-1625.

Saboktakin, M., X. Ye, S. J. Oh, S.-H. Hong, A. T. Fafarman, U. K. Chettiar, N. Engheta, C. B. Murray and C. R. Kagan (2012). "Metal-Enhanced Upconversion Luminescence Tunable through Metal Nanoparticle–Nanophosphor Separation." ACS Nano **6**(10): 8758-8766.

Saha, A., S. K. Basiruddin, R. Sarkar, N. Pradhan and N. R. Jana (2009). "Functionalized Plasmonic-Fluorescent Nanoparticles for Imaging and Detection." Journal of Physical Chemistry C **113**(43): 18492-18498.

Sanchez, E. J., L. Novotny and X. S. Xie (1999). "Near-field fluorescence microscopy based on two-photon excitation with metal tips." Physical Review Letters **82**(20): 4014-4017.

Sannomiya, T., C. Hafner and J. Voros (2008). "In situ Sensing of Single Binding Events by Localized Surface Plasmon Resonance." Nano Letters **8**(10): 3450-3455.

Sariciftci, N. S., D. Braun, C. Zhang, V. I. Srdanov, A. J. Heeger, G. Stucky and F. Wudl (1993). "Semiconducting polymer-buckminsterfullerene heterojunctions: Diodes, photodiodes, and photovoltaic cells." Applied Physics Letters **62**(6): 585-587.

Sariciftci, N. S., L. Smilowitz, A. J. Heeger and F. Wudl (1992). "Photoinduced electron transfer from a conducting polymer to Buckminsterfullerene." Science **258**(5087): 1474-1476.

Sau, T. K. and C. J. Murphy (2005). "Self-assembly patterns formed upon solvent evaporation of aqueous cetyltrimethylammonium bromide-coated gold nanoparticles of various shapes." Langmuir **21**(7): 2923-2929.

Schietinger, S., T. Aichele, H.-Q. Wang, T. Nann and O. Benson (2009). "Plasmon-Enhanced Upconversion in Single $NaYF_4$:Yb^{3+}/Er^{3+} Codoped Nanocrystals." Nano Letters **10**(1): 134-138.

Schmid, G., R. Pfeil, R. Boese, F. Bandermann, S. Meyer, G. H. M. Calis and J. W. A. van der Velden (1981). "$Au_{55}[P(C_6H_5)_3]_{12}CI_6$ — ein Goldcluster ungewöhnlicher Größe." Chemische Berichte **114**(11): 3634-3642.

Schneider, G., G. Decher, N. Nerambourg, R. Praho, M. H. V. Werts and M. Blanchard-Desce (2006). "Distance-dependent fluorescence quenching on gold nanoparticles ensheathed with layer-by-layer assembled polyelectrolytes." Nano Letters **6**(3): 530-536.

Sepúlveda, B., P. C. Angelomé, L. M. Lechuga and L. M. Liz-Marzán (2009). "LSPR-based nanobiosensors." Nano Today **4**(3): 244-251.

Service, R. F. (2011). "Outlook Brightens for Plastic Solar Cells." Science **332**(6027): 293.

Sharma, P., S. Brown, G. Walter, S. Santra and B. Moudgil (2006). "Nanoparticles for bioimaging." Advances in Colloid and Interface Science **123–126**(0): 471-485.

Song, J. H., T. Atay, S. F. Shi, H. Urabe and A. V. Nurmikko (2005). "Large enhancement of fluorescence efficiency from CdSe/ZnS quantum dots induced by resonant coupling to spatially controlled surface plasmons." Nano Letters **5**(8): 1557-1561.

Sortino, S. (2012). "Photoactivated nanomaterials for biomedical release applications." Journal of Materials Chemistry **22**(2): 301-318.

Sotiriou, G. A. (2013). "Biomedical applications of multifunctional plasmonic nanoparticles." Wiley Interdisciplinary Reviews: Nanomedicine and Nanobiotechnology **5**(1): 19-30.

Sotiriou, G. A., A. M. Hirt, P.-Y. Lozach, A. Teleki, F. Krumeich and S. E. Pratsinis (2011). "Hybrid, Silica-Coated, Janus-Like Plasmonic-Magnetic Nanoparticles." Chemistry of Materials **23**(7): 1985-1992.

Stöber, W., A. Fink and E. Bohn (1968). "Controlled growth of monodisperse silica spheres in the micron size range." Journal of Colloid and Interface Science **26**(1): 62-69.

Sze, S. M. (1969). "Semiconductor devices, Physics of." Second Edition, John Wiley, New York.

Szeremeta, J., M. Nyk, A. Chyla, W. Strek and M. Samoc (2011). "Enhancement of photoconduction in a conjugated polymer through doping with copper nanoparticles." Optical Materials **33**(9): 1372-1376.

Tang, C. W. (1986). "2-Layer Organic Photovoltaic Cell." Applied Physics Letters **48**(2): 183-185.

Tikhomirov, V. K., V. D. Rodríguez, J. Méndez-Ramos, J. del-Castillo, D. Kirilenko, G. Van Tendeloo and V. V. Moshchalkov (2012). "Optimizing Er/Yb ratio and content in Er–Yb co-doped glass-ceramics for enhancement of the up- and down-conversion luminescence." Solar Energy Materials and Solar Cells **100**(0): 209-215.

Timothy, A. L., B. James, A. Jesse and S. Konstantin (2007). "Hybrid plasmonic magnetic nanoparticles as molecular specific agents for MRI/optical imaging and photothermal therapy of cancer cells." Nanotechnology **18**(32): 325101.

Tong, L., Q. Wei, A. Wei and J.-X. Cheng (2009). "Gold Nanorods as Contrast Agents for Biological Imaging: Optical Properties, Surface Conjugation and Photothermal Effects." Photochemistry and Photobiology **85**(1): 21-32.

Tong, R. and D. S. Kohane (2012). "Shedding light on nanomedicine." Wiley Interdisciplinary Reviews: Nanomedicine and Nanobiotechnology **4**(6): 638-662.

Turkevich, J., P. C. Stevenson and J. Hillier (1951). "A study of the nucleation and growth processes in the synthesis of colloidal gold." Discussions of the Faraday Society **11**(0): 55-75.

van den Broek, B., B. Ashcroft, T. H. Oosterkamp and J. van Noort (2013). "Parallel Nanometric 3D Tracking of Intracellular Gold Nanorods Using Multifocal Two-Photon Microscopy." Nano Letters **13**(3): 980-986.

Vigderman, L. and E. R. Zubarev (2012). "Starfruit-Shaped Gold Nanorods and Nanowires: Synthesis and SERS Characterization." Langmuir **28**(24): 9034-9040.

von Maltzahn, G., J.-H. Park, A. Agrawal, N. K. Bandaru, S. K. Das, M. J. Sailor and S. N. Bhatia (2009). "Computationally Guided Photothermal Tumor Therapy Using Long-Circulating Gold Nanorod Antennas." Cancer Research **69**(9): 3892-3900.

Wagner, H. J. and R. O. Loutfy (1982). "Photoelectric properties of CdS--MgPc heterojunction solar cells." Journal of Vacuum Science and Technology **20**(3): 300-304.

Wang, C., H. Xu, C. Liang, Y. Liu, Z. Li, G. Yang, L. Cheng, Y. Li, Z. Liu (2013). “Iron Oxide @ Polypyrrole Nanoparticles as a Multifunctional Drug Carrier for Remotely Controlled Cancer Therapy with Synergistic Antitumor Effects.” ACS Nano **7**(8): 6782-6795.

Wang, D. H., D. Y. Kim, K. W. Choi, J. H. Seo, S. H. Im, J. H. Park, O. O. Park and A. J. Heeger (2011). "Enhancement of Donor–Acceptor Polymer Bulk Heterojunction Solar Cell Power Conversion Efficiencies by Addition of Au Nanoparticles." Angewandte Chemie International Edition **50**(24): 5519-5523.

Wang, H., T. B. Huff, D. A. Zweifel, W. He, P. S. Low, A. Wei and J.-X. Cheng (2005). "In vitro and in vivo two-photon luminescence imaging of single gold nanorods." Proceedings of the National Academy of Sciences of the United States of America **102**(44): 15752-15756.

Wang, M., G. Abbineni, A. Clevenger, C. Mao and S. Xu (2011). "Upconversion nanoparticles: synthesis, surface modification and biological applications." Nanomedicine: Nanotechnology, Biology and Medicine **7**(6): 710-729.

Wang, Z. L., M. B. Mohamed, S. Link and M. A. El-Sayed (1999). "Crystallographic facets and shapes of gold nanorods of different aspect ratios." Surface Science **440**(1–2): L809-L814.

Watekar, P. R., S. Ju and W.-T. Han (2008). "Optical properties of the alumino-silicate glass doped with Er-ions/Au particles." Colloids and Surfaces A: Physicochemical and Engineering Aspects **313–314**(0): 492-496.

Weare, W. W., S. M. Reed, M. G. Warner and J. E. Hutchison (2000). "Improved Synthesis of Small (dCORE ≈ 1.5 nm) Phosphine-Stabilized Gold Nanoparticles." Journal of the American Chemical Society **122**(51): 12890-12891.

Weiss, S. (1999). "Fluorescence Spectroscopy of Single Biomolecules." Science **283**(5408): 1676-1683.

Wu, J.-L., F.-C. Chen, Y.-S. Hsiao, F.-C. Chien, P. Chen, C.-H. Kuo, M. H. Huang and C.-S. Hsu (2011). "Surface Plasmonic Effects of Metallic Nanoparticles on the Performance of Polymer Bulk Heterojunction Solar Cells." ACS Nano **5**(2): 959-967.

Wu, S., G. Han, D. J. Milliron, S. Aloni, V. Altoe, D. V. Talapin, B. E. Cohen and P. J. Schuck (2009). "Non-blinking and photostable upconverted luminescence from single lanthanide-doped nanocrystals." Proceedings of the National Academy of Sciences **106**(27): 10917-10921.

Wu, W., J. Shen, P. Banerjee and S. Zhou (2011). "A Multifuntional Nanoplatform Based on Responsive Fluorescent Plasmonic ZnO-Au@PEG Hybrid Nanogels." Advanced Functional Materials **21**(15): 2830-2839.

Xu, H., E. J. Bjerneld, M. Käll and L. Börjesson (1999). "Spectroscopy of Single Hemoglobin Molecules by Surface Enhanced Raman Scattering." Physical Review Letters **83**(21): 4357-4360.

Yablonovitch, E. and G. D. Cody (1982). "Intensity enhancement in textured optical sheets for solar cells." Electron Devices, IEEE Transactions on **29**(2): 300-305.

Yang, J., J. B. You, C. C. Chen, W. C. Hsu, H. R. Tan, X. W. Zhang, Z. R. Hong and Y. Yang (2011). "Plasmonic Polymer Tandem Solar Cell." ACS Nano **5**(8): 6210-6217.

Yang, X., Liu, J., He, H., Zhou, L.,Gong, C., Wang, X.,Yang, L., Yuan, J., Huang, H., He, L., Zhang, B. and Z. Zhuang (2010). "SiO_2 nanoparticles induce cytotoxicity and protein expression alteration in HaCaT cells", Particle and Fibre Toxicology **7**(1): 1-12

Yokoyama, M., Y. Endo, A. Matsubara and F. H. Mikawa (1981). "Mechanism of extrinsic carrier photogeneration in poly-N-vinylcarbazole. II. Quenching of exciplex fluorescence by electric field." The Journal of Chemical Physics **75**(6): 3006-3011.

Yokoyama, M., S. Shimokihara, A. Matsubara and H. Mikawa (1982). "Extrinsic carrier photogeneration in poly-N-vinylcarbazole. III. CT fluorescence quenching by an electric field." The Journal of Chemical Physics **76**(1): 724-728.

Yonzon, C. R., E. Jeoung, S. Zou, G. C. Schatz, M. Mrksich and R. P. Van Duyne (2004). "A Comparative Analysis of Localized and Propagating Surface Plasmon Resonance Sensors: The Binding of Concanavalin A to a Monosaccharide Functionalized Self-Assembled Monolayer." Journal of the American Chemical Society **126**(39): 12669-12676.

Yorulmaz, M., S. Khatua, P. Zijlstra, A. Gaiduk and M. Orrit (2012). "Luminescence Quantum Yield of Single Gold Nanorods." Nano Letters **12**(9): 5059-5059.

Yu, S.-S. Chang, C.-L. Lee and C. R. C. Wang (1997). "Gold Nanorods: Electrochemical Synthesis and Optical Properties." The Journal of Physical Chemistry B **101**(34): 661-664.

Yu, G., J. Gao, J. C. Hummelen, F. Wudl and A. J. Heeger (1995). "Polymer Photovoltaic Cells: Enhanced Efficiencies via a Network of Internal Donor-Acceptor Heterojunctions." Science **270**(5243): 1789-1791.

Zhang, F., G. B. Braun, Y. Shi, Y. Zhang, X. Sun, N. O. Reich, D. Zhao and G. Stucky (2010). "Fabrication of $Ag@SiO_2@Y_2O_3$:Er Nanostructures for Bioimaging: Tuning of the Upconversion Fluorescence with Silver Nanoparticles." Journal of the American Chemical Society **132**(9): 2850-2851.

Zhang, X. F., L. Clime, H. Q. Ly, M. Trudeau and T. Veres (2010). "Multifunctional Fe_3O_4−Au/Porous Silica@Fluorescein Core/Shell Nanoparticles with Enhanced Fluorescence Quantum Yield." The Journal of Physical Chemistry C **114**(43): 18313-18317.

Zhang, X., Hong, Y., Tang, M. and Y. Pu. (2011). "ZnO, TiO_2, SiO_2 and Al_2O_3 Nanoparticles-induced Toxic Effects on Human Fetal Lung Fibroblasts", Biomed. Environ. Sci. **24**(6):661-669.

Zhang, Z., L. Wang, J. Wang, X. Jiang, X. Li, Z. Hu, Y. Ji, X. Wu and C. Chen (2012). "Mesoporous Silica-Coated Gold Nanorods as a Light-Mediated Multifunctional Theranostic Platform for Cancer Treatment." Advanced Materials **24**(11): 1418-1423.

Zhou, J.-C., Z.-L. Yang, W. Dong, R.-J. Tang, L.-D. Sun and C.-H. Yan (2011). "Bioimaging and toxicity assessments of near-infrared upconversion luminescent $NaYF_4$:Yb,Tm nanocrystals." Biomaterials **32**(34): 9059-9067.